Design of Efficient Cobalt-based Bi-functional Catalysts for Zinc-Air Batteries

by

Guihua Liu

A thesis

presented to the University of Waterloo

in fulfillment of the

thesis requirement for the degree of

Doctor of Philosophy

in

Chemical Engineering

Waterloo, Ontario, Canada, 2019

Examining Committee Membership

The following served on the Examining Committee for this thesis. The decision of the Examining Committee is by majority vote.

External Examiner	Dr. Aicheng Chen Professor
Supervisor	Dr. Zhongwei Chen Professor
Internal Member	Dr. Eric Croiset Professor
Internal Member	Dr. Jeffery Gostick Professor
Internal-external Member	Dr. Juewen Liu Professor

Author's Declaration

This thesis consists of material all of which I authored or co-authored: see Statement of Contributions included in the thesis. This is a true copy of the thesis, including any required final revisions, as accepted by my examiners.

I understand that my thesis may be made electronically available to the public.

Statement of Contributions

Some of the chapters in this thesis are based published works co-authored by myself. These include the following publications.

Chapter 2 of this thesis consist of some paragraphs from a review paper that I was co-authored with my supervisor, and Dr. Jing Fu, Ruilin Liang, Dr. Aiping Yu, Dr. Zhenyu Bai. I am the third author of this paper and assisted with the writing of the paper.

"Recent progress in electrically rechargeable zinc-air batteries", Advanced Materials, 2018, 1805230

Chapter 4 of this thesis consist of paragraphs from a paper that was co-authored by myself, my supervisor, Dr. Jingde Li, Dr, Jing Fu, Dr. Gaopeng Jiang, Dan Luo, Dr. Fathy M. Hassan, Jing Zhang, Ya-Ping Deng, Pan Xu, and Dr. Luis Ricardez-Sandoval. I contributed equally to the paper as co-first author. In this work, I performed most of the experiments, data analysis and involved in the writing of the manuscript.

"Surface decorated cobalt sulfide as efficient catalyst for oxygen evolution reaction and its intrinsic activity", Journal of Catalysis, 2018, 367: 43–52

Chapter 6 of this thesis consists of a paper that was co-authored by myself, my supervisor, Dr. Jingde Li, Dr. Jing Fu, Dr. Gaopeng Jiang, Dr. Gregory Lui, Dan Luo, Ya-Ping Deng, Jing Zhang, Zachary P. Cano, Dr. Aiping Yu, Dr. Dong Su, Dr. Zhengyu Bai, Dr. Lin Yang. I am the first author of this paper, and I carried out most of the experiments, collected and analyzed the data, as well as the writing of the manuscript.

"Oxygen vacancy-rich semiconductor supported bifunctional catalyst for efficient and stable zinc-air battery", Advanced Materials, 2019, 31, 1806761.

Abstract

Due to its high theoretical specific energy and low-cost, rechargeable zinc-air batteries have attracted tremendous attention as a promising next-generation energy conversion system. However, there are some challenges that need to overcome before its practical application. One of the key issues is the slow reaction kinetics in the air cathode of the batteries towards the oxygen reduction reaction (ORR) and oxygen evolution reaction (OER). This would cause insufficient charge/discharge efficiency and poor cycle stability of the batteries. Therefore, the development of efficient ORR-OER bi-functional electrocatalysts with high catalytic activity and durability is essential for the development of rechargeable zinc-air batteries.

In this work, a series of catalyst design strategies have been explored to improve the activity and durability of cobalt-based bi-functional catalysts especially under the oxidative condition of OER reaction. The latter would cause catalyst oxidation and aggregation, and therefore deteriorate the cycling performance of the bi-functional catalysts in zinc-air batteries. In the first study, a surface engineering approach was adopted to prepare efficient bi-functional catalyst consists of mildly oxidized, N-doped Co_9S_8 catalyst supported on N-doped reduce graphite oxide (O-N-Co_9S_8@N-RGO). The surface decorated electrocatalyst shows excellent activity for both ORR and OER, and maintains good stability over 900 charge-discharge cycles at 10 mA cm^{-2} in zinc-air battery. Interestedly, it was found that O-N-Co_9S_8 nanoparticles responsible for the OER reaction were completely converted into Co_3O_4 after OER reaction, indicating Co_3O_4 is the actual active phase for OER. On the basis of this observation, we propose and demonstrate that oxides in-situ generated cobalt oxides during OER reaction are more active than the directly calcined oxides. This work advances fundamental insight and the design of metal chalcogenides-based bi-functional “catalysts”.

On the recognition of the high catalytic activity of surface-engineered Co_9S_8 material, a three-dimensionally ordered mesoporous (3DOM) structured surface-engineered Co_9S_8 catalyst was developed to explore the benefits of the 3DOM structural design for its catalytic performance. Different from the N-RGO supported O-N-Co_9S_8, the 3DOM-Co_9S_8 catalyst is self-supported, which contains only an inner carbon layer within its mesoporous structure. Due to the 3D interconnected architecture and large surface area, the air electrode delivers excellent cell performance and cycling durability. However, the partial structure crush of N-Co_9S_8 after long-time OER testing was observed, demonstrating that the highly oxidative operating condition of rechargeable zinc-air batteries could cause significant structural integrity issues of porous chalcogenide electrocatalysts.

Thus, in the last study, a new strategy focusing on the oxidation-resistive catalyst support design using oxygen vacancy (OV)-rich, low-bandgap semiconductor was proposed. The OVs promote the electrical conductivity of the semiconductor support, and at the same time offer a strong metal-support interaction (SMSI). The SMSI enables the catalysts with small metal size, high catalytic activity, and high stability. This strategy is demonstrated by successfully synthesizing ultrafine Co metal decorated 3DOM titanium oxynitride (3DOM-Co@TiO_xN_y). The catalyst not only exhibits good ORR-OER activities, but also shows excellent cycling stability in alkaline conditions, e.g. less than 1% energy efficiency loss over 900 charge-discharge cycles at 20 mA cm^{-2}. Theoretical calculation confirmed that the high stability of this catalyst is attributed to the strong SMSI between Co and 3DOM-TiO_xN_y. This study will provide an alternative strategy for the design of efficient and durable non-precious electrocatalysts using OV-rich semiconductors as support materials.

In summary, a series of catalyst design strategies for efficient and durable bi-functional ORR-

OER catalyst were developed in this work. It was found that NH_3 treatment is an effective surface-engineering approach to develop highly active ORR-OER catalysts. The in-situ transformation or oxidation of Co_9S_8 into Co_3O_4 observed in post-OER analysis advanced our understanding of the chemical, structural transformation and real catalytic phase for OER "catalyst". Moreover, the results show that the 3DOM design of self-supported Co_9S_8 catalyst could also benefits the catalytic performance by facilitating the mass and electronic transportation within the 3DOM framework. Finally, based on our up-to-date understanding of the OV in semiconductor physics and heterogeneous catalysis, a novel bi-functional catalyst support design strategy was proposed and demonstrated using OV-rich TiO_xN_y semiconductor. Excellent cycling stability and activity performance of such semiconductor supported cobalt catalyst in rechargeable zinc-air batteries is achieved.

Acknowledgements

I would like to express my sincere gratitude to my supervisor, Professor Zhongwei Chen, for his support, motivation, guidance and advice during my Ph.D. study. I would also like extend thanks to my Ph.D. exam committee members, including Professor Eric Croiset, Professor Jeffery Gostick Professor Junwen Liu and Professor Ali Elkamel from the University of Waterloo, and Professor Aicheng Chen as my external examiner from the University of Guelph for their valuable time and insights.

I would also like to thanks all the group members who were always there to help in my project, especially Dr. Jing Fu for her support and assistance in my Ph.D. study. Special thanks go to Dr. Hadis Zarrin for her support and assistance at the beginning of my Ph.D. study. I also received help from my outstanding colleagues which included, but not limited to, Dr. Gaopeng Jiang, Dr. Dong Un Lee, Zachary P. Cano, Jing Zhang, Ya-ping Deng, Dan Luo, Ruilin Liang and also my office member Dr. Sannan Yousaf Toor. Thanks a lot for all your help and support in the past four years.

Moreover, I would like to acknowledge my parents and my husband Dr. Jingde Li. I am grateful for their unconditional love, support and sacrifice. Also, I would like to express my spatial thanks to my three-year-old son, Daniel Li for the fun he brings to me during my Ph.D. study.

Finally, I would like to mention my gratitude to the Natural Science and Engineering Research Council of Canada (NSERC), the Waterloo Institute for Nanotechnology, and the University of Waterloo for financial support.

Table of Contents

List of Figures

List of Tables

List of Abbreviations

3DOM – Three-dimensionally ordered mesoporous

BET – Brunauer-Emmett-Teller

CV – Cyclic voltammetry

DDI – Distilled de-ionized water

EDS – Energy dispersive X-ray spectroscopy

FFT – Fast Fourier transform

GDL – Gas diffusion layer

Ir/C – Iridium on carbon catalyst

N-CNF – N-codoped carbon nano frame

N-CNT – N-doped carbon nanotube

N-RGO – Nitrogen-doped reduce graphite oxide

NR – Nano Rod

ORR – Oxygen reduction reaction

OER – Oxygen evolution reaction

OV– Oxygen Vacancy

PS – Polystyrene

Pt/C – Platinum on carbon catalyst

PVP – Polyvinylpyrrolidone

RDE – Rotating disk electrode

RHE – Reversible hydrogen electrode

SEM – Scanning electron microscopy

SMSI – Strong Metal-Support Interaction

TEM – Transmission electron microscopy

XPS – X-ray photoelectron spectroscopy

XRD – X-ray diffraction

CHAPTER 1

Introduction and Motivation

Rechargeable zinc-air batteries have attracted extensive attention because of their low-cost and high energy density (1084 Wh kg^{-1}), which is approximately five times that of lithium-ion batteries.[1] The practical application of rechargeable zinc-air batteries, however, requires active and durable air electrode electrocatalysts for both oxygen reduction reaction (ORR) and oxygen evolution reaction (OER). Pt-based materials are the most active ORR catalysts,[2] whereas Ru/Ir oxides are usually considered as the best-performing OER electrocatalysts.[3] However, these materials are expensive and exhibit poor bi-functional ORR-OER activity. Therefore, developing low-cost and efficient ORR-OER bi-functional catalysts is one of the major challenges for zinc-air batteries.[4]

Nowadays, the most promising non-precious bi-functional catalysts are derived from carbon-transition metal hybrid materials.[5-8] These materials have received considerable attention due to their unique physical and chemical properties: *i)* the carbon material, as a support, ensure the good conductivity of the catalysts; *ii)* when doped with N, S or transition metal elements, e.g. Fe, Co, it shows excellent ORR activity,[9,10] and its ORR activity is originated from the N/S-dopant neighbouring carbon atoms, the edges (or defect) sites and the C-N-M (M=Co, Fe) center within the carbon structure;[11-15] *iii)* the transition metals govern the OER activities, especially their oxides, hydroxides, chalcogenide, phosphate or nitride have been reported exhibits good OER activity.[16-19]

Despite these progress achieved in the development of active bi-functional catalysts, to further improve the power performance and energy efficiency of zinc-air batteries, the search for

high-performance bi-functional oxygen electrocatalysts is still under increasing demand. Recently, surface engineering(e.g. NH_3 etching), cation or anion substituting, heteroatom doping of transition metal chalcogenides and nitrides have been reported can effectively improve catalytic activities, especially towards OER.[20-22] Moreover, since the ORR-OER reactions occur at the O_2 gas/catalyst/electrolyte three-phase interface, catalysts with porous structure might facilitate the mass transfer process, e.g. O_2 gas diffusion within the catalyst, which could further improve the electrochemical performances of the batteries.[23-25] Therefore, surface engineering of cobalt chalcogenides combined with a porous structural design, e.g. three-dimensional ordered macroporous (3DOM) morphology, might further advances the development of efficient ORR-OER bi-functional catalysts in zinc-air batteries.

In fact, the practical application of the zinc-air batteries requires the aforementioned hybrid catalysts not only exhibit high ORR-OER activities, but also present good stability during the reactions. However, a critical issue in the development of durable ORR-OER bi-functional catalysts is that the highly oxidative operating condition of rechargeable zinc-air batteries causes oxidation of bi-functional oxygen electrocatalysts.[26] This would lead to structural and chemical changes of the transition metal materials. The in-situ transformation of the as-prepared catalyst during OER reaction has raised a question that what are the real active OER components in the "catalysts",[27] which highlight the importance of post-OER characterization of the as-prepared bi-functional catalyst to identify the real catalytic OER component. In addition, carbon electrochemical oxidation occurs during OER, which causes the loss or aggregation of carbon-supported transition metal catalysts, and therefore degrades the electrocatalysis durability and performance.[28,29]

To alleviate the carbon electrochemical oxidation in OER, some strategies were proposed

including coating the carbon materials with corrosion resistive TiO_2,[30,31] or developing stable perovskites oxides as active catalysts,[32] Indeed, metal oxides are more resistive to oxidation than carbon, but they usually have a low electrical conductivity, which hinders the electrocatalysis efficiency. Therefore, an ideal catalyst for rechargeable zinc-air battery should have corrosion resistance properties under oxidizing conditions of OER, accompanied with good conductivity and bi-functional catalytic activity.

In summary, previous studies have demonstrated that: *i)* surface engineering of transition metal chalcogenides is an effective strategy to prepare active ORR-OER bi-functional catalysts; *ii)* the study of real active phase for OER is necessary and has attracted increasing attention for researchers; *iii)* a combination of surface engineering and porous structure design would benefits the overall performance of the catalysts by providing a high surface area and the short diffusion path of the recants and products within its porous channels; and *iv)* the selection or synthesis of conductive oxidation-resistant support materials is essential for the durability performance of ORR-OER bi-functional catalysts in zinc-air batteries.

Therefore, in this study, a series of catalyst design strategies have been adopted and proposed for the development of active and durable ORR-OER bi-functional catalysts. First, using NH_3 etching surface engineering, a highly active bi-functional catalyst that consists of surface-decorated (nitrogen-doped, mildly oxidized) Co_9S_8 crystals and nitrogen-doped reduce graphite oxide sheet (O-N-Co_9S_8@N-RGO) was developed. In order to probe the real active OER phase, ex-situ characterization of the as-prepared catalyst was performed. The development of efficient surface-decorated Co_9S_8 catalyst was further extended by designing it into a 3DOM structure to evaluate its effectiveness in improving the electrocatalysis performance in zinc-air batteries. Moreover, to address the carbon-corrosion issue in zinc-air batteries, a novel catalyst support

design was proposed and successfully demonstrated by using 3DOM structured OV-rich, low-bandgap oxide semiconductor as oxidation resistive conductive support, and at the same time to obtain highly dispersed, ultra-small cobalt nanocrystals as active and stable 3DOM-Co@TiO_xN_y bi-functional catalyst for zinc-air batteries.

1.1 Research objectives

Based on the above, the goal of this research is to develop efficient ORR-OER bi-functional electrocatalysts for rechargeable zinc-air batteries. To achieve this goal, a series of catalyst design strategies that may boost the activity and durability performance of transition metal materials toward ORR-OER were explored. The specific objectives of this study are:

i) to develop efficient reduced graphene oxide supported Co_9S_8 ORR-OER bi-functional catalyst using surface engineering approach, e.g. NH_3 etching;

ii) to provide insights on the real catalytic phase of cobalt-based materials under the oxidative operating of OER by ex-situ characterization of the as-developed catalyst;

iii) to evaluate the effectiveness of 3DOM structural design on the catalytic performance of surface-engineered Co_9S_8 catalyst;

iv) to develop a highly active, oxidation-resistive and durable bi-functional catalyst using OV-rich conductive semiconductor (e.g. TiO_xN_y) as support.

1.2 Research contribution

i) An efficient surface decorated O-N-Co_9S_8 bi-functional oxygen electrocatalyst was developed. It was revealed that, for the first time, the high activity of O-N-Co_9S_8 is contributed

by the *in-situ* generated Co_3O_4 phase exposing high-index surfaces. On the basis of this observation, it was proposed and demonstrated that oxides *in-situ* generated during OER are more active than the directly calcined oxides. This work advances fundamental insight of metal chalcogenides "catalysts" and guides the design of active bi-functional catalysts in rechargeable zinc-air batteries.

ii) The first 3DOM structured self-supported N-Co_9S_8 bi-functional catalyst was prepared. The investigation on its ORR-OER activity, durability performance and its structural integrity under oxidative OER reaction reveal that 3DOM morphology design is an effective strategy to improve the overall catalytic performance of transition metal catalysts. However, the partial structure crush of 3DOM N-Co_9S_8 after long-time OER testing implies that chalcogenide compounds might not suitable for the design of structurally robust bi-functional catalyst.

iii) Building on a multidisciplinary understanding of OVs in semiconductor physics and heterogeneous solid-gas catalysis, a novel ORR-OER bi-functional catalyst design strategy was proposed to develop active and oxidation-resistive semiconductor-based 3DOM structured electrocatalyst. The OVs of semiconductor substrate (TiO_xN_y) not only endows the oxides with excellent conductivity, but also induce strong metal-support interaction (SMSI) that favours the formation and stabilization of highly active ultrafine cobalt nanoparticles governing OER-ORR activities. This work sheds light on using OV-rich semiconductors as promising support to design efficient and durable non-precious electrocatalysts.

1.3 Outline of the thesis

This thesis consists of seven chapters as follows:

Chapter 1 gives an overview of the thesis, including introduction and fundamentals of the ORR-OER bi-functional catalysts. The main objectives and contributions of the research are also presented in this chapter.

Chapter 2 reviews and summarizes the literature about ORR-OER bi-functional catalysts in zinc-air batteries.

Chapter 3 gives the introductions to the experimental characterization techniques used in this research.

Beginning with Chapter 4, different catalyst design strategies that aim to improve the activity and durability performance of the ORR-OER bi-functional catalysts are presented. For example, Chapter 4 presents a surface-engineering strategy to design efficient RGO supported O-N-Co_9S_8 catalysts.

A 3DOM structured N-doped Co_9S_8 catalyst design is introduced in Chapter 5 to evaluate the effect of catalyst structure on the overall performance of the surface-engineered Co_9S_8 based catalyst.

In Chapter 6, an alternative strategy focusing on the catalyst support design to obtain highly active and durable ORR-OER catalysts is proposed. In this strategy, for the first time, the concept of OVs-induced strong metal-support interaction (SMSI) is introduced to design active and stable semiconductor-based electrocatalysts with ultrafine dispersion of the active cobalt phase for ORR and OER.

Chapter 7 concludes the results obtained from this study and provides recommendations for further studies.

CHAPTER 2

Background and Literature Review

This chapter provides the background to zinc-air batteries and the ORR-OER bi-functional catalysts. The first section presents an overview of the topic. A brief introduction of zinc-air batteries including its components and ORR-OER reaction is given in Section 2.2. Literature reviews on the ORR-OER catalysts are provided in Section 2.3. Commonly used oxygen electrocatalysts design strategies are reviewed in Section 2.4, and the recent progress on the understanding of real OER catalytic phase are discussed in Section 2.5.

2.1 Overview

As an alternative energy and power source for fossil fuels, electrochemical energy storage and conversion technologies are gaining rapidly increasing attention. Currently, the most successful electrochemical-based renewable energy technologies are lithium-ion batteries and fuel cells.[1] However, their high costs and inherent safety issues have driven the need to develop cheaper, advanced next-generation electrochemical systems.[2,3] A promising solution is zinc-air batteries, in which the selection of readily accessible zinc and atmospheric oxygen can greatly reduce its cost.[4] Additionally, it has a high theoretical specific energy (1218 Wh kg^{-1}) and volumetric energy density of 6136 Wh L^{-1} as well.[5] Moreover, the zinc-air battery uses aqueous alkaline electrolyte, which is immune to fire hazard and more safety.[6]

In fact, low-rate primary zinc-air batteries have been commercialized and used in powering hearing aids and navigation lights, etc. For rechargeable zinc-air batteries, however, their practical application is still challenging. The main issues are its low capacity retention and poor

cycling performance resulted from zinc dendrite formation, structural change during zinc regeneration and the inefficient catalysis performance of the air electrode. [7,8]

Due to the complexity of these problems, in this study, we focus only on the inefficient oxygen catalysis issue in zinc-air battery. In other words, this research will focus on the development of efficient and durable bi-functional oxygen electrocatalysts, which are responsible for catalyzing both the oxygen reduction and evolution reaction (ORR-OER) at the air electrode. As mentioned earlier, the lack of such active, stable and low-cost bi-functional catalysts represents one of the major challenges in the development of rechargeable zinc-air batteries.[9,10]

In the past years, extensive efforts have been devoted to the development of efficient and stable ORR-OER bi-functional catalysts, aiming to promote the sluggish oxygen electrochemical reactions, and thus reduce the overpotentials of ORR and OER reaction.[11,12] Now, the best-performing ORR catalysts are Pt-based noble metals such as its alloys,[13-15] and Ru/Ir oxides have been exhibiting excellent activity for OER.[16] However, the high cost of these precious metals and poor bi-functionalities have limited their practical applications in zinc-air batteries. Therefore, the focus of this filed is on the development of bi-functional catalysts from earth-abundant elements, such as non-precious transition metal based metal oxide, hydroxide and sulfide, carbon material, and their composite materials.[17-19]

As efficient and durable bi-functional catalysts, the above mentioned non-precious materials should not only have good conductivity and high ORR-OER activities, but also exhibit excellent stability under the strong oxidative potentials of OER. The latter could cause corrosion problem of carbon-based bi-functional catalysts, and therefore affects the durability of the catalysts.[20] On

the other hand, the absence of carbon would result in a low conductivity of catalyst, which hinders electrocatalysis efficiency. Therefore, the appropriate selection and design, e.g. surface engineering, morphology control of electrocatalysts with balanced activity, stability and conductivity is essential for rechargeable zinc-air batteries.

2.2 Zinc-air battery fundamentals and ORR-OER reactions

A typical zinc-air battery comprises of a zinc anode and an oxygen-permeable cathode assembled in alkaline electrolyte. To be more specific, it consists of the following four main parts or components: *i)* the metallic zinc anode, where the zinc redox reaction occurs; *ii)* the alkaline electrolyte that conduct hydroxide ions (OH^-) between the electrodes; *iii)* the air cathode that composes of oxygen electrocatalysts toward ORR and OER reactions; *iv)* a membrane separator, e.g. a microporous polypropylene membrane, which not only can act as a physical barrier against potential zinc dendrite penetration, but also allows the transportation of OH^- between the two electrodes.

Figure 2.1 shows a schematic of a rechargeable zinc-air battery. One can see that, during discharge, electrons and zinc ions were released at the zinc anode, generating electrical power. The released electrons go through an external load to reach the air cathode, where atmospheric oxygen is reduced to OH^- by receiving the electrons through ORR reaction (Eq. 2-1). In fact, the ORR reaction occurs at the gas/catalyst/electrolyte triple phase boundary in the air cathode. Thus, an important catalyst design strategy is to make it into a porous structure easily accessible to atmospheric O_2 in alkaline electrolyte, which would benefit the overall performance of the zinc-air batteries. To complete the circuit, during discharge, the OH^- ions are migrated to the zinc electrode and then react with metallic zinc forming $Zn(OH)_4^{2-}$ ions (Eq. 2-2). The $Zn(OH)_4^{2-}$

ions are not stable and can be decomposed into ZnO (Eq. 2-3) and the H_2O returns to the electrolyte.

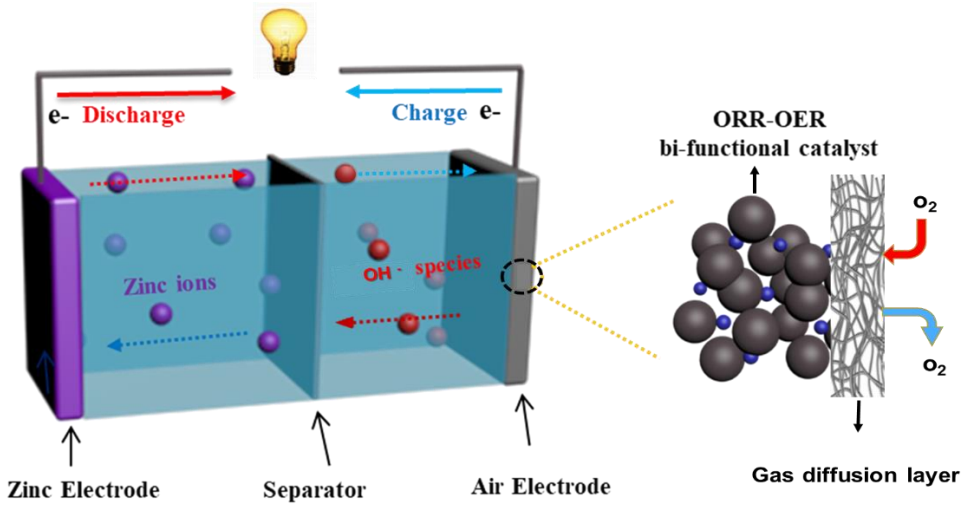

Figure 2.1 Schematic illustrations of a rechargeable zinc-air battery.

The air electrode reaction:

$$O_2 + 2H_2O + 4e^- \Leftrightarrow 4OH^-, \quad E = +0.40\ V \ \text{vs. SHE} \tag{2-1}$$

The zinc electrode reactions:

$$Zn + 4OH^- \Leftrightarrow Zn(OH)_4^{2-} + 2e^- \tag{2-2}$$

$$Zn(OH)_4^{2-} \Leftrightarrow ZnO + 2OH^- + H_2O \tag{2-3}$$

$$Zn + 2OH^- \Leftrightarrow ZnO + H_2O + 2e^-, \quad E = -1.25\ V \ \text{vs. SHE} \tag{2-4}$$

The overall reaction:

$$2Zn + O_2 \Leftrightarrow 2ZnO, \quad E = 1.65\ V\ \ vs.\,SHE \qquad (2\text{-}5)$$

During the charging process, the zinc-air battery stores electric energy through OER reaction (backward reaction in Eq.2-1). The OER reaction occurs at the electrode-electrolyte interface, whereas zinc is deposited at the zinc electrode surface (backward reaction in Eq.2-4). The overall reaction during zinc-air battery discharge and charge was shown in Eq.2-5. The theoretical equilibrium potential of this reaction is 1.65 V, but it is reduced to 1.35–1.4V in the operating cell due to the activation, ohmic and concentration loss.[21]

The catalytic ORR reaction in the alkaline medium proceeds in several steps: gaseous oxygen diffusion from the atmosphere to the catalyst surface, oxygen absorption on the catalyst surface, electrons transfer from the electrode to oxygen, activation or breaking of the oxygen bond, and the formation and sequent removal of OH^- from the catalyst surface to the electrolyte. Oxygen can be reduced to OH^- by direct 4-electron pathway or to peroxide by 2-electron pathway (see equations 2-6, 2-7). The most desirable one for ORR is the 4-electron pathway.[22]

$$O_2(g) + 2\ H_2O(aq) + 4e^- \rightarrow 4\ OH^-(l) \qquad (2\text{-}6)$$

$$O_2(g) + H_2O(aq) + 2e^- \rightarrow HO_2^-(l) + OH^- \qquad (2\text{-}7)$$

The strong bond energy (498 kJ mol^{-1}) of the oxygen molecule makes ORR reaction kinetics unfavourable to proceed.[23] On the other hand, OER reaction is also very complex and involves multiple sequential electron transfer steps as well as oxygen-oxygen bond formation. The reaction of OER is also very slow and kinetically sluggish.[24] Thus, the electrochemical conversion efficiency in zinc-air batteries is limited by the “high-activation barrier” of ORR-OER reactions. In electrochemistry, such activation barrier is usually referred to as overpotential.

Therefore, the development of highly active catalyst towards both ORR and OER is to lower their overpotentials. In addition, as mentioned in Section 2.1, the strongly oxidizing potentials of OER might cause structural damage or degradation of the catalyst, and thus also impose a big challenge for the stability or durability performance of the oxygen electrocatalysts. Accordingly, an efficient ORR-OER bi-functional catalyst would have the following features: high activity for both ORR and OER; high electrical conductivity; good electrochemical stability even under the high oxidative electrode potentials.

2.3 ORR-OER bi-functional electrocatalysts

As mentioned before, the scarcity, high cost and poor ORR-OER bi-functional activities of Pt and Ir/Ru based precious metals prohibited their practical application in rechargeable zinc-air batteries. Therefore, in the past decades, various non-precious ORR-OER bi-functional catalysts have been developed, which can be divided into two main categories: *i)* hybrids of transition metal-based materials (oxides, chalcogenides, nitrides, carbides) and carbon materials; *ii)* metal-free carbon-based catalysts. A brief introduction of these bi-functional catalysts is presented in this section.

2.3.1 Transition metal/carbon hybrid catalysts

Transition metal oxides including Mn, Co, Ni, and Fe, have been extensively explored as ORR-OER bi-functional electrocatalysts in the form of single, binary or ternary spinel oxides ($A_xB_{3-x}O_4$), such as Co_3O_4, $NiCo_2O_4$ and $Co_xMn_{3-x}O_4$, etc.[25] Additionally, perovskite-type metal oxides with a formula of ABO_3, such as $La_{0.6}Ca_{0.4}CoO_3$, have been reported capable of simultaneously catalyzing both ORR and OER reaction.[26,27] The advantages of using metal oxides as electrocatalysis materials lie on *i)* their structural diversity that allows it to be mixed or

doped, and therefore their electronic structure and ORR-OER activities can be tuned through metal cations replacement or exchange, etc.;[28] ii) they have sufficient stability in oxidative electrochemical environments.[29,30] However, they also have some intrinsic drawbacks. For example, most of these reported oxides, e.g. Co_3O_4, exhibit good OER activities, but poor ORR performance.[28] Meanwhile, metal oxides catalysts usually have low electronic conductivity, which limits their utilization as an air electrode catalyst.

To overcome this problem, conductive carbon materials such as graphene, carbon nanotubes, and carbon black are commonly added as the catalyst support.[31] Many studies have demonstrated that the hybrids, metal oxides with carbon materials, are an effective approach to improve the catalytic activity of ORR-OER.[32,33] A recent study reported by Zeng et al.[34] represents a typical effort in the development of such carbon-hybrid catalysts, in which a free-standing cobalt oxide/nitrogen-doped CNT (Co_3O_4/N-CNT) composite aerogel was prepared by anchoring Co_3O_4 inside of an interconnected, conductive CNT aerogel film. The composite aerogel film shows high bi-functional catalytic activities for ORR and OER, and therefore was as an air electrode for flexible zinc-air batteries.

In addition to metal oxides/carbon hybrids, metal hydroxide and chalcogenides/carbon composites are also investigated in ORR-OER.[35,36] For example, Qian et al.[37] found that NiCoFe trinary layered double hydroxides (LDHs) show modest bi-functional ORR/OER activities. Recently, Wang and co-workers[38] developed a highly efficient bi-functional electrocatalyst by depositing 3-5 nm NiFe-LDH nanoparticles on Co, N-codoped carbon nanoframes (Co,N-CNF). The NiFe-LDH/Co,N-CNF electrocatalyst displayed an OER overpotential of 0.312 V at 10 mA cm^{-2} and an ORR half-wave potential of 0.790 V, showing excellent ORR-OER activities. In that study, the high performance of the LDH/carbon

electrocatalyst as considered originated from the high electrical conductivity and excellent ORR activity of Co, N-CNF, together with the highly OER active ultrafine (3–5nm) NiFe-LDH nanoparticles. In addition to the LDHs, chalcogenides such as Co_9S_8 nanoparticles anchored into an N, S co-implanted three-dimensional carbon matrix (Co_9S_8@NSCM) was found highly active towards ORR-OER electrocatalysis.[39] Noted that, recently, there are studies report that metal chalcogenides and hydroxides are thermodynamically less stable than metal oxides under strongly oxidizing conditions of OER. This has triggered the studies on real OER catalytic phase in transition metal-based catalysts.[40-45] For example, Hu et al.[45] found that NiSe was completely converted into $Ni(OH)_2$ crystal after OER reaction under alkaline conditions, and the latter was claimed as the real OER catalyst. Recent synchrotron radiation X-ray absorption and in-situ Raman spectroscopy analysis indicates that, during OER, there is a dynamic conversion between Co_3O_4, $Co(OH)_2$ and CoO(OH) species.[46,47] All of these studies highlight the importance of post-OER characterization of the as-prepared bi-functional catalyst to identify the real catalytic OER component.

2.3.2 Metal-free catalysts

Metal-free materials as bi-functional catalysts toward both ORR and OER were also reported, among them the heteroatom (N, S, P,) doped carbon-based materials represents the primary class of metal-free catalysts in alkaline medium.[48,49] It is believed that catalytic activities of these carbon-based metal-free catalysts are primarily attributed to its large specific surface area and the unique electronic structure, for which the integration of N, S, P heteroatoms can efficiently tune the electronic structure of the surrounding carbon atoms and control the local charge density.[50] For example, Yang et al.[51] synthesized a metal-free catalyst that consists of three-dimensional (3D) graphene nanoribbon networks (N-GRW) doped with nitrogen. This carbon-based 3D N-

GRW material was found exhibits good bi-functional electrocatalytic activities for both ORR and OER. Moreover, that study experimentally demonstrated that the electron-donating quaternary N sites were responsible for ORR, whereas the electron-withdrawing pyridinic N moieties in N-GRW served as active sites for OER. Although, these carbon-based catalysts have an intrinsic drawback: they are susceptible to electrochemical corrosion. Therefore, the proposed research will focus on the development of efficient and durable bi-functional catalyst based on non-precious metal oxides/nitrides.

2.4 Oxygen electrocatalysts design strategies

In the previous sections, a brief summary of the ORR-OER bi-functional catalysts materials has been given. In this section, we present a short discussion on the strategies used to design or engineer the material structure and properties for efficient and durable bi-functional oxygen catalysis performance.

2.4.1. Coupling strategy on enhanced bifunctionality

One promising strategy to achieve catalyst bifunctionality is by integrating ORR- and OER-active components into a favourable nanostructure. To this end, a core-corona structured bi-functional oxygen catalyst consisting of $LaNiO_3$ and nitrogen-doped carbon nanotubes (NCNTs) was explored.[52] In this coupled catalyst, each NCNT serves as an ORR-active component anchored on the OER-active $LaNiO_3$ core. The coupling effect arising from the core-corona structure provides the key to exemplary bi-functional activity of the catalyst compared with state-of-the-art Pt/C and $LaNiO_3$ catalysts. Likewise, nitrogen-doped graphene when chemically coupling with other transition metal oxides such as perovskite (e.g., $La_{0.5}Sr_{0.5}Co_{0.8}Fe_{0.2}O_3$) and spinel (e.g., Co_3O_4) has shown improved catalytic activity for ORR-OER.[53-55] Although the

reaction mechanisms associated with the actual bi-functional active sites in these hybrid catalysts remains unclear, the metal-N bonds derived from synergistic coupling of nanomaterials were found to be the crucial factor for the ORR and OER enhancement.[56] For instance, higher ORR and OER activities were achieved by a Co_3O_4/N-doped graphene hybrid catalyst in comparison to those of Co_3O_4/graphene and Co_3O_4 due to the formation of interfacial Co-N bonds between Co_3O_4 and N-doped graphene.[57] The coupling strategy has also been extended to chemical bonding of WS_2 on carbon nanotubes via tungsten carbide bonding, which provides efficient pathways for transferring electrons by spin polarization to facilitate the ORR/OER catalytic process.[58]

2.4.2. Oxygen vacancy enhanced activity in metal oxides

As discussed in Section 2.3.1, transition metal oxides with spinel or perovskite crystal structure have been demonstrated as promising bifunctional catalysts for oxygen redox in alkaline solutions. In addition to downsizing and nanostructuring metal oxides to improve mass activity, their catalytic performance can also be significantly enhanced by modifying the surface electronic structure to yield high intrinsic activity. Oxygen vacancy has been regarded as an important tool to influence the surface electronic structure and thus catalytic activity.[59,60] They can be created in the metal oxide crystal lattice by method such as argon plasma treatment and post-heat treatment under reducing environment.[61-63] Removal of an oxygen atom from the metal oxide lattice will result in electron delocalization on metal cations neighbouring the vacancy site, which would enhance the exposure of active sites and charge transfer to promote catalyst performance.[64] For instance, mesoporous Co_3O_4 nanowires were reduced by $NaBH_4$ treatment leaving oxygen vacancies on the nanowire surface. Relative to pristine Co_3O_4 nanowires, the reduced Co_3O_4 nanowires contain an increased portion of OER-active Co^{2+}

oxidation state associated with oxygen vacancy formation, resulting in enhanced OER activity due to increased number of active sites and electronic conductivity.[65] Moreover, the capability to control and confine oxygen vacancies on desirable facets will be important to realize the full potential of transition metal oxide as bi-functional catalysts. For example, Ling et al.[66] developed a one-dimensional single-crystal CoO nanorod (NRs) with desired facets and vacancy defects. The study reported that, compared with other facets of CoO, the oxygen vacancies present on the oxygen-terminated {111} nanofacets ({111}-Ov) of CoO NRs are effective for enhancing charge transfer and assuring optimal adsorption energies for intermediates of the ORR and OER. As a result, the intrinsic ORR and OER activities of CoO NRs with defect-rich {111}-Ov facets exceeded those of polycrystalline CoO NRs by factors of 7.2 and 2.6, respectively. Besides the formation of oxygen vacancies, filling the oxygen vacancies in defect-rich CoO with sulfur was also demonstrated effective for improving the electrocatalytic performance.[67]

2.4.3. Heteroatom dopants improved activity in carbons and chalcogenides

The rational doping of heteroatom (e.g. N, S, P, B and Se) has also emerged as a promising strategy to design carbon-based metal-free bi-functional oxygen catalysts in alkaline media.[68] The introduction of such dopants in carbons can either donate electrons or generate holes to fine-tune electronic properties of adjacent carbon atoms and thus generate catalytic active sites for ORR and OER.[69] By doping carbon with more electronegative heteroatoms such as N, a net positive charge is created on surrounding carbon atoms, which improves the chemisorption of oxygen and electron transfer, leading to enhanced catalytic activities for ORR-OER.[70] On the other hand, there are studies reported that doping heteroatoms, which are less electronegative (e.g., B) into graphene, will create positively polarized active sites for catalytic process.[71] In addition to single atom doping, binary (e.g., N/S, N/B, and N/P) and ternary (e.g., N/B/P and

N/F/B) doping of nanostructured carbon catalysts have been demonstrated to improve catalyst performance,[72] which can be attributed to the synergistic electronic interactions between the different dopants and adjacent carbon atoms.[73]

In addition to carbons, transition-metal chalcogenides can be doped with heteroatoms such as P and N, improving their catalytic activity and stability substantially.[74,75] For example, Hao et al. [76] introduced N dopants to CoS_2 nanospheres via a hydrothermal reaction. The N doping can have a positive influence on the electronic density and configurations of CoS_2 nanospheres, which minimize the reaction barriers and thus make the N-enriched CoS_2 nanospheres highly efficient OER catalysts. Guo et al.[77] prepared (N, P)-doped CoS_2 nanoclusters that were embedded inside TiO_2 nanoporous films. The resulting catalyst exhibited improved electrocatalytic ORR/OER activities in an alkaline electrolyte (onset potential of 0.91 V for ORR and 1.41 V for OER *vs*. reversible hydrogen electrode, RHE) that were 50 and 160 mV higher than that of CoS_2 nanoclusters. The improvement was largely due to a decrease in charge transfer resistance of the CoS_2 nanoclusters after doping of N and P.

2.4.4. Corrosion resistant supports

As mentioned previously, to ensure the good conductivity and large surface area of the oxygen electrocatalysts, the best-performing redox catalysts are usually composited with carbon materials, such as carbon nanotubes, and graphene. However, the highly oxidative operating condition of rechargeable zinc-air batteries can cause significant oxidation or corrosion of these carbon-based or supported bi-functional catalysts. This would cause severe issues in the stability of the catalysts especially for those under harsh ORR-OER operating conditions: *i)* the mass losses of the carbon would lead to agglomeration of the supported nanoparticle catalyst; *ii)* the

formation of surface C-O groups would lower the conductivity of the catalysts. All of these will degrade the performance of the batteries.

To alleviate the corrosion problem, some strategies have been proposed. One common approach is to use metal oxides as support. For example, 3DOM structured Co_3O_4 supported Pd catalyst (Pd@3DOM-Co_3O_4) was reported can exhibits good ORR-OER activity and superb stability (Figure 2.2a).[78] In such a catalyst, the Co_3O_4 support is actually active component towards the oxygen reactions, especially for OER, whereas the Pd is an ORR active phase. The zinc-air battery equipped with such Pd@3DOM-Co_3O_4 catalyst could stably operate for 300 charge/discharge cycles for 50 h (10 min per a charge/discharge cycle), outperforming 3DOM-Co_3O_4, Pt/C, and Ir/C (Figure 2.2b). In addition to the oxygen electrocatalysis active support, corrosion-resistant TiO_2 support has also been developed. The TiO_2 support is not active for both ORR and OER, but used to firmly anchor Pt catalyst through strong metal-support interaction, showing improved ORR activity and durability.[79] Recently, TiN has been investigated as conductive electrocatalyst support materials for ORR.[80] For these supporting materials, both the active Co_3O_4 and inactive TiO_2 oxides support have an intrinsic low-conductivity drawback and therefore hinders the electrocatalysis efficient. TiN is conductive but not suitable to firmly "hold" the active supported catalysts due to its non-defective surface structure. Thus, practical catalyst support materials must be designed such that their surfaces inhibit excessive oxidation and/or are concealed by conductive oxide layers.

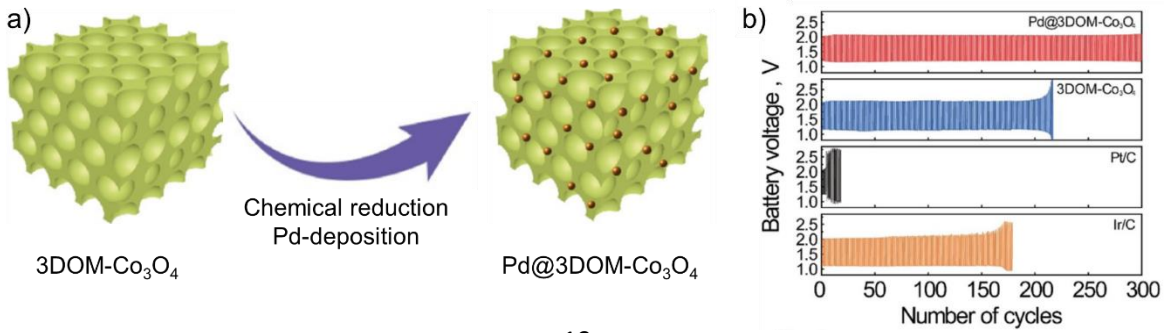

Figure 2.2 (a) Schematic conversion of Pd-deposited 3D ordered mesoporous spinel cobalt oxide (Pd@3DOM-Co_3O_4). (b) Charge-discharge cycling performance of the rechargeable zinc-air battery using Pd@3DOM-Co_3O_4, 3DOM-Co_3O_4, Pt/C and Ir/C obtained with a 10 min cycle period and applied current density of 10 mA cm^{-2}. Reproduced with permission.[78]

In summary, due to their low cost and good catalytic activity, transition metal-based materials, such as oxides, chalcogenides are promising ORR-OER bi-functional catalysts. In particular, when they are hybrid with carbon materials or undergoes surface engineering treatment, the transition metal/carbon composites usually exhibit excellent ORR-ORR activity. However, the challenge of carbon-containing bi-functional catalysts is the oxidative potentials of OER, especially when carbon was used as supporting material, for which the oxidation of carbon support would deteriorate the catalytic performance of the hybrid catalysts. Meanwhile, during OER reaction, the oxidation of the transition metal surfaces could also occur. In addition to the stability issue, it raised a question in the electrochemical community that what is the real catalytic phase for OER reaction. Therefore, the design of efficient and durable ORR-OER bi-functional catalysts for zinc-air batteries should include: *i)* a careful selection of conductive support, and active transition metal materials; *ii)* a rational morphology design to maximize the exposure of active sites; and *iii)* an in-depth understanding on the real catalytic phase under OER working conditions.

CHAPTER 3

Experimental Methods and Characterization Techniques

This chapter provides general descriptions of the characterization techniques and electrochemical analysis methods used in this study. More detailed information on specific nanomaterials synthesis procedures and electrochemical evaluation parameters are given in the experimental methods section included in each chapter.

3.1 Electrochemical testing methods

3.1.1 Rotating disk electrode (RDE) test

RDE is a working electrode used in three-electrode half-cell testing system, in which the electrode rotates during experiments to study electrochemical activity of various redox catalysts. Figure 3.1a shows the typical RDE testing set-up. The working electrode (glassy carbon disc) rotates in a glass cell filled with an electrolyte. The counter electrode, e.g. a graphite rod, is used to complete the circuit. The reference electrode allows for electrode potential measurement and control versus a standard electrode potential. The catalysts or active materials are coated on the glassy carbon electrode (Figure 3.1b). During ORR and OER testing, the three electrodes are immersed in the oxygen/nitrogen saturated 0.1M KOH electrolyte solution, respectively. For instance, in a typical measurement of ORR activity, the potential of the working electrode is swept from 0 to -1.0 V vs. SCE at the rate of 10 mV s^{-1} in oxygen saturated electrolyte condition. At the same time, the electrode is continuously rotated (i.e., at 900 rpm) to induce convective electrolyte flow that ensures a steady supply of oxygen saturated electrolyte to the catalyst layer (Figure 3.1b).

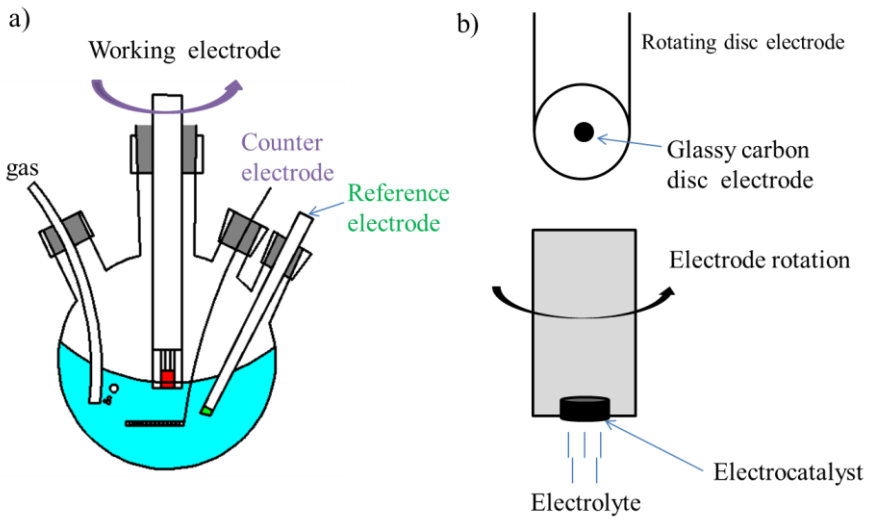

Figure 3.1 Schematic diagram of a) Standard three-electrode cell used for RDE measurements; b) Rotating disc electrode upon which the catalyst is deposited**.**

3.1.2 Cyclic voltammetry (CV) and linear sweep voltammetry (LSV)

Both CV and LSV are potentiodynamic electrochemical measurement techniques used to analyze the electrochemical signatures of catalysts under investigation. CV refers to a method where the electrode potential is swept repeatedly at a constant scanning rate (mV s^{-1}) (i.e., 10 mV s^{-1}) and a certain rotation speed (i.e., 900 rpm) within a desired potential window while LSV involves sweeping from an initial value to a final value. In a typical measurement of the ORR activity, the electrode potential is swept from 0 V to -1.0 V vs. SCE in an oxygen-saturated 0.1 M KOH electrolyte cell at a certain rotation speed while the potential range for OER is 0 V to 0.9 V vs. SCE. Then the electrode potential was calibrated with respect to an RHE, for unified evaluation of catalytic activity, according to Equation 3-1.

$$E_{RHE}=E_{SCE} + 0.244\ V + 0.591 \times pH \text{ at } 25\ ℃ \quad (3\text{-}1)$$

Or, the calibration can be performed in the high purity hydrogen saturated electrolyte with a Pt wire as the working electrode and measuring the voltage ΔE between the two electrodes. An example rotating disc voltammogram of 3D graphene aerogel-supported Ni/MnO catalyst in 0.1 M KOH solution is shown in Figure 3.2. An efficient bifunctional oxygen electrocatalyst should minimize the overpotential for both the ORR and OER, allowing for an ideal reversible oxygen electrode.

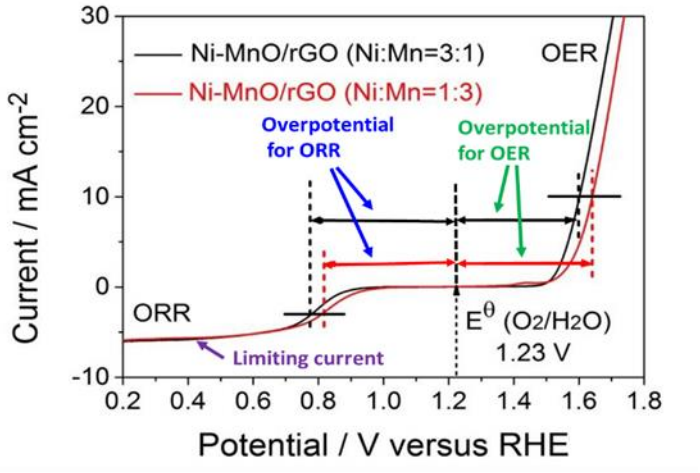

Figure 3.2 The overall LSV polarization curves of the catalysts with different Ni/Mn ratios within the ORR and OER potential window (Rotation rate: 1600 rmp; Sweep rate: 5 mV s^{-1}).[1]

3.1.3 Galvanodynamic charge and discharge testing

The charge-discharge properties of the zinc-air batteries equipped with the ORR-OER catalysts can be measured by the galvanodynamic technique. The galvanodynamic tests were performed by applying a current range of 0 A to a target value at a fixed current rate (A s^{-1}), and at the same time, the cell potentials of the air cathode versus the zinc anode were measured. As a

result, the polarization curves associated with the catalytic oxygen reaction were obtained (Figure 3.3), which can be used to determine the overpotentials of oxygen electrocatalysis process and the resistances that arise from the battery operation.

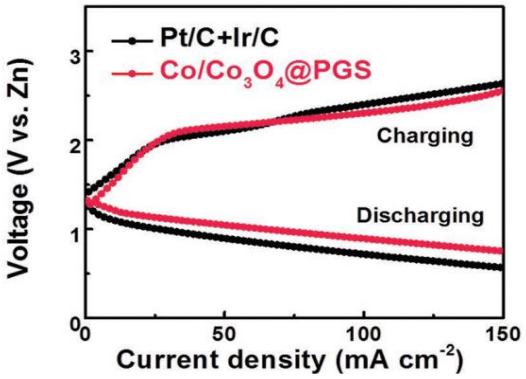

Figure 3.3 Typical charge and discharge polarization curves for zinc-air battery.[2]

3.1.4 Galvanostatic cycling

Galvanostatic cycling is an electrochemical technique that is usually used to evaluate the durability performance of the oxygen electrocatalysts. During the cycling test, a repeated cycle of fixed current is applied in alternating polarity for a period of time, and the cell potential was recorded (Figure 3.4). The fixed current is the same magnitude but with opposite polarity to obtain the charge and discharge regimes of the batteries. Both pulses cycling and extended cycling test can be performed by varying the time interval for each cycle. The rechargeability of the battery can be evaluated by a pulse cycling in short intervals, whereas extended cycling determines the more practical cycling capabilities of the battery. The repetition of such process will allow us to track the change of cell potential during the charge and discharge of batteries, indicative for the stability of the air cathode or catalysts.

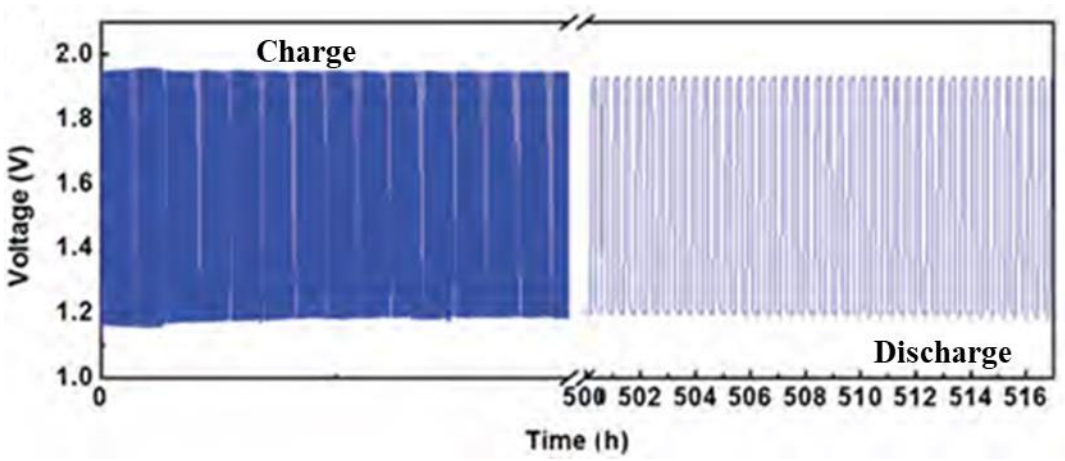

Figure 3.4 Typical galvanostatic discharge/charge battery cycling test.[3]

3.2 Characterization techniques

3.2.1 X-ray diffraction (XRD)

XRD is a technique primarily used to identify the crystal structure of crystalline material and can provide information on atomic spacing, bulk composition, etc. Based on constructive interference of directed X-rays and crystalline sample, diffraction patterns at the angles corresponding to specific crystal planes will be generated.[4] This is made possible by the fact that the wavelength of X-ray is typically the same order of magnitude (1–100 angstroms) as the spacing between atomic planes in the crystalline, and the constructive interference occurs only when the conditions satisfy Bragg's law, as shown by Equation 3-2 below.

$$n\lambda = 2d\sin\theta \qquad (3\text{-}2)$$

where n, λ, d, and θ represent the order of the spectrum (any integer), the wavelength of the X-rays, the lattice spacing, and the diffraction angle, respectively. Since each mineral has its

featured diffraction patterns or d-spacing, a comparison of measured patterns or d-spacing with standard reference patterns will allow us to identify the crystalline sample.

3.2.2 Scanning electron microscopy (SEM)

SEM is an important imaging instrument. It uses signals that derive from electron-sample interactions at the surface of solid specimens to image the morphology and topological characteristics of micro-scale and nano-scale materials. To be more specific, the working principle of SEM is to scan the sample with an extremely high-energy narrow electron beam, and a variety of signals are generated through the interaction between the electron beam and the sample surface. Among these signals, the secondary electrons and backscattered electrons are used to show morphology and topography on sample surface.

3.2.3 Brunauer–Emmett–Teller (BET) method

Brunauer–Emmett–Teller (BET) theory aims to explain the physical adsorption of gas molecules on a solid surface and serves as the basis for an important analysis technique for the measurement of the specific surface area of materials.[5] BET theory builds upon the foundational Langmuir adsorption theory, which provides a model for monolayer molecular adsorption, and extends this theory to multilayer adsorption using three assumptions:

1. Gas molecules can adsorb on a solid surface in an infinite number of layers;
2. Individual adsorption layers do not interact with one another; and
3. Langmuir theory can be applied to each individual adsorption layer.

These three assumptions form the basis for the BET equation shown below (Equation 3-3):

$$\frac{1}{v[\left(\frac{p_0}{p}\right)-1]} = \frac{c-1}{v_m c}\left(\frac{p}{p_0}\right) + \frac{1}{v_m c} \tag{3-3}$$

where p_0 and p are the saturation and equilibrium pressure of adsorbates at a given temperature, v and v_m are the total adsorbed gas and monolayer adsorbed gas quantity, and c is the BET constant. By measuring the pressure and total gas adsorption at a given temperature, a plot showing $1/v[(p_0/p)-1]$ vs. $\phi = p/p_0$ can be created. Finding the slop and y-intercept of this data allows the monolayer adsorption v_m and BET constant c to be calculated. Once these values are found, the total specific surface can be derived based on the cross-sectional area of the adsorbate species and the mass of the sample used for characterization. In this research, BET is used to identify the surface area and pore volume of the developed 3DOM metal oxide/nitride/sulfide composites.

3.2.4 Transmission electron microscopy (TEM)

TEM is a microscopy technique that allows direct visualization of materials morphology at nanometer scale. High resolution TEM (HRTEM) imaging can even shows morphology of the sample at atomic level. In TEM, a beam of electrons is transmitted through an ultra-thin specimen (<100 nm) or a suspension on a grid, interacting with the specimen as it passes through it. Based on electron diffraction theory, the signals from the collected diffracted electrons can be projected to a high resolution image of the sample. TEM is a powerful tool for material science, and widely used in imaging the internal structure, atomic arrangements and crystal orientation of nanomaterials.

As discussed above, in TEM, the images are formed by electrons passing through a thin specimen. However, if the electron beam is focused to a fine spot (0.05-0.2 nm), and then

scanned over the sample in a faster pattern.[6] This would generate a scanning transmission electron microscopy (STEM) image of the sample, providing atom-by-atom information of the materials. More importantly, the electron energy loss spectroscopy (EELS) in STEM is a powerful tool to distinguish elements and identify the oxidation states of metal atoms. The combined STEM and EELS analysis would provide accurate information on the inter-atomic structure and chemical properties of the materials.

3.2.5 Energy dispersive x-ray spectroscopy (EDS)

EDS is a technique used for the elemental analysis of a specimen. In EDS, the surface of a sample was bombarded by a high-energy electron beam, which may lead to an X-ray excitation. The energy of the X-rays emitted from a sample is a characteristic of the emitting element with a unique atomic structure. Accordingly, the elements in the specimen can be determined. Moreover, the intensity distribution of the scattered X-rays is used to determine the distribution of the corresponding element, and thus the elemental composition of the sample was measured.

3.2.6 X-ray photoelectron spectroscopy (XPS)

XPS is a surface characterization technique used to determine the functional groups, elemental composition, and chemical state of the sample surface. Typically, X-rays of a fixed energy is used to de-irradiate the sample, causing the inner electrons of the atom to be excited to emit. The amount of electrons escaping from the surface of the material (up to 10 nm) can be detected and analyzed based on the electron binding energy. Then, the elements on the surface of the material can be identified through the featured relationship between the energy spectrum and the number of electrons. In other words, XPS determines the elements and the quantity of those elements of the sample surface as well. In addition, XPS is also a unique and valuable tool for

understanding surface chemistry (local bonding environment of a species) of a material by analyzing the shift of the bonding energy of the element, referred to as “chemical shift”.

CHAPTER 4

Two-dimensional Carbon-supported Cobalt Sulfide Bi-functional Electrocatalyst

In this chapter, we developed an efficient two-dimensional carbon-supported cobalt sulfide bi-functional catalyst, which consists of surface decorated, e.g. oxidation and nitrogen doped, cobalt sulfide supported on N-doped reduced graphene oxide (O-N-Co_9S_8@N-RGO). The ORR/OER activity and stability of this composite catalyst were evaluated. The results show that O-N-Co_9S_8@N-RGO possesses excellent bi-functional activity especially for oxygen evolution reaction (OER), and exhibits good stability over 900 charge-discharge cycles at 10 mA cm^{-2} in zinc-air battery. Moreover, the real OER catalytic phase of this material was identified: we found that O-N-Co_9S_8 was completely converted into Co_3O_4 after OER, showing oxide is actual active phase for OER reaction. Furthermore, we propose and demonstrate that oxides in-situ generated during OER are more active than the directly calcined oxides. This work advances fundamental insight of metal chalcogenides "catalysts" and guides the design of active bi-functional catalysts. This chapter is organized as follows: Section 4.1 presents a background and motivation of this study. Details about the experimental characterization and analysis are described in Section 4.2; Results and discussions are presented in Section 4.3. A summary of this work is provided at the end of this chapter.

4.1. Introduction

The development of efficient bi-functional electro-catalysts for both ORR and OER is of critical importance for rechargeable zinc-air batteries. Precious metals such as Pt, Ir, Ru are the best performing catalysts for oxygen electro-catalysis in alkaline.[1, 2] However, the scarcity and

poor catalytic bi-functionality hinder their application in zinc-air batteries. The most promising non-precious bi-functional catalysts are derived from carbon-transition metals (e.g. Co, Ni, Fe, Mo, etc.) hybrid materials.[3] The carbon, as support, ensures the good conductivity of the catalysts, and when doped with N, S or transition metal elements, e.g. Fe, Co, it shows excellent ORR activity.[4] On the other hand, the transition metals, especially their oxides, hydroxides, phosphide, sulfide or nitride can exhibit good OER activities.[5-8]

Recently, surface engineering, e.g. NH_3 etching, cation or anion substituting, heteroatom doping, of transition metal chalcogenides and nitrides can effectively improve their activities, especially towards OER.[9-12] Many studies have attributed the enhancement of catalytic activities to synergistic effect or vacancy sites on these engineered transition metal surfaces.[13-15] However, other studies have reported that, during OER, there exist progressive oxidation of the metal-based materials, [16-20] and the oxidized metal surfaces might be responsible for the catalytic activity.[21,22] These reports raised a question that, in the absence of post-OER characterization of the as-prepared catalysts, the explanations on catalytic activity might be inadequate and sometime non-convincing.[21] On the other hand, these reports also imply that considering surface oxidation in the development of metal chalcogenides catalyst might be also beneficial for OER activity.

Based on the above, in the present study, we have engineered an efficient bi-functional catalyst with excellent ORR-OER activity that consists of mildly oxidized, N-doped imperfect Co_9S_8 crystals supported on N-doped reduce graphite oxide (O-N-Co_9S_8@N-RGO). Meanwhile, the origin of its OER activity (over-potential of 350mV at current density of 10 mA cm^{-2} under 0.1M KOH) was investigated by detailed experimental characterization of the as-prepared

catalysts before and after OER reaction. In addition, although the oxidation O-N-Co_9S_8 crystal during OER is expected, some questions still remain. For example, will high OER activity be maintained (good stability performance) after catalysts oxidation, and why? Addressing these questions will provide in-depth knowledge of the intrinsic OER activity and "stability" of metal chalcogenides and will potentially guide the design of efficient bi-functional catalysts especially with OER activity.

4.2. Experimental section

4.2.1 Preparation of O-N-Co_9S_8@N-RGO composite

Reduce graphene oxide (RGO) is obtained by thermal-shock heat treating graphene oxide (GO) in Ar at 900^{o}C for 1 min, in which the GO was synthesized from graphite powder using modified Hummers method [23,24]. Then, 30 mg of RGO was dispersed in 150 mL of water by ultrasonication for 1 hour. Cobalt nitrate hexahydrate [$Co(NO_3)_2$ $6H_2O$, 655mg] and sodium dodecyl sulfate [SDS, 865mg] were added to the RGO dispersion. Ammonia solution (28-30%, 10mL) was drop-wisely added to the solution with a rate of 5 mL min^{-1} under stirring at room temperature. The above suspension was then put into oil bath at 90 ℃ with stirring for 6 hours under ambient atmosphere. After that, the solution was naturally cooled down to room temperature. The suspended black product was collected by centrifugation and washed with DDI water and ethanol, and then freeze-dried. The as-obtained powder product, referred to as Co-S-O-N-RGO precursor, was thermal-shock treated under NH_3 atmosphere at 700 ℃ in tube furnace for 5 mins, and then cooled down to room temperature in Ar. The resulting product is O-N-Co_9S_8@N-RGO composite.

4.2.2 Preparation of hollow Co_3O_4, O-N-Co_9S_8 and N-RGO

The hollow Co_3O_4 was derived from the following steps: first, 30 g glucose and 0.1 mol $Co(CH_3COO)_2$ $6H_2O$ were dissolved into 300 ml distilled water under vigorous magnetic stirring; then, the solution was transferred into a Teflon container, sealed in autoclave for hydrothermal reaction at 180 ℃ for 400 min. The precipitation product was washed, and centrifuged with distilled water and ethanol for 3 times, respectively. The resulting product was dried at 70 ℃ for 10 h and collected as precursor; finally, hollow Co_3O_4 product was obtained by annealing the precursor at 500 ℃ for 1h in air, with a ramping rate of 1 ℃ min^{-1}. For the synthesis of O-N-Co_9S_8 and N-RGO, the same procedure as in the development of O-N-Co_9S_8@N-RGO composite was used but without the addition of RGO and Co precursor, respectively.

4.2.3 Characterization

X-ray diffraction (XRD) was carried out on a Rigaku D/Max 2550 X-ray diffractometer with Ni-filtered Cu Kα radiation (λ = 1.5418 Å). The morphology of the as-prepared composite was investigated using field emission scanning electron microscopy (FE-SEM) (Zeiss Ultra Plus, United Kingdom), and high-resolution transmission electron microscopy (HRTEM) instrument (FEIPhilips CM 300, United States). X-ray photoelectron spectroscopy (XPS) (Thermo Scientific K-Alpha XPS spectrometer) was used to investigate the chemical composition of the as-prepared composites. Note that, the post-OER characterizations (e.g. XRD, XPS) were performed using the catalysts sprayed on carbon paper. Thus, their XRD figures show some patterns of the carbon background.

4.2.4 Electrochemical activity evaluation

The half-cell electrochemical evaluation of the ORR-OER activity of the as-prepared composites was conducted via rotating disk electrode (RDE) voltammetry using a three-electrode

system and potentiostat (CH Instruments 760D). Ink solution was prepared by mixing the composites and carbon black (Vulcan Carbon XC-72) in a 2:1 mass ratio in 1-propanol solution with a total mass concentration of 4 mg mL^{-1}. The working electrode was prepared by coating the ink onto a polished glassy carbon disk electrode with an active material loading of 0.40 mg cm^{-2}. A graphite rod and saturated calomel electrode (SCE) were used as the counter and reference electrodes, respectively. All potentials were referenced to a reversible hydrogen electrode (RHE) by adding a value of (0.245+0.059×pH) V. The electrolyte is 0.1 M KOH. Cyclic voltammetry (CV) analysis was performed at the scan rate of 50 mV s^{-1}. The ORR and OER activities were measured in the O_2 and N_2 saturated electrolyte, respectively, through LSV at the scan rate of 10 mV s^{-1}. The OER and ORR activity of as-developed catalysts and commercial Pt/C or Ir/C catalysts were normalized by the geometry area of RDE electrode at the same loading. The potentials in OER and ORR were corrected for iR losses and background current, respectively. The latter is the current obtained when N_2 is purged into the electrolyte in ORR test.

4.2.5 Rechargeable zinc-air battery test

The full-cell Zinc-air battery tests were performed using home-made plastic prototypes. Polished Zinc-plate was used as the Zinc electrode. The O-N-Co_9S_8@N-RGO air electrode was prepared by spraying catalyst ink onto the front side of a carbon paper gas diffusion layer (GDL; SGL Carbon 39 BC; Ion Power Inc.) with an active catalyst loading of 0.67 mg cm^{-2}. The catalyst ink is prepared from 2.67mg O-N-Co_9S_8@N-RGO composite, 1.33mg Vulcan XC-72 carbon black, 13.33mg 15 wt% Nafion (LIQUion solution, Ion Power Inc.) and 5.0 mL 1-propanol. Stainless steel meshe was used as the current collector for the air cathode, in which it was placed in contact with the backside of the carbon paper. The current collector for the Zinc

anode is copper foil. The electrolyte is a solution of 6 M KOH and 0.2 M $Zn(CH_3COO)_2$.

4.3 Results and discussion

The O-N-Co_9S_8@N-RGO composite was developed by "thermal shock" heat treatment of the Co, S, N and RGO-containing precursor (Co-S-O-N-RGO) under NH_3 atmosphere at 700 ℃ for 5 min. The merits of such synthesis procedure are: *i)* the thermal shock heat treatment can result in a fast and imperfect Co_9S_8 crystallization process; *ii)* NH_3 as a reduction agent not only prevents the formation of cobalt oxides during calcination, but also provides the N doping source for N-RGO and Co_9S_8 during crystallization. The formation of N-RGO is essential for the ORR activity of the composite. For Co_9S_8 crystallization, the NH_3 treatment would result in S-deficient Co_9S_8 surfaces with distorted bulk crystal structure; *iii)* using RGO rather than GO as precursor component ensures mild oxidation of the Co_9S_8 crystal surfaces when NH_3 atmosphere was changed to Ar right after the thermal shock treatment. A highly oxidized catalyst surface might form calcined cobalt oxides. As discussed later, a mild oxidized and imperfect Co_9S_8 crystal rather than calcined cobalt oxides is more beneficial for OER. These features of the O-N-Co_9S_8@N-RGO composite are confirmed by characterization analyses.

Figure 4.1a and 4.1b show the SEM and HRTEM images of the O-N-Co_9S_8@N-RGO composite, respectively. The two lattice fringes with d-spacing of 0.29 and 0.49 nm in HRTEM indicates that (311) and (111) planes of Co_9S_8 are the exposed catalyst surfaces. Hereafter, these two surfaces are referred to as O-N-Co_9S_8 (311) and O-N-Co_9S_8 (111). TEM-ELLS mapping of the O-N-Co_9S_8@N-RGO composite clearly indicates the N-insertion in the bulk Co_9S_8 crystal (Figure 4.1c), in which Co, S and N are uniformly distributed within the particle. The O element, however, was found on both the RGO sheet and the outer surface of O-N-Co_9S_8 particle,

suggesting surface oxidation of the Co_9S_8 crystal.

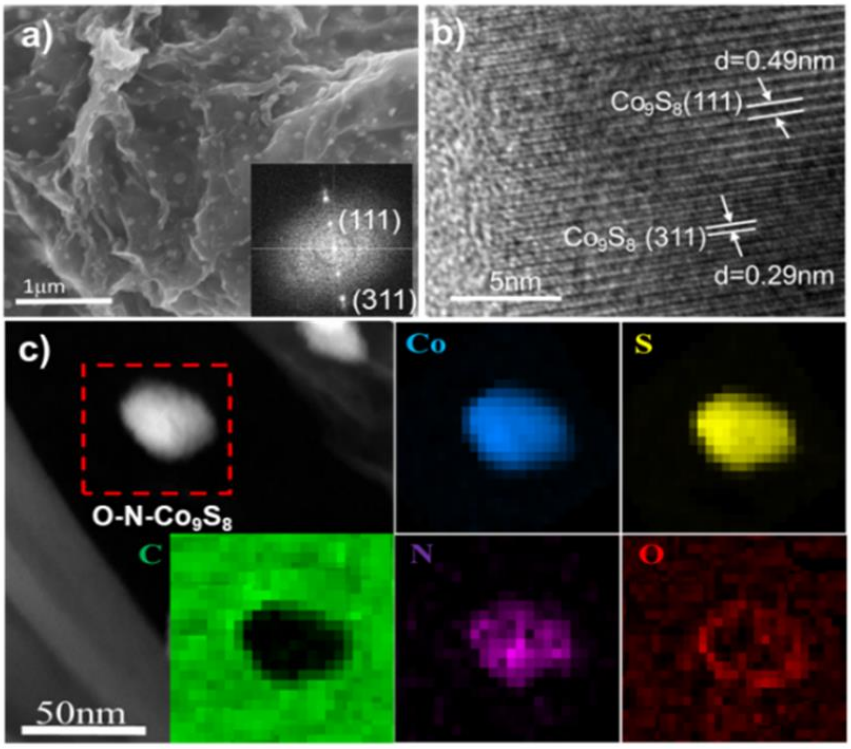

Figure 4.1 a) SEM; b) HRTEM images, and c) TEM-Electron energy-loss spectroscopy (TEM-EELS) mapping images of O-N-Co_9S_8@N-RGO before OER reaction.

The formation of distorted cubic Co_9S_8 crystal was confirmed by XRD characterization (Figure 4.2). As compared with the standard pattern of cubic Co_9S_8, the characteristic peaks of O-N-Co_9S_8@N-RGO were slightly shifted to higher angle, especially for the peak around 52 °, suggesting a small shrinkage of the Co_9S_8 crystal. This shrinkage might have been caused by the smaller atomic radius of doped N (65 pm) than S (88 pm). A profile fitting of the O-N-Co_9S_8 peaks with standard cubic Co_9S_8 (lattice parameter: a=9.927 Å) gives a residual error of 6.69%. The calculated lattice parameter of O-N-Co_9S_8 is found to be a=9.825Å, verifying the shrinkage of its cubic structure.

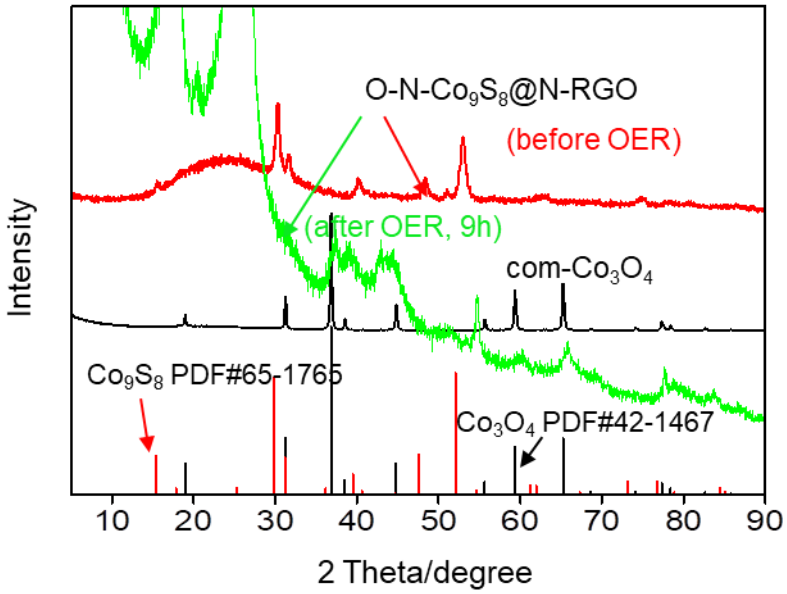

Figure 4.2 XRD patterns of the O-N-Co_9S_8@N-RGO catalyst before and after 9h OER half-cell test at a constant potential of 1.60V *vs.* RHE.

In the Co 2p XPS spectra of O-N-Co_9S_8@N-RGO composite (before OER), there is a sharp Co $2p_{3/2}$ peak around 778.3eV (Figure 1e). This peak is very close to that of metallic Co (777.9 eV), suggesting the reduced nature of the Co_9S_8 surface.[25-27] In the S 2p spectrum (Figure 1f, before OER), the peak at 161.4 eV and 162.5 eV agrees with the $2p_{3/2}$ and $2p_{1/2}$ state in Co-S bond. The minor O-Co peak (530.1 eV) in the O1s spectrum (Figure 1g, before OER) indicates that its surface is only slightly oxidized.

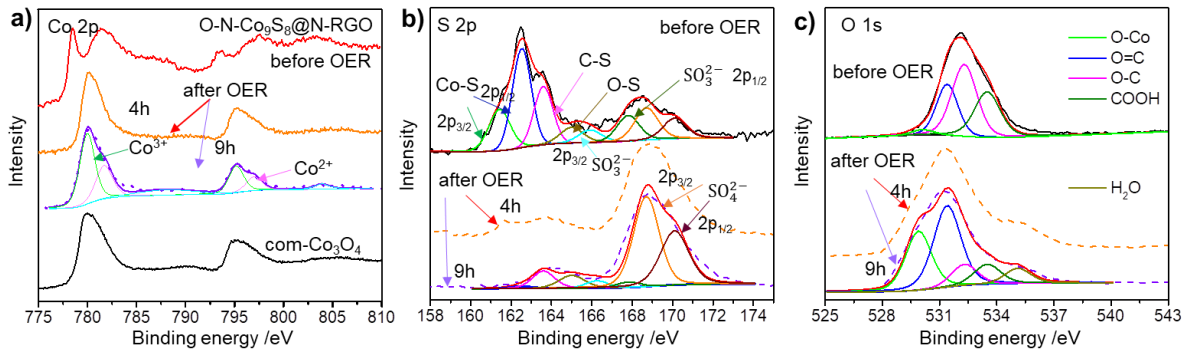

Figure 4.3 a) XPS spectra of the Co 2p; b) S 2p; c) O 1s in O-N-Co_9S_8@N-RGO before and after OER reaction.

The activity of O-N-Co_9S_8@N-RGO was measured by LSV voltammetry with 0.1 M KOH solution. The results show that it delivers an ORR onset potential of 0.91 V, and a half-wave potential of 0.81 V (Figure 4.4a). Although the ORR performance of the as-prepared composite still cannot provide the same performance as that obtained with the Pt/C catalyst, it exhibits a much lower OER over-potential (~350 mV) than commercial Ir/C (20%Ir supported on Vulcan XC-72, ~392 mV) when a current density of 10 mA cm^{-2} is generated (Figure 4.4b). This indicates that this composite is one of the best performing OER catalysts in mild alkaline media (see Table 4.1).

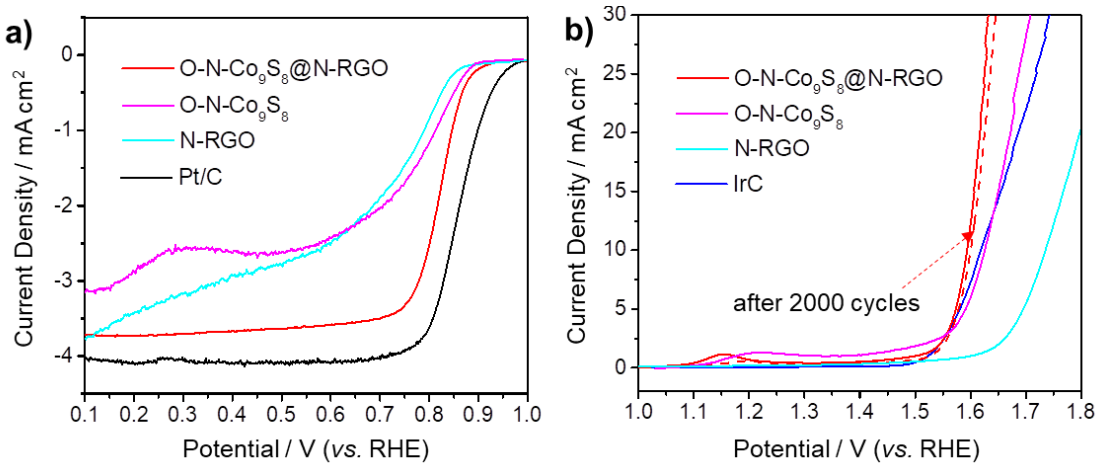

Figure 4.4 a) ORR activities evaluated by RDE LSV at a rotating speed of 900 rpm; b) OER activity at RDE (1600 rpm) in 0.1 M KOH electrolyte. LSVs adopted at a scan rate of 10 mV s^{-1}.

Table 4.1. Comparison of the OER performance (in 0.1M KOH) of O-N-Co_9S_8@N-RGO catalyst with other highly OER active metal sulfides or oxides catalysts reported in the literature.

Bifunctional catalysts	OER over-potential at 10mA cm^{-2}
O-N-Co_9S_8@N-RGO	350mV (This work)
N-Co_9S_8/G	409mV[7]
$CoO_{0.87}S_{0.13}$/GN	357mV[14]
$Co_{0.5}Fe_{0.5}S$@N-MC	340mV[28]
Co_xO_y/NC	430mV[29]
CoO_x/CNT	390mV[30]
Co_3O_4 thin film	377 mV[31]
Co_3O_4/N-C	450 mV[32]
Co@Co_3O_4	410 mV[33]

In addition to the O-N-Co_9S_8@N-RGO, O-N-Co_9S_8 and N-RGO were synthesized to distinguish the active ORR and OER component in the composite (Figure 4.4). The synthesis procedures are presented in Section 4.2.2. The results show that: *i)* O-N-Co_9S_8 and N-RGO alone only have limited ORR activity, highlighting the importance of combining Co and N-RGO in improving ORR performance; *ii)* although the N-RGO can further enhance the OER activity, the OER activity of the O-N-Co_9S_8@N-RGO is mainly contributed by O-N-Co_9S_8 phase. Figure 4.4b shows that the activity of the O-N-Co_9S_8@N-RGO was maintained after 2000 cyclic voltammetry cycles (from 0.9 to 1.7 V *vs*. RHE).

It is also worth to mention that the O-N-Co_9S_8@N-RGO catalyst was obtained by thermal-shock treatment of Co-S-O-N-RGO precursor under NH_3 atmosphere at 700 ℃. However, when the

Co-S-O-N-RGO precursor was treated at a higher temperature 900 ℃, it was converted into a highly-oxidized, S-doped $Co_{5.47}N$ and N-RGO composite (Figure 4.5 and Figure 4.6a), referred to as O-S-$Co_{5.47}N$@N-RGO. On the other hand, when the thermal treatment was conducted under Ar instead of NH_3 at T=700 ℃, the resulting product is S-doped CoO and N-RGO composite (S-CoO@N-RGO), (Figure 4.5 and Figure 4.6a). The formation of CoO can be expected since both the Co precursor and GO contains a large amount of O. Both of the composites have a similar morphology as in O-N-Co_9S_8@N-RGO. The HRTEM image of O-S-$Co_{5.47}N$@N-RGO composite was presented in Figure 4.5b. The lattice fringe was identified as (111) plane with an interspace of 0.21 nm.[34] However, it shows many dislocations and stacking faults, which might result from the highly oxidation of the $Co_{5.47}N$ surface. For the S-CoO@N-RGO composite, its HRTEM image shows a clear lattice fringe with the d-spacing value of 0.24 nm, corresponding to (111) crystal planes of cubic CoO [35] (Figure 4.6d).

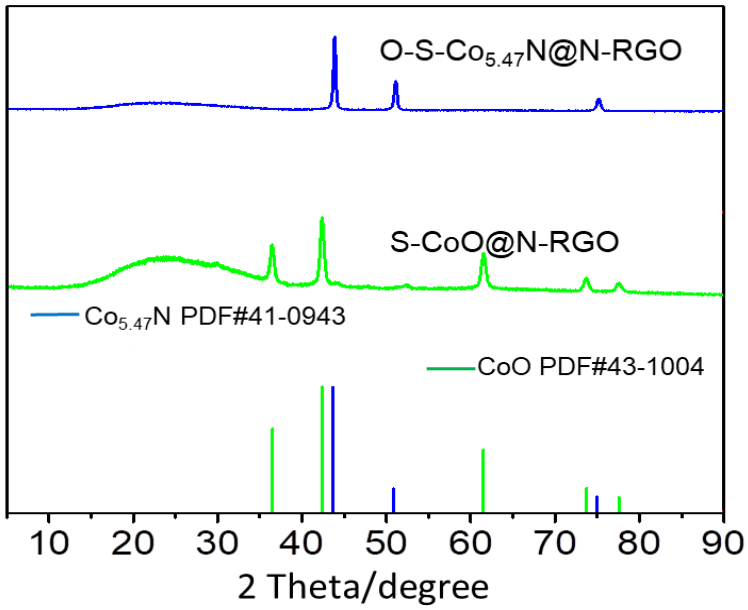

Figure 4.5 XRD patterns of the O-S-$Co_{5.47}N$@N-RGO and S-CoO@ N-RGO composite.

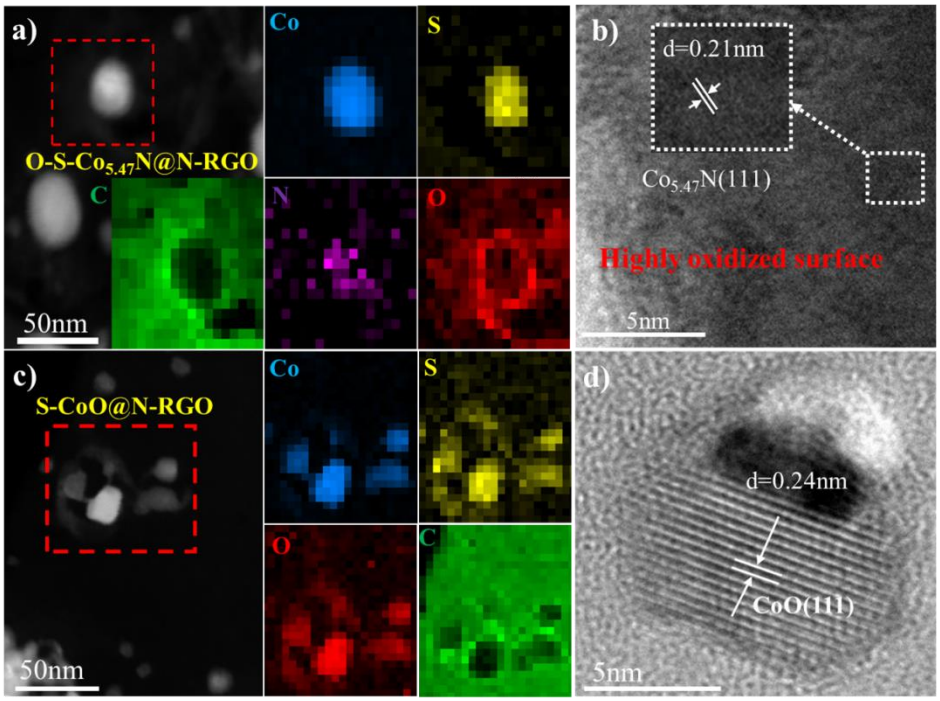

Figure 4.6 a) The TEM-Electron energy-loss spectroscopy (TEM-EELS) mapping and b) HRTEM images for the O-S-$Co_{5.47}N$@N-RGO; c) TEM-EELS mapping and d) HRTEM images of the S-CoO@N-RGO composite.

The ORR/OER activity of the O-S-$Co_{5.47}N$@N-RGO and S-CoO@N-RGO composites were also measured and compared with that of O-N-Co_9S_8@N-RGO. Figure 4.7a shows that the O-S-$Co_{5.47}N$@N-RGO exhibits a similar onset and half-wave potential as O-N-Co_9S_8@N-RGO, and sightly higher than S-CoO@N-RGO. Also, the OER activity of S-CoO@N-RGO is much lower than that of O-S-$Co_{5.47}N$@N-RGO and O-N-Co_9S_8@N-RGO (Figure 4.7b). Therefore, in this work, we focus on the study of the catalytic performance of the as-obtained O-N-Co_9S_8@N-RGO composite.

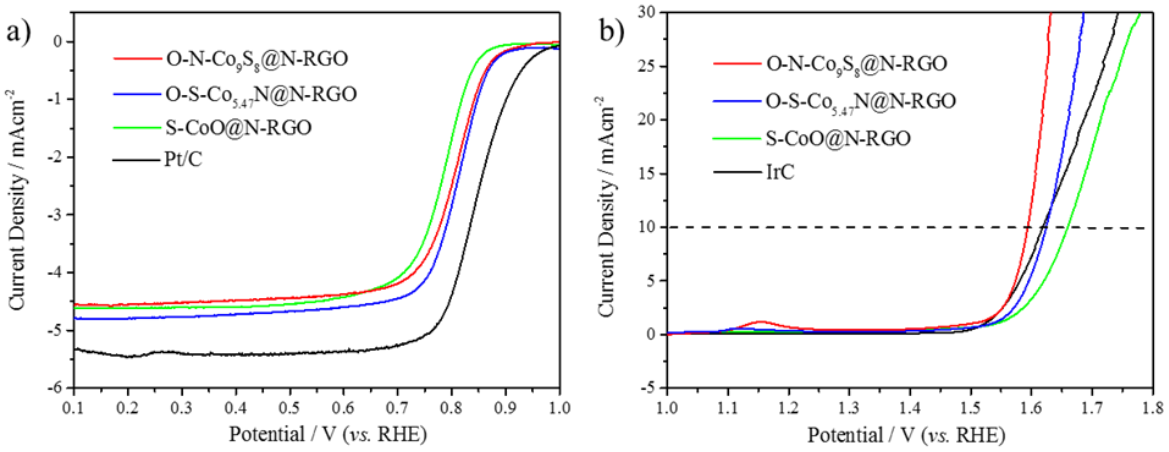

Figure 4.7 Comparison of electrocatalytic performance of O-N-Co_9S_8@N-RGO, O-S-$Co_{5.47}N$@N-RGO and S-CoO@ N-RGO composites evaluated in 0.1 M KOH: a) ORR and b) OER LSV curves obtained at a scan rate of 10 mV s^{-1} under rotating speed of 1600rpm.

Hence, the stability performance of O-N-Co_9S_8@N-RGO was first evaluated through the current-time curve with the applied potentials at 1.60V *vs.* RHE (Figure 4.8a). The result shows that the O-N-Co_9S_8@N-RGO electrodes deliver a stable current over 20 hours of continuous operation, implying its good "stability" for OER. When used as an air electrode (catalyst loading of 0.67 mg cm^{-2}) in zinc-air battery, O-N-Co_9S_8@N-RGO demonstrates comparable and even better charge performance with that of Pt/C+Ir/C particularly at high current densities (Figure 4.8b). In addition, a long-term cyclability for over 200 h (at 10 mA cm^{-2}) was achieved in ambient air (Figure 4.8c), indicating that the O-N-Co_9S_8@N-RGO composite exhibits excellent cycling performance for OER.

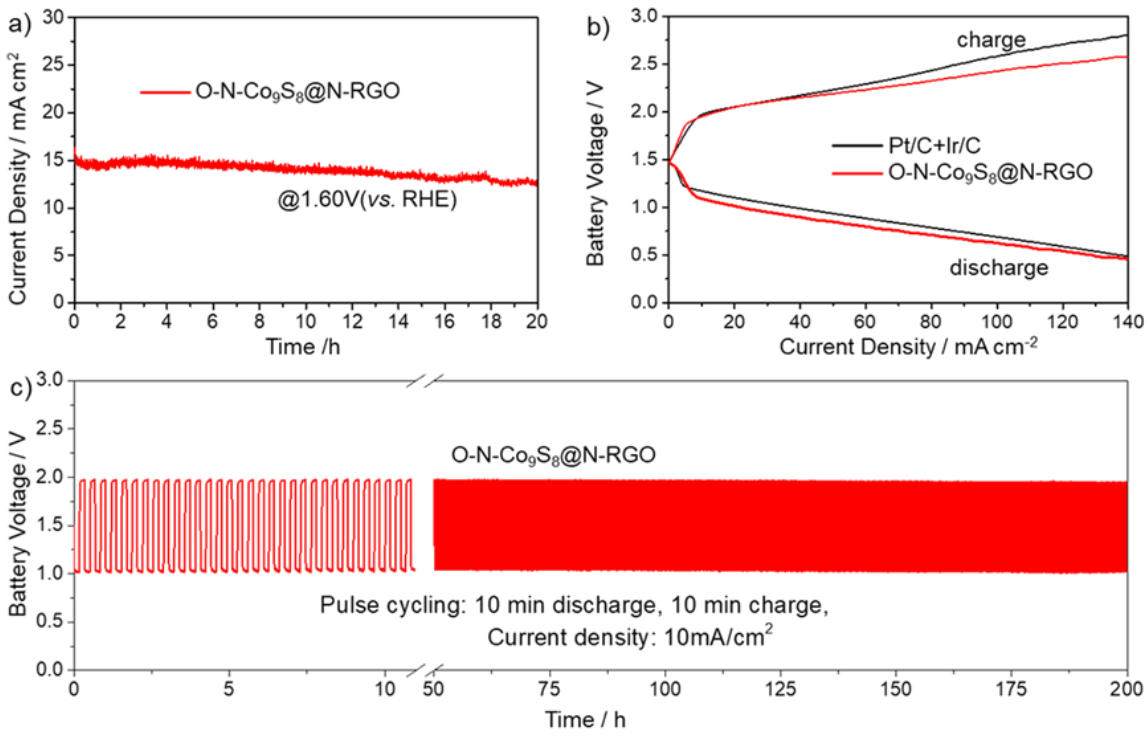

Figure 4.8 a) Long-term OER electrolysis stability of O-N-Co_9S_8@N-RGO under constant potential; b) Charge and discharge polarization curves, and c) Cycling performance of Zinc-air battery assembled using O-N-Co_9S_8@N-RGO as air electrode in ambient air.

The morphology and composition of the O-N-Co_9S_8@N-RGO catalyst after OER half-cell test (at a constant potential of 1.60V *vs*.RHE) were also examined. The XRD pattern (Figure 4.2) and TEM images (Figure 4.9a-b) showed that, after 9 hours of OER reaction, O-N-Co_9S_8 crystals were converted to aggregated Co_3O_4 particles. This suggests that there is a phase transformation during OER, which might also be facilitated by the doped and imperfect crystallization nature of O-N-Co_9S_8. HRTEM imaging (Figure 4.9c) show that the interplanar spacings on Co_3O_4 are 0.16, 0.20 and 0.24 nm, respectively, which corresponds to the d-spacing (422), (400) and (311) lattice planes of cubic Co_3O_4. This is consistent with that shown in the FFT pattern (inset Figure 4.9c). TEM-ELLS mapping of the sample after OER reveals that most of S was replaced by O, whereas N was no longer observed in the mapping analysis (Figure 4.9d). This observation suggests that

N (or at least most of N) was removed after OER, which is also supported by the N1s XPS analysis (Figure 4.10).

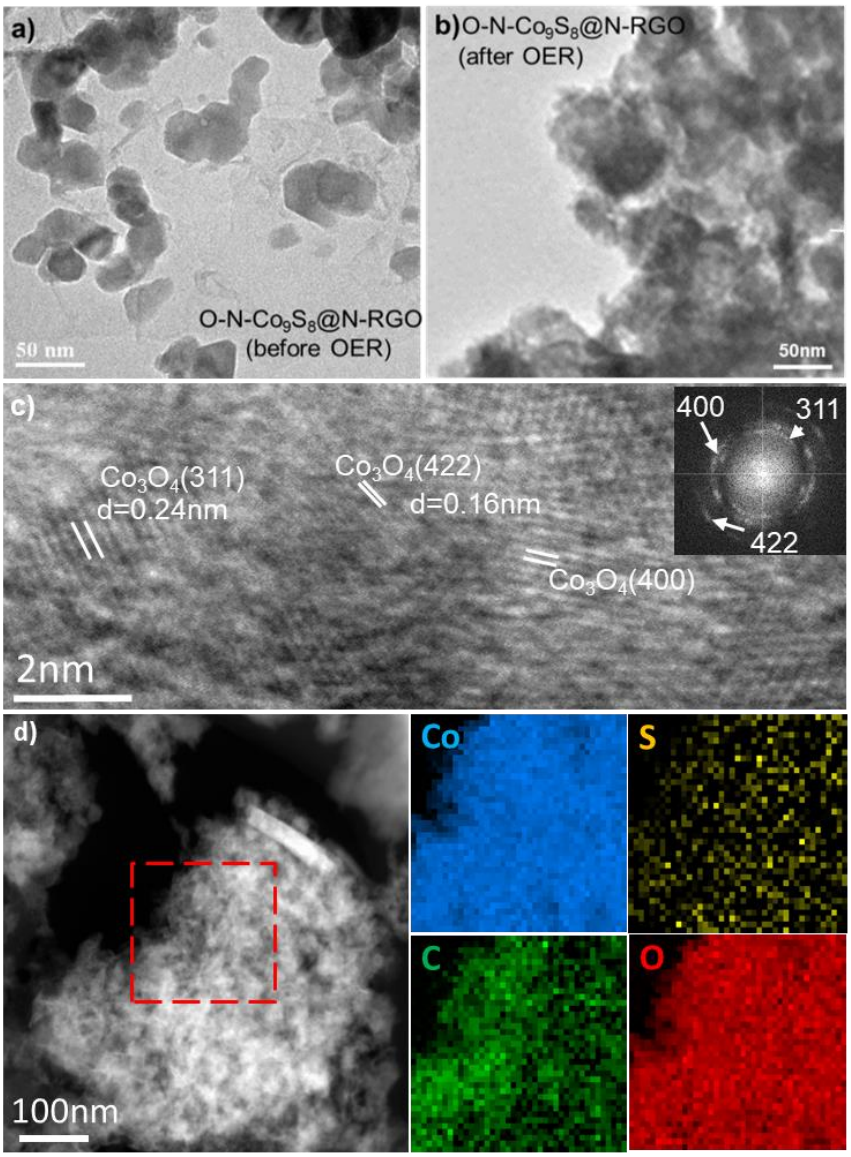

Figure 4.9 a) TEM image of O-N-Co_9S_8@N-RGO before and b) after 9h OER half-cell test at a constant potential of 1.60V *vs.* RHE; c) HRTEM and b) TEM-EELS mapping images of O-N-Co_9S_8@N-RGO after OER reaction.

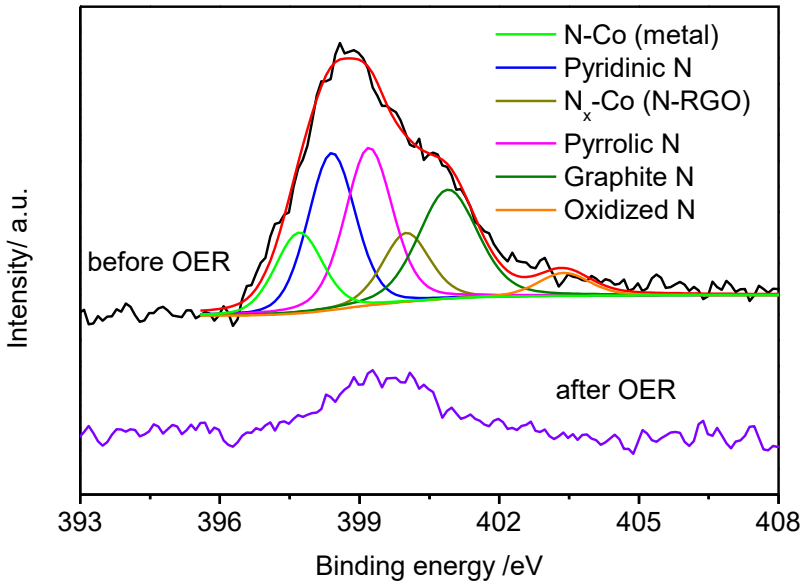

Figure 4.10 XPS spectra of N 1s in O-N-Co_9S_8@N-RGO composite before and after 9 hour OER reaction.

The Co 2p XPS spectrum of the post-OER (after 4 and 9 hour reaction) O-N-Co_9S_8@N-RGO catalyst are identical to that obtained from com-Co_3O_4. By integrating the peak area of Co^{3+} and Co^{2+}, the Co^{3+}/Co^{2+} ratio was found to be 1.93:1, which is very close with the theoretical value of Co^{3+}/Co^{2+} = 2:1 in Co_3O_4, which further supports the transformation of O-N-Co_9S_8 to Co_3O_4. The very minor Co-S peak after OER reaction, as shown in S 2p XPS spectrum (Figure 4.3b), also confirms the replacement of S by O in O-N-Co_9S_8 particle. The increased intensity of SO_4^{2-} peaks imply that most of the residue S exists in the form of SO_4^{2-}. The substitution of S by O is also supported by the increased intensity of O-Co peak in O 1s XPS spectrum (Figure 4.3c, after OER).

The above analysis confirmed the complete oxidation of O-N-Co_9S_8 into Co_3O_4 during OER. As shown in previous half-cell and zinc-air durability test (Figure 4.8a, and 4.8c), even after 9 hours, the catalyst still exhibits excellent OER performance, e.g. in half-cell RDE durability test,

the output current dropped by 15% after 20 hours. That is, the high OER activity was maintained during, and even after the transformation of O-N-Co_9S_8 to Co_3O_4. This raises another question: how is this achieved? Interestingly, we found that the (111) lattice plane of Co_3O_4, featured with large interplanar spacing (0.46nm), was not detected in the present HRTEM imaging analysis. It is one of the typical surfaces that is commonly observed in calcined Co_3O_4 (Figure 4.11).

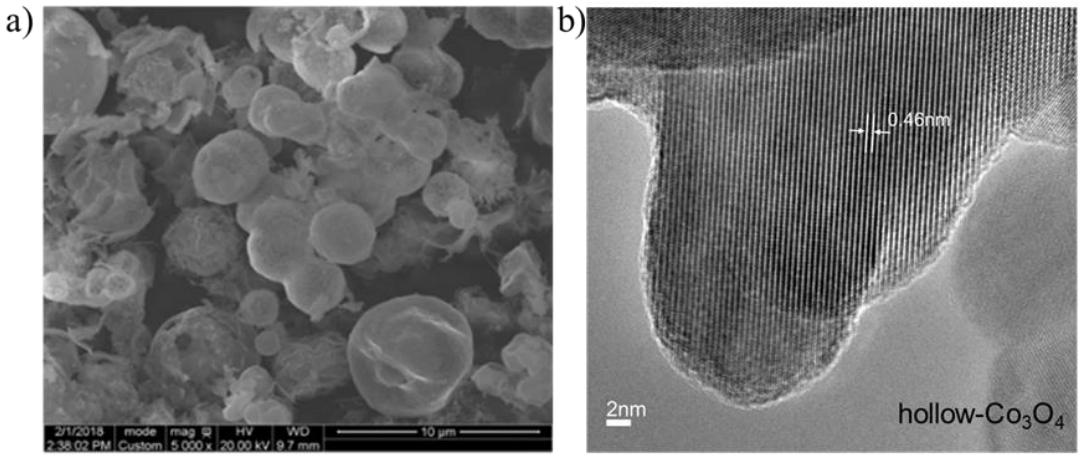

Figure 4.11 a) SEM and b) HRTEM image of calcined hollow Co_3O_4 particle.

Therefore, based on the above observations, it is reasonable to assume that the Co sites in the resulting Co_3O_4 (311), (422), (400) high-index surfaces might be responsible for the high OER activity of the post-OER (or *in-situ* generated) Co_3O_4 phase. This is consistent with the experimental study by Wei et al.[36], in which they reported that the exposed Co_3O_4 (112) high-index facet shows much lower overpotential for OER than (111) surface. This might explain the higher OER activity of this *in-situ* generated Co_3O_4 than many reported calcined Co_3O_4 catalysts (Table 4.1). The latter usually contains exposed Co_3O_4 (111) plane (Figure 4.11). This means that, although Co_3O_4 has been confirmed as the real stable OER catalytic phase, the direct synthesis of Co_3O_4 by calcination might not be a suitable approach for preparing efficient OER

catalyst. The Co_3O_4 obtained from phase transition under OER might be more active than calcined Co_3O_4 crystals.

To further support this argument, we reduced the com-Co_3O_4 in H_2 (10%)/Ar atmosphere at 700℃ for 5 mins. The XRD and XPS Co 2p spectrum show the resulting product is a composite of Co-CoO crystals, and the surface Co is in the state of CoO (Figure 4.12a). As expected, in the RDE test, it exhibits a ~50 mV lower overpotential (at 10 mA cm^{-2}) for OER than com-Co_3O_4 (Figure 4.12b). As shown in Figure 4.12c, the Co-CoO composite delivers a stable OER performance under continuous operation at an applied potential of 1.65V *vs*. RHE. Post-OER characterizations show that, after the 9 hour OER test at 1.65V *vs*. RHE, the Co-CoO crystals remained intact (Figure 4.12a). However, the state of surface Co was transformed from CoO into Co_3O_4 (Figure 4.12d).

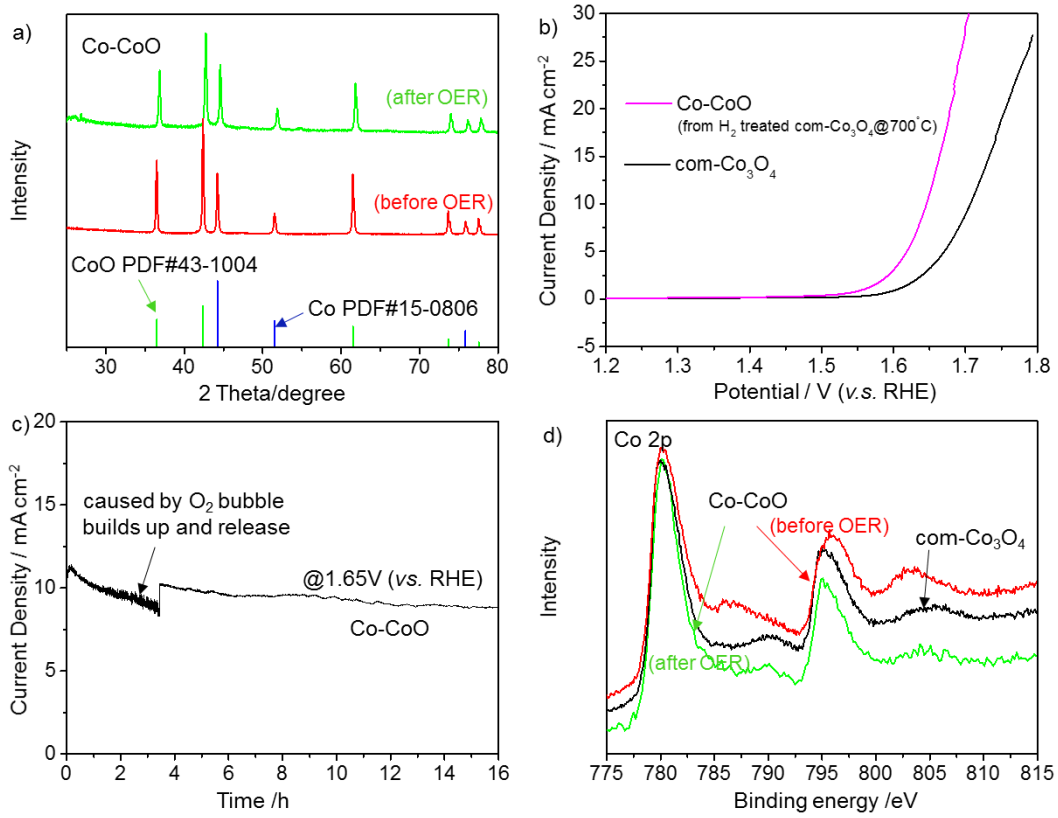

Figure 4.12 a) XRD and b) OER activities of Co-CoO (obtained from H_2 treatment of com-Co_3O_4) at RDE (1600 rpm) in 0.1 M KOH electrolyte at LSV scan rate of 10 mV s^{-1}; c) Long-term electrolysis stability of Co-CoO composite under constant potential in RDE test; d) Co 2p XPS spectra of the Co-CoO composite before and after 9hour OER test at constant potential of 1.65 V (*vs.* RHE).

Similar results were also obtained for our calcined hollow Co_3O_4 catalyst: when reduced by H_2, the resulting hollow CoO-Co_3O_4 composite shows a ~35 mV lower OER overpotential than the original hollow Co_3O_4 particle (Figure 4.13). Here, it is worth mentioning that there are studies report the formation of $Co(OH)_2$ and CoOOH species during OER on CoO_x catalysts in XPS and in-situ surface-enhanced Raman spectroscopy analysis. [37-39] In fact, the formation of OH-Co-OH and OH-Co-O intermediate surfaces is very likely to occur during OER, especially on the out-most Co_9S_8/Co_3O_4 surfaces that are in close contact with the OH^- reactant. Bulk-Pourbaix thermodynamics have dictated that, as the potential increases, the stability of Co states increases as $Co(OH)_2$ < Co_3O_4 < CoOOH < CoO_2, and Co^{2+} is predicted unstable at the OER region (above 1.23 V vs RHE).[40, 41] Interestingly, in the present study, there is no evidence for the formation of $Co(OH)_2$ and CoOOH species even in the XPS analysis. One possible explanation might be they were oxidized into Co_3O_4 states (CoO/Co_2O_3) in ambient air. Or, the formation of CoOOH (Co^{3+}) and CoO_2 (Co^{4+}) crystal is kinetically unfavoured at 1.65V vs RHE, because of the less oxidative S in the composite. These S could stabilize the low oxidation state Co^{2+}. Meanwhile, the replacement of S and with O would consume many OH^-, lowering the local concentration of OH^- on the catalyst surface. As a result, the oxidation kinetics for Co^{2+} to Co^{3+} or Co^{4+} might be hindered. Moreover, considering the fact that: *i)* the formation of $Co(OH)_2$ and CoOOH bulk crystals has been rarely reported; *ii)* in the present study, Co_3O_4 crystal was indeed produced during OER. This indicates that Co_3O_4 is the real stable phase formed in OER when

Co_9S_8 is used as the “catalyst”.

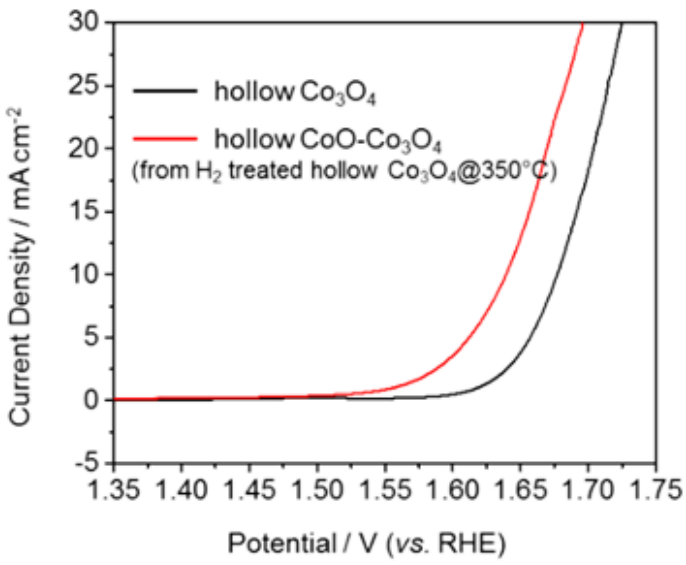

Figure 4.13 a) OER activities of hollow CoO-Co_3O_4 (obtained from H_2 treatment of hollow Co_3O_4) and hollow Co_3O_4 at RDE (1600 rpm) in 0.1 M KOH electrolyte at LSV scan rate of 10 mV s^{-1}.

4.4 Summary

An O-N-Co_9S_8@N-RGO composite was designed as an efficient and stable bifuntional catalyst for Zinc-air batteries. It was developed on the basis of imperfect crystallization and surface engineering, e.g. oxidation and nitrogen doping, of Co_9S_8 crystals to achieve a high catalytic activity in particularly for OER. When used as the air electrode catalyst, the Zinc-air battery exhibits significantly reduced discharge and charge overpotentials and outstanding long cycling stability over 200 cycles at 10 mA cm^{-2}. Moreover, post-characterization reveals that O-N-Co_9S_8 was completely converted into Co_3O_4 after OER, confirming Co_3O_4 is the real stable catalytic phase. As there are increasingly many reports claiming transition metal sulfides as highly efficient OER catalysts, this observation further clarifies what the OER catalyst really is.

Moreover, the study suggested that the continuous exposure of these oxidized Co sites during O-N-Co_9S_8 transition into Co_3O_4 might play an essential role in the cycling performance of such catalyst. This is made possible by *i)* the surface reconstruction during O-N-Co_9S_8 transition into Co_3O_4, and *ii)* the unique Co sites topology on the exposed planes of *in-situ* generated Co_3O_4. With such knowledge, our study suggests, and experimentally shows that *in-situ* generated metal oxides, e.g. Co_3O_4, from phase transition of metal chalcogenides, or reduced metal oxides during OER, should be more active than the calcined oxides crystals. This work advances the fundamental insights on the activity and "stability" of metal chalcogenides-based OER "catalysts", providing guidance for the design of active OER catalysts.

CHAPTER 5

Three Dimensional Self-supported Cobalt Sulfide Bi-functional Electrocatalyst

The ORR and OER reaction in zinc-air batteries occur at the gas/catalyst/electrolyte three-phase interfaces. Thus, design of non-precious ORR-OER bi-functional catalysts that are active, stable and easily accessible to atmospheric O_2 in alkaline electrolyte are essential. Therefore, in this study, the N-RGO supported surface engineered Co_9S_8 hybrid catalyst reported in Chapter 4 was designed into a self-supported three-dimensionally ordered macroporous (3DOM) bi-functional catalyst, which is composed of honeycomb-structured N-Co_9S_8 embedded with an N-doped carbonaceous (NC) layer, referred to as 3DOM N-Co_9S_8@NC. Benefiting from the hierarchical 3DOM structure design and the ORR-OER active NC and N-Co_9S_8 components, the 3DOM N-Co_9S_8@NC catalyst exhibits a comparable ORR and much better OER performance with that Pt/Ir-based noble catalyst. The zinc-air battery with 3DOM N-Co_9S_8@NC catalyst demonstrated outstanding galvanodynamically charge and discharge performance and achieved long cycling stability over 400 h at 10 mA cm^{-2}.

5.1 Introduction

In the previous chapter, we have demonstrated a rational design of efficient two-dimensional N-RGO supported Co_9S_8 bi-functional catalyst through an effective surface engineering technique. Despite the activity improvement, the actual performance of the carbon-supported Co_9S_8 air electrode might be restricted by the slow mass transfer process within 2D featured N-RGO-based catalyst. Since the reactions occur at the O_2 gas/catalyst/electrolyte three-phase interface, catalysts with porous structure could facilitate the mass transfer process, e.g. O_2 gas

diffusion, within the catalyst, and further improve the electrochemical performances of the batteries.[1-3] Moreover, N-RGO would suffer from electrochemical oxidation (or corrosion) under the high operating potentials of OER and thus degrade the durability performance of the catalyst.[4,5]

Therefore, in this work, we proposed that, by designing surface engineered Co_9S_8 into a self-supported porous framework with a three-dimensional through-continuity, it can increase the accessibility of the active phases to reactants while minimizing agglomeration of nanoparticles for better durability. The 3D nanoarchitectures with periodically and continuous porous networks are expected to offer improved bi-functional oxygen catalysis for rechargeable zinc-air batteries. To this end, a hybrid catalytic nanoarchitecture is constructed in which active phases of both Co_9S_8 and N-doped carbon and pores are connected within an electronically conductive 3D network. Such architecturally arranged catalyst with increased surface area and site activity with high absorptivity and mass transport potential, giving rise to favourable catalytic activity for both ORR and OER.

5.2 Experimental section

5.2.1 Preparation of 3DOM Co_9S_8 composites

Figure 5.1a) shows the procedure for preparing the three-dimensionally ordered hierarchical porous Co_9S_8 composites (3DOM Co_9S_8). First, polystyrene spheres (PS) with an average diameter of ~200 nm (Figure 5.1 b and c) were synthesized through emulsion polymerization reaction using styrene, polyvinylpyrrolidone (PVP), potassium persulfate and DDI water. Then, the as-obtained of monodisperse PS spheres were self-assembled into ordered, close-packed PS template through centrifugation.[6] After that, a cobalt-sulfur precursor was prepared by

dissolving 2.0 g Cobalt(II) sulfate heptahydrate ($CoSO_4 \cdot 7\ H_2O$) into a 10.5 mL solution that mixed from methanol (MeOH) and hydrochloric acid (HCl) [MeOH: HCl volumetric ratio=20:1] at room temperature. Then, 2.0 g PS template was added to the as-prepared cobalt-sulfur precursor solution and followed by a 10 min vacuum impregnation. The infiltrated PS template (Precursor@PS) was filtered and dried overnight at ambient condition. The 3DOM Co_9S_8 composites were fabricated by calcinating the Precursor@PS in Ar and NH_3 atmosphere at 500°C with a ramp 1°C/min. The composition of the as-prepared 3DOM Co_9S_8 materials can be tuned by changing the duration of NH_3 treatment. The resulting powder product etching in NH_3 for 20min was referred to as 3DOM N-Co_9S_8@NC. For optimization purpose, the Precursor@PS nanocomposite treated in NH_3 atmosphere for 40 min and Ar (without NH_3 etching) were also performed, the resulting composites were referred to as 3DOM $Co_9S_8/Co_2N_{0.67}$@NC and 3DOM Co_9S_8/CoO@C, respectively.

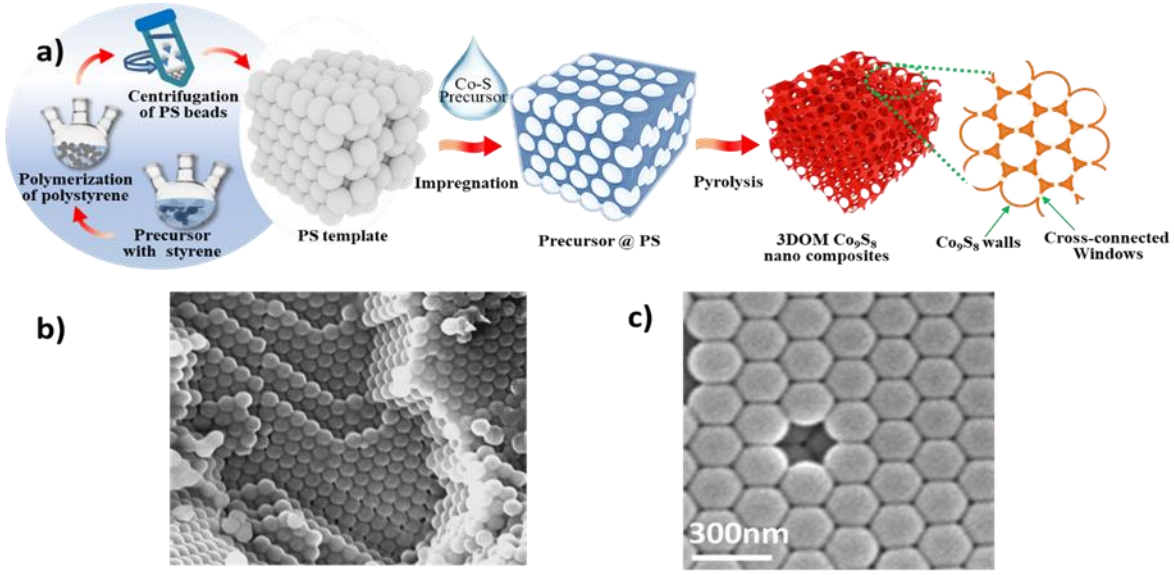

Figure 5.1 a) Schematic diagram of the procedure for the preparation of 3DOM Co_9S_8 composites; b) low and c) high magnification SEM images of PS template.

5.2.2 Material characterization

The morphologies and microstructures of the as-prepared 3DOM catalysts were characterized using scanning electron microscopy (SEM, LEO FESEM 1530), transmission electron microscopy (TEM, JEOL 2010F) and scanning transmission electron microscopy (STEM) -electron energy loss spectroscopy (EELS) mapping. Their crystal structures were investigated using X-Ray Diffraction (XRD, Rigaku Miniflex 600), High-resolution TEM (HR-TEM, Titan 80-300 HB). The surface chemical composition of the samples was analyzed by X-ray photoelectron spectroscopy (XPS, Thermo Scientific Al K-Alpha Xray source), binding energy scale was calibrated to fix the carbon sp3 peak at 284.8 eV. BET analysis was performed to evaluate the surface area of 3DOM N-Co_9S_8@NC composite.

5.2.3 Electrochemical evaluation

The electrocatalytic activities of the as-prepared 3DOM Co_9S_8 composites were evaluated using a three-electrode glass cell in 0.1 M KOH solution. An SCE electrode and graphite rod was used as the reference and counter electrodes, respectively. The working electrode is the glassy carbon electrode loaded with 3DOM catalyst. The catalyst inks were prepared by dispersing 2 mg of active 3DOM Co_9S_8 composite and 2 mg of Vulcan XC-72 in 1 mL of ethanol containing 0.15 wt% Nafion ionomer. The ink was sonicated for 30min. Then, 25 µL of catalyst ink was drop-casted onto the RDE electrode. The loading of active 3DOM Co_9S_8 catalysts is 0.25 mg cm^{-2}. The ORR and OER activities of the 3DOM catalysts were measured under O_2 and N_2 saturated 0.1M KOH, respectively, at a scanning rate of 10 mV s^{-1}. The same procedure was applied to measure the ORR and OER activity of commercial precious catalysts Pt/C (28.8 wt. % Pt) and

Ir/C (20 wt. % Ir), respectively. Calibration of SCE was performed by measuring the voltage ΔE between the SCE and a Pt wire immersed in the high purity hydrogen saturated 0.1 M KOH electrolyte. The measured ΔE between SCE and RHE is 0.996V. Then RDE potentials are calibrated and given as referred to RHE using the equation 5-1:

$$V_{RHE}=V_{SCE}+0.996\ V \qquad (5-1)$$

The kinetics of the as-developed 3DOM N-Co_9S_8@NC catalyst has been investigated through a series of LSV tests conducted at a rate of 10mV s^{-1} with varying rotating speed from 400 rpm to 2500 rpm. Specifically, the number of electrons transferred for ORR on 3DOM N-Co_9S_8@NC electrodes was determined on the basis of the Koutechy-Levich (K-L) equation as given blow [7,8]:

$$\frac{1}{J}=\frac{1}{J_L}+\frac{1}{J_K}=\frac{1}{B\omega^{1/2}}+\frac{1}{J_K} \qquad (5-2)$$

$$B=0.62nFC_o(D_o)^{2/3}v^{-\frac{1}{6}} \qquad (5-3)$$

where J is the measured current density, J_L is the diffusion-limiting current density, J_K is the kinetic current density, ω is the electrode rotation rate (rad s^{-1}), n is transferred electron number, F is Faraday constant (96485 C mol^{-1}), C_o is the bulk concentration of O_2, D_0 is the diffusion coefficient of O_2 and υ is the kinetic viscosity of the electrolyte. For the case of 0.1 M KOH at room temperature, the constants adopted are as follows: C_o=1.2×10^{-3} mol L^{-1}, D_0=1.9×10^{-5} cm^2 s^{-1}, υ=0.01 cm^2 s^{-1}.

The electrochemical performance of the catalyst 3DOM N-Co_9S_8@NC in zinc-air battery was tested using a multichannel potentiostation (Princeton Applied Research, VersaSTAT MC).

The catalyst was spray-coated onto carbon paper and was used as cathode. The catalyst loading is 1.0 mg cm^{-2}. The anode and separator are zinc-plate and microporous membrane, respectively. The electrolyte is 6.0M KOH solution with 0.2M $Zn(CH_3COO)_2$. The galvanodynamic charge and discharge profiles of the battery were obtained by scaling the current density from 0 to 150 mA cm^{-2}. The cycling tests were conducted at a current density of 10 mA cm^{-2} with 10 min discharge and 10min charge time for each cycle. The tests were operated in ambient air condition.

5.3 Results and discussion

The crystal structure of the as-prepared 3DOM Co_9S_8 composites was confirmed by XRD analysis. Figure 5.2 shows that the diffraction peaks of Co_9S_8 (JCPDS:65-1765) were observed for the 3DOM N-Co_9S_8@NC. The typical graphitic carbon peak was not detected, indicating the presence of amorphous carbon in the composite. For the 3DOM Co_9S_8/$Co_2N_{0.67}$@NC composite obtained in 40min NH_3 treatment, in addition to Co_9S_8, diffraction peaks of $Co_2N_{0.67}$ (JCPDS:06-0691) were found. The existence of CoO (JCPDS:43-1004) in 3DOM Co_9S_8/CoO@C obtained in Ar atmosphere was also verified. Interestingly, the Co_9S_8 peaks in 3DOM N-Co_9S_8@NC and 3DOM Co_9S_8/$Co_2N_{0.67}$@NC were found shift to higher angles, suggesting N-doping in the Co_9S_8 crystal lattice.

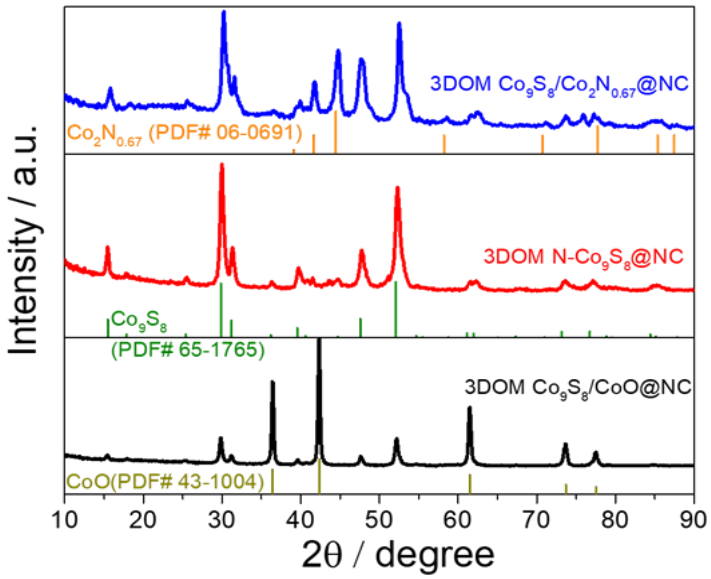

Figure 5.2 XRD patterns of various 3DOM Co_9S_8 composites.

The structure and morphology of these 3DOM composites were characterized using SEM and TEM. Figures 5.3a-c) presents the SEM images of the three composites, clearly showing their 3DOM architecture. It can be seen that the macropores with the size of about 200 nm are interconnected by windows on the wall. TEM images show that, as compared with that of 3DOM Co_9S_8/CoO@C (Figures 5.3d) and $Co_9S_8/Co_2N_{0.67}$@NC (Figure 5.3f), the 3DOM N-Co_9S_8@NC catalyst possesses more uniform and continues wall with a thickness of ~20nm (Figure 5.3e). The N_2 adsorption-desorption isotherms confirm the presence of mesoporous and macroporous structure in the 3DOM N-Co_9S_8@NC with a high BET surface area of 95.75 m^2 g^{-1} (Figure 5.3g). This ensures high availability of the catalytic active sites, and therefore is beneficial for the ORR and OER.

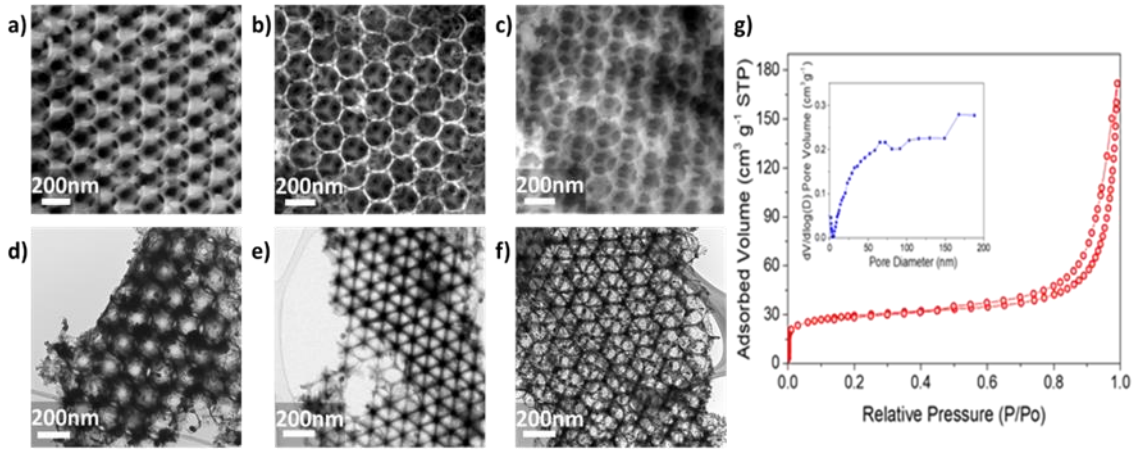

Figure 5.3 a-c) SEM images; and d-f) TEM images of 3DOM Co_9S_8/CoO@C, 3DOM N-Co_9S_8@NC and 3DOM Co_9S_8/$Co_2N_{0.67}$@NC composites, respectively; g) N_2 adsorption-desorption isotherms and pore size distribution of 3DOM N-Co_9S_8@NC composite.

Figure 5.4a-c show the STEM-EELS elemental mapping of the selected wall region of the 3DOM Co_9S_8 composites. In 3DOM N-Co_9S_8@NC, the intense Co and S signals and uniformly distributed N throughout its wall structure indicate that the successful N-doping of Co_9S_8 framework **(**Figure 5.4b**)**. Figure 5.4a and c show that the O and N elements distributed throughout the wall structure in the Co_9S_8/CoO@C and Co_9S_8/$Co_2N_{0.67}$@NC composite, respectively. However, S is only observed on part of 3DOM walls and its linkage particles. A reasonable explanation for this observation is that the framework of Co_9S_8/CoO@C is CoO decorated with Co_9S_8, whereas the wall of Co_9S_8/$Co_2N_{0.67}$@NC is $Co_2N_{0.67}$ combines with N-doped Co_9S_8. The C signals in the external edge of Co_9S_8 wall manifest that the carbon is originated from PS during calcination in Ar.

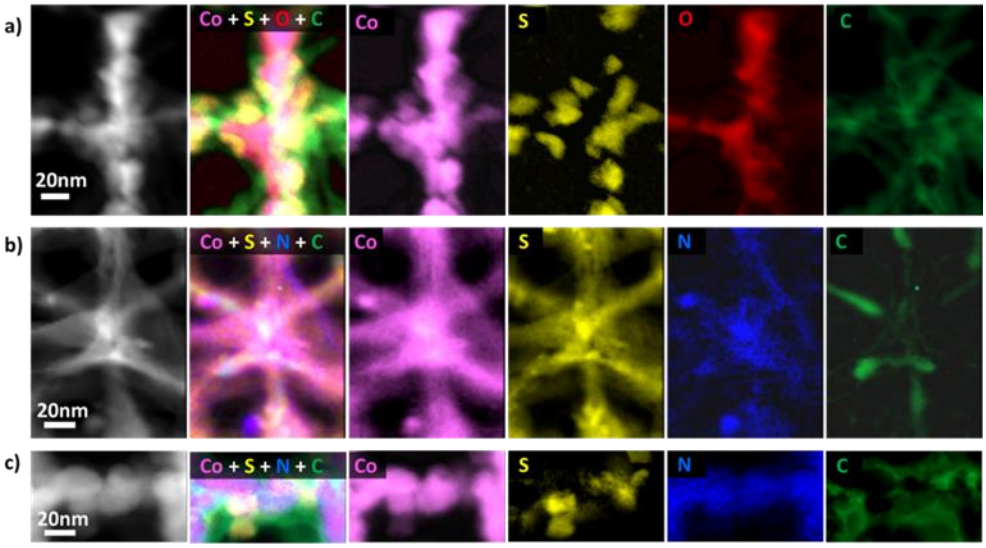

Figures 5.4 STEM-electron energy-loss spectroscopy (STEM-EELS) elemental mapping of a) 3DOM Co_9S_8/CoO@C; b) 3DOM N-Co_9S_8@NC; and c) 3DOM Co_9S_8/$Co_2N_{0.67}$@NC composites.

The high-resolution TEM (HRTEM) image of the 3DOM N-Co_9S_8@NC framework reveals that its Co_9S_8 wall is intimately lining with an amorphous carbon layer (Figure 5.5), enabling a good conductivity of the catalyst. Three different lattice fringes were observed and their corresponding fast Fourier transform (FFT) patterns can be indexed to the (311), (220) and (200) crystal planes of Co_9S_8, respectively, which align well with the XRD result (Figure 5.2).

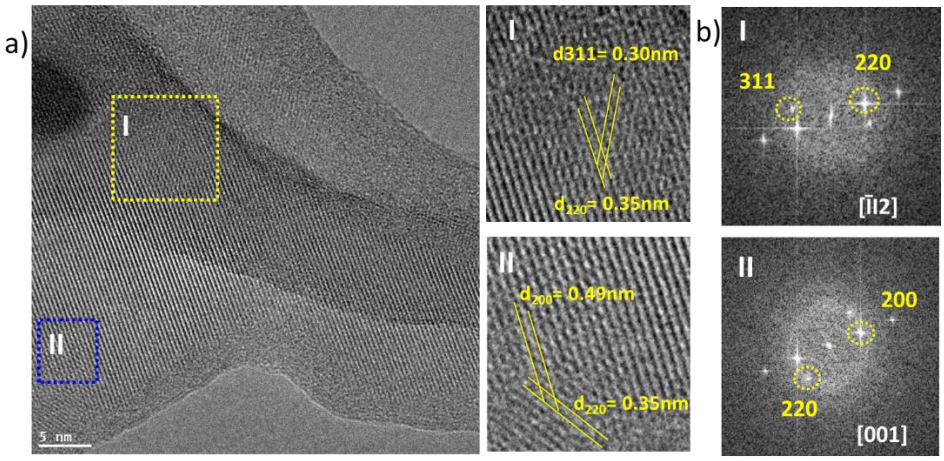

Figure 5.5 a) HRTEM image and b) corresponding FFT pattern of 3DOM N-Co_9S_8@NC composite.

Furthermore, the chemical states of the fabricated 3DOM Co_9S_8 composites were probed with XPS. As shown in Figure 5.6a, the chemical state of Co in the 3DOM N-Co_9S_8@NC and 3DOM Co_9S_8/CoO@C composites is similar, in which the peaks of Co $2p_{3/2}$ and Co $2p_{1/2}$ are deconvoluted into three components. The two peaks located at 780.5 and 782.3 eV are assigned to binding energies of Co^{3+} and Co^{2+}, respectively. Peaks at 786.6 and 802.9 eV can be attributed to the shake-up satellite of Co $2p_{3/2}$ and Co $2p_{1/2}$, respectively.[9,10] Interestingly, a sharp Co $2p_{3/2}$ peak located at around 778.4 eV was observed in 3DOM Co_9S_8/$Co_2N_{0.67}$@NC, which can be attributed to metallic Co.[11] This observation confirms a further reduced Co chemical state after NH_3 etching. In the XPS spectrum of S 2p (Figure 5.6b), the peaks at 161.5 and 162.5 eV represent Co-S bonding in Co_9S_8.[12-14] The increasing peak intensity of Co-S from 3DOM Co_9S_8/CoO@C to 3DOM Co_9S_8/$Co_2N_{0.67}$@NC further confirm that more highly crystalline Co_9S_8 instead of CoO formed after NH_3 etching, in which intrinsically benefit for both OER and ORR catalytic activity.

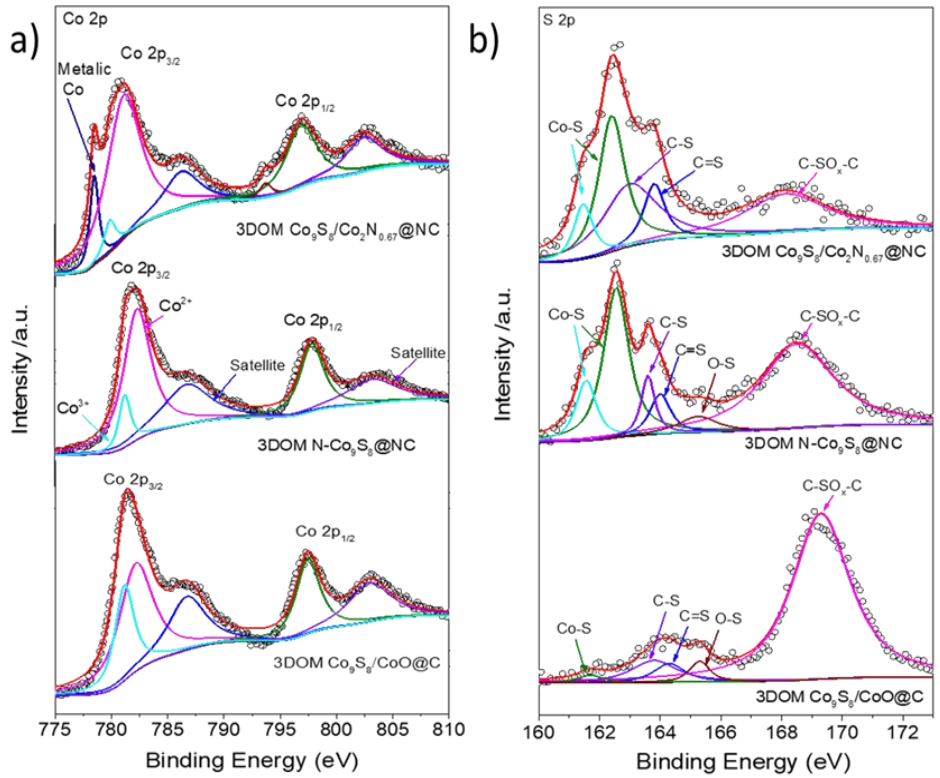

Figure 5.6 High resolution XPS spectra of the a) Co 2p, and b) S 2p in 3DOM Co_9S_8 composites.

Figure 5.7a shows that the C 1s peaks at around 284.8 and 285.8 eV can be assigned to sp^2 graphitic carbon and C-S bonds in 3DOM Co_9S_8/CoO@C. An obvious peak shifting and increasing intensity of C-S (285.5eV) can be observed in both 3DOM N-Co_9S_8@NC and 3DOM $Co_9S_8/Co_2N_{0.67}$@NC, which might resulted from the N-doping in the carbon layer forming C=N bonding.[15] The N-doping of carbon layer, as well as the N-doping of Co_9S_8, is further confirmed with high resolution XPS spectrum of the N 1s, see Figure 5.7b. The N 1s XPS spectra of 3DOM N-Co_9S_8@NC and 3DOM $Co_9S_8/Co_2N_{0.67}$@NC suggesting the presence of pyridinic N (398.4 eV), pyrrolic N (400.5 eV), graphitic N (401.9 eV), and oxidized N (405.0 eV) evidencing the efficient doping of N atoms in the coated-carbon layers.[16,17] On the other hand, the Co–N_x peak at 399.4 eV[18,19] suggests that N atoms were successfully doped into the

Co_9S_8 lattice in 3DOM N-Co_9S_8@NC composite, and forms cobalt nitride in 3DOM $Co_9S_8/Co_2N_{0.67}$@NC. This agree with the N signal in the ELLS mapping (Figure 5.4 b and c). The N-doped carbon is believed has a positive effect on the ORR performance, whereas N-doped Co_9S_8 is believed can boost the electrocatalytic activity toward both ORR and OER. [20,21]

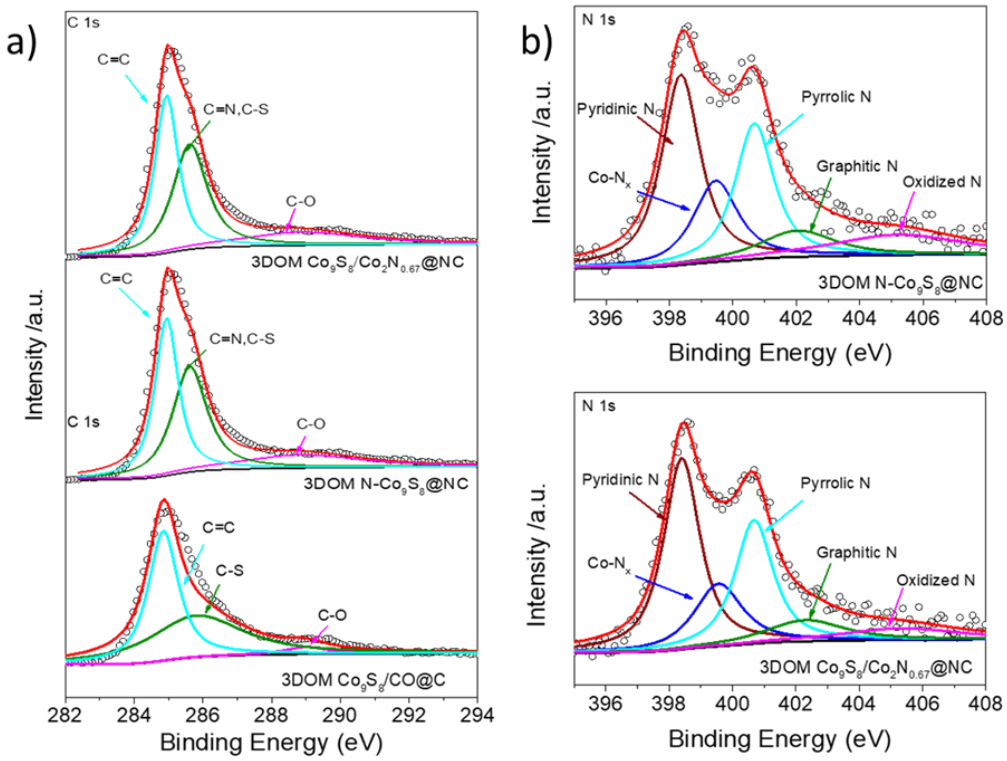

Figure 5.7 High resolution XPS spectra of the a) C 1s, and b) N 1s in the 3DOM Co_9S_8 composites.

Figure 5.8a-b show the electrocatalytic activity of 3DOM Co_9S_8 catalysts for ORR and OER, and commercial Pt/C and Ir/C were used as reference catalysts. The results show that, among the 3DOM composites, 3DOM Co_9S_8/CoO@C obtained in Ar exhibits the lowest ORR (onset potential 0.82 V) and OER (onset potential 1.56 V) activity. Meanwhile, when compared to 3DOM $Co_9S_8/Co_2N_{0.67}$@NC, 3DOM N-Co_9S_8@NC has a much better OER performance (onset potential at 1.52 V) and slightly higher ORR activity with a similar onset potential (0.89 V) but

more positive half-wave potential (0.82 V). When compared to the benchmark precious catalysts, 3DOM N-Co_9S_8@NC shows a comparable ORR and much better OER performance with that of Pt/C and Ir/C, respectively. Although it's ORR onset potential still can't catch up with the Pt/C catalyst (0.97 V), the 3DOM N-Co_9S_8@NC composite has the same half-wave potential (0.82 V) as the Pt/C catalyst at a current density of ~2.7 mA cm^{-2}. The advantage of 3DOM N-Co_9S_8@NC composite is further highlighted by the Kouteck ý–Levich (KL) analysis based on the ORR LSV curves obtained at various rotation speeds (Figure 5.8c). The calculated ORR electron transfer number is 3.84-3.99 (Figure 5.8d), which is very close to the theoretical number 4 in the the pseudo-four electron reaction pathway ($O_2 + H_2O + 4e^- = 4OH^-$). In addition to the good ORR performance, 3DOM N-Co_9S_8@NC composite shows superior OER activity. Specifically, it has a much smaller OER over-potential (339 mV) as that of commercial Ir/C (425 mV) when a current density of 10 mA cm^{-2} is generated. On the other hand, the overpotential for 3DOM $Co_9S_8/Co_2N_{0.67}$@NC and 3DOM Co_9S_8/CoO@C are 368 mV and 388 mV, respectively (Figure 5.8b). This enhanced OER and ORR activity for 3DOM N-Co_9S_8@NC should be attributed to the N-doped Co_9S_8 and the N-doped carbon layer. Additionally, the porous 3DOM hierarchical architecture can provide an expanded surface area, which provides increased number of catalytic active sites and afford more efficient mass transport path for electrolyte as well as electroactive species.

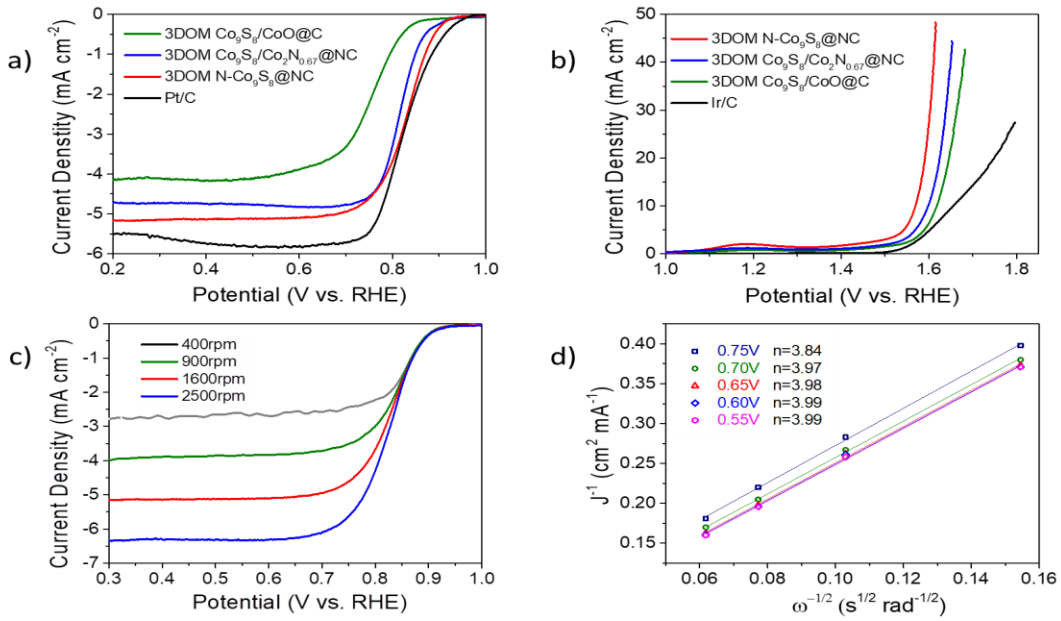

Figure 5.8 a) ORR and b) OER LSV curves of Pt/C, Ir/C and various 3DOM Co_9S_8 composites and obtained at a scan rate of 10 mV s^{-1} in 0.1 M KOH electrolyte at 1600 rpm, respectively; c) LSVs of 3DOM N-Co_9S_8@NC in O_2-saturated 0.1 M KOH at a sweep rate of 10 mV s^{-1} and different rotation rates; d) the corresponding K-L plots (J^{-1} versus $\omega^{-1/2}$) at different potentials.

In addition to the high ORR and OER electrocatalytic activity, the durability of bi-functional catalysts in particular for OER reaction is another key aspect to be considered. Chronoamperometry testing was carried out at a constant potential of 1.65 V *vs.* RHE in N_2 saturated 0.1M KOH solution. It shows that 3DOM N-Co_9S_8@NC electrodes exhibited a 92.5% activity retention over 18 h of continuous operation (Figure 5.9 a), in sharp contrast to precious catalyst Ir/C that showed significant activity loss (16%) as manifested by its gradually decreasing current over time (18h). Moreover, when fabricated into air electrodes and tested in rechargeable zinc-air batteries, the 3DOM N-Co_9S_8@NC catalyst exhibits a similar open circuit voltage (OCV) but longer cycle life than that of Pt/C-Ir/C precious metal catalysts. Figure 5.9b displays the

galvanodynamically charge and discharge polarization curves of the batteries using 3DOM N-Co_9S_8@NC and Pt/C-Ir/C as air electrodes, respectively. It clearly reveals that both of the batteries have almost same OCV (~1.47 V) while the cell with 3DOM N-Co_9S_8@NC (red curves in Figure 5.9 b) exhibits a lower overpotentials, particularly at high current densities, than that of the Pt/C-Ir/C battery (black curve in Figure 5.9 b). Moreover, the cycling performance of the zinc-air battery using 3DOM N-Co_9S_8@NC and Pt/C-Ir/C catalysts were evaluated by performing the galvanostatic charge and discharge test at 10 mA cm^{-2} with each cycle being 2 hours. One can see that the 3DOM N-Co_9S_8@NC fabricated air electrode exhibits a 98% voltage retention after 400 hours' cycling, whereas the battery with Pt/C-Ir/C only stands for 80 hours before displaying severely enlarged overpotentials (Figure 5.9c). Although the 3DOM N-Co_9S_8@NC composite shows superior stability than the Pt/C and Ir/C catalysts in both chronoamperometry and galvanostatic charge and discharge cycling test, the 3DOM structure of 3DOM N-Co_9S_8@NC was found partially crush down to particles after 8 hours' chronoamperometry testing at 1.65 V *vs.* RHE, see Figure 5.10.

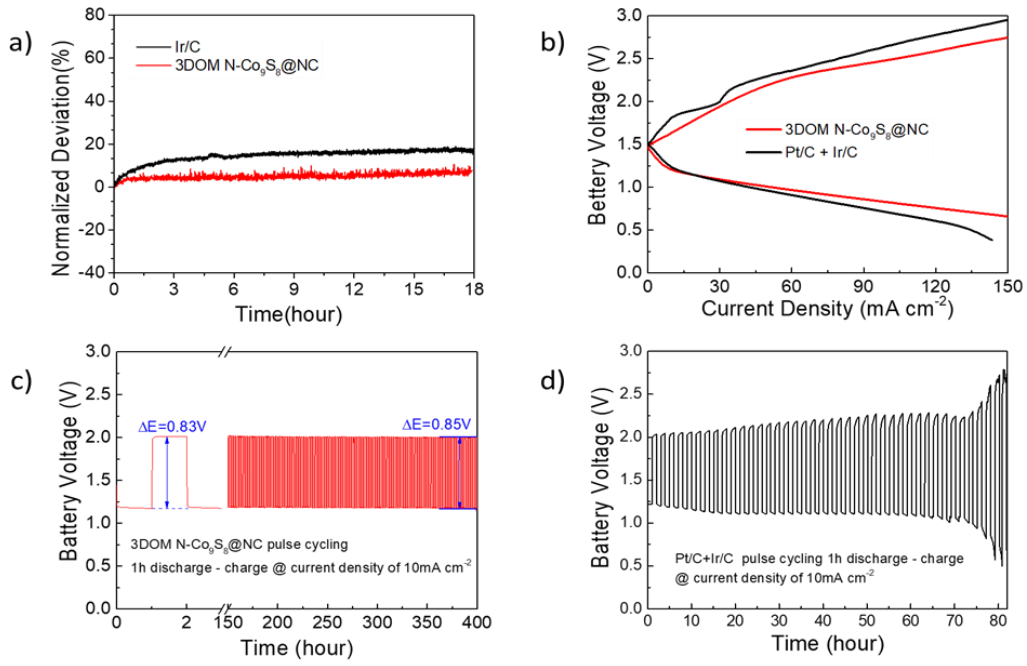

Figure 5.9 a) long-term OER electrolysis stability of 3DOM N-Co_9S_8@NC under constant potential at 1.65 V *vs.* RHE in N_2 saturate 0.1M KOH; b) charge and discharge polarization curves; cycling performance of zinc-air batteries assembled using c) 3DOM N-Co_9S_8@NC and d) Pt/C-Ir/C as air electrodes tested in ambient air.

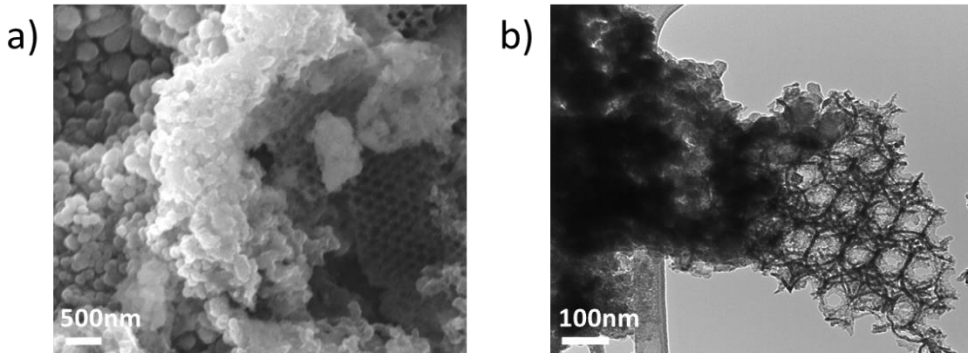

Figure 5.10 a) SEM and b) TEM image of 3DOM N-Co_9S_8@NC after applied 8 hours' constant potential at 1.65 V *vs.* RHE in N_2 saturate 0.1M KOH.

5.4 Summary

In summary, a 3DOM surface engineered N-Co_9S_8@NC composite was designed as an efficient ORR-OER bifunctional catalyst for zinc-air batteries by a facile hard-template method followed by temperature controlled heat treatment process. The 3D hierarchical honeycomb-like mesoporous structure is beneficial for the ORR-OER reactions occur at the gas/catalyst/electrolyte three-phase interface. The presence of N-doped carbon layer lined in the 3D solid network of the porous architecture further enhances the electrical conductivity and ORR activity of the composite catalysts. Such self-supported continuous N-Co_9S_8 porous network provided a 3D through-continuity for maximum accessibility of the active phases to reactants while minimizing agglomeration of the N-Co_9S_8 nanoparticles. With all these merits combined together, the zinc-air battery using the 3DOM N-Co_9S_8@NC catalyst delivers outstanding galvanodynamically charge and discharge performance and achieved long cycling stability over 400 h at 10 mA cm^{-2} current density. All results clearly suggesting that the oxygen catalytic activity and cycling durability were efficiently improved by design active transition metal hybrid into 3DOM self-support porous structure, although partially structure crush was observed after long-time OER testing. Design of a more robust bi-functional oxygen electrocatalyst with high activity will be presented in the next chapter.

CHAPTER 6

Three-dimensional Oxygen Vacancy-rich TiO_xN_y Semiconductor-supported Cobalt Bi-functional Electrocatalyst

In this chapter, an ultrafine Co metal decorated three-dimensionally ordered macroporous titanium oxynitride (3DOM-Co@TiO_xN_y) bi-functional catalyst was presented. It was developed through a new catalyst support design strategy focusing on OV-rich, low-bandgap semiconductor; the OVs promote the electrical conductivity of the TiO_xN_y semiconductor support, and at the same time offer a strong metal-support interaction (SMSI), which gives small Co catalyst size, high catalytic activity, and high stability. The results confirmed that 3DOM-Co@TiO_xN_y exhibits comparable activities for oxygen reduction and evolution reactions, but much higher cycling stability than noble-metals in alkaline conditions. This work sheds light on using OV-rich semiconductors as promising support to design efficient and durable non-precious electrocatalysts. This study is organized as follows: an introduction of this study is presented in Section 6.1. The experimental and computational methods used in this study are described in Section 6.2. Results and discussions are given in Section 6.3. Concluding remarks are stated in Section 6.4.

6.1 Introduction

The practical application of rechargeable zinc-air batteries requires a low-cost, efficient and stable air electrode catalyst toward both the oxygen reduction reaction (ORR) and oxygen evolution reaction (OER). The most promising non-precious bifunctional catalysts are carbon-supported transition metal hybrid materials.[1-9] However, carbon-supported catalysts suffer from carbon electrochemical oxidation, which causes the loss or aggregation of supported catalysts

and degrades the electrocatalysis durability and performance.[2,3] To alleviate this problem, some strategies have been reported including coating the carbon support with corrosion-resistive TiO_2,[4-6] using conductive TiN as an alternative support,[7-9] or developing perovskite oxides as active catalysts.[10-12] However, both TiO_2 and perovskite oxides have an intrinsic low-conductivity drawback, and nor TiN is an optimum support material to obtain highly dispersed and active catalysts due to the non-defective surface structure. Thus, the objective of this study is to develop conductive and oxidation-resistant support to relieve catalyst degradation, and at the same time to achieve a high bifunctional catalytic activity with enhanced durability performance.

Here, we propose that OV-rich, low-bandgap oxide semiconductor can be promising support to design active and durable ultrafine metal catalysts in electrocatalysis (Figure 6.1). This argument is built on our multidisciplinary understanding of OVs in semiconductor physics and heterogeneous solid-gas catalysis: *i)* the OVs lower the bandgap in oxide semiconductors: the higher OVs concentration, the higher conductivity of the oxides;[13,14] *ii)* in solid-gas catalysis, the OVs on oxide supports would provide an SMSI with the supported metal catalysts, and results in high metal dispersion, small metal size, high relative catalytic activity and high stability.[15-20] That is, the OVs are not only beneficial for the conductivity of the oxides, but it also offers an SMSI that favours the formation and stabilization of highly active ultrafine metal nanoparticles. Note that, in electrocatalysis, the role of OVs in metal oxides as active components is well reported for contributing to its enhanced catalytic activities.[21,22] However, the significance of OVs in supporting materials is much less discussed, in particular for processes involving the oxidative OER reaction. To the best of our knowledge, this is the first time that the concept of OVs-induced SMSI is introduced to design active and stable semiconductor-based electrocatalysts with ultrafine dispersion of the active phase for ORR and

OER.

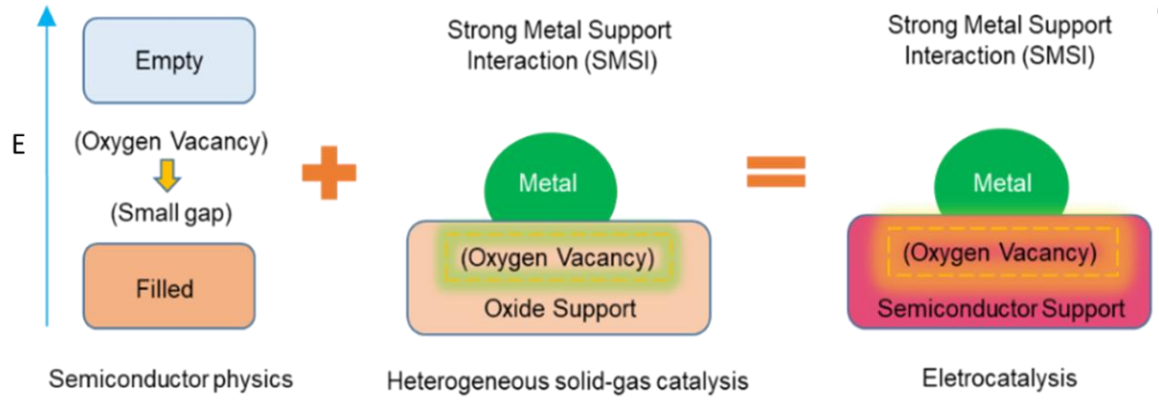

Figure 6.1 The design strategy for semiconductor-supported metal as electrocatalysts.

In this work, we developed an efficient and durable bifunctional catalyst which comprises OV-rich 3DOM TiO_xN_y supported ultrafine Co, referred to as 3DOM-Co@TiO_xN_y. The as-developed 3DOM-Co@TiO_xN_y catalyst exhibits good ORR-OER activities and superior stability in alkaline conditions. The zinc-air battery using this catalyst delivers excellent stability with less than 1% energy efficiency loss over 900 charge-discharge cycles at 20 mA cm^{-2}. The high stability is attributed to the strong SMSI between Co and 3DOM-TiO_xN_y which verified by density functional theory (DFT) calculations. This work guides the design of efficient and durable non-precious electrocatalysts using OV-rich semiconductors as promising support materials.

6.2 Experimental and Computational Details

6.2.1 Catalyst preparation

The 3DOM-Co@TiO_xN_y catalyst was prepared using polystyrene (PS) sphere as template. The PS spheres have an average diameter of ~200 nm and were synthesized through emulsion polymerization using styrene, polyvinylpyrrolidone (PVP), potassium persulfate, and DDI water (Figure 6.2). Detailed information about the synthesis of PS spheres can be found in [23].

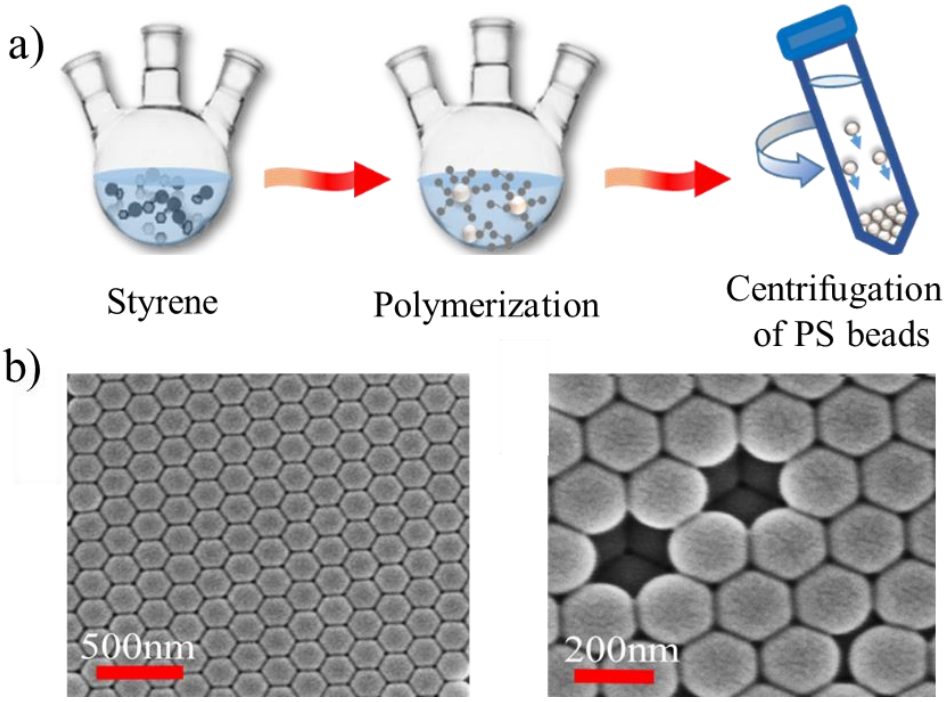

Figure 6.2. a) Schematic of preparation procedure for PS beads; b) low and high magnification SEM images of PS template.

For the preparation of 3DOM-Co@TiO_xN_y, 178mg cobalt acetate [$Co(CH_3COO)_2 \cdot 4\ H_2O$] was dissolved in a 11 mL solution that mixed from ethanol (EtOH), titanium butoxide [$Ti(OBu)_4$] and hydrochloric acid (HCl) solutions [EtOH:$Ti(OBu)_4$:HCl volumetric ratio=5:5:1] at room temperature. The as-obtained precursor solution has a Co:Ti atomic ratio of 1:20 and was added drop-wisely to the PS template (1mL precursor:1mg PS) under vacuum filtration. The infiltrated PS template was dried overnight. Then, the PS template was removed by calcination in Ar and NH_3 using the following heating program: from room temperature to 300 ℃ and stay at 300 ℃

for 1 h, heat up to 540 ℃ and keep 1 h, raise the temperature to 800 ℃ and keep for 20min. The ramping rate is 1 ℃/min. Then, the gas atmosphere is switched from Ar to NH_3 and keeps at 800 ℃ for 40min. After that, the gas is switched back to Ar and cool down to room temperature. The resulting powder product was referred to as 3DOM-Co@TiO_xN_y (Figure 6.3).

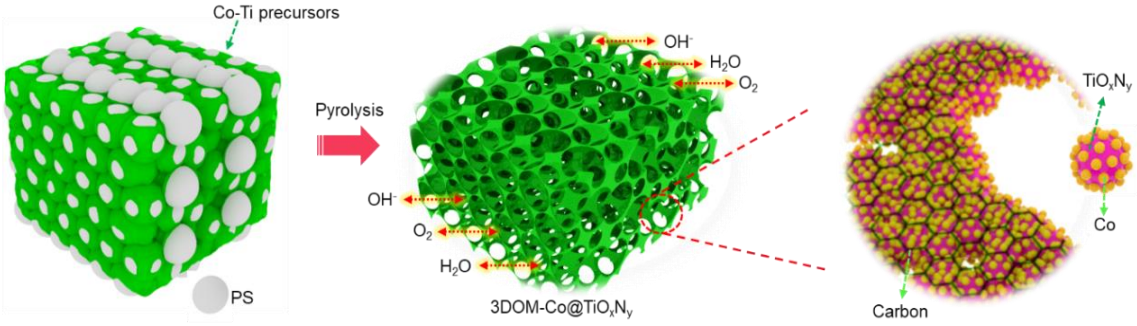

Figure 6.3 Schematic of preparation procedure for 3DOM-Co@TiO_xN_y catalyst, and the Co interface-confinement effect induced by SMSI and carbon layer.

Note that the Co composition or Co:Ti ratio in 3DOM-Co@TiO_xN_y can be tuned by changing the amount of $Co(OAc)_2 \cdot 4H_2O$ in the precursor solution. For optimization purpose, 3DOM-Co@TiO_xN_y composites with Co:Ti atomic ratio of 1:80 and 4:20 were also prepared, which are referred to as 3DOM-Co@TiO_xN_y (1:80) and 3DOM-Co@TiO_xN_y (4:20), respectively. With the absence of $Co(OAc)_2 \cdot 4H_2O$ in the precursor solution, the as-obtained product is named as 3DOM-TiO_xN_y (Figure 6.4). Moreover, in addition to the 3DOM-Co@TiO_xN_y obtained with 40mins NH_3 treatment, two other Co@TiO_xN_y samples were also developed by changing the duration of NH_3 treatment (10mins and 1hour), which were referred to as 3DOM-Co@TiO_xN_y (in NH_3 10min) and 3DOM-Co@TiO_xN_y (in NH_3 1h), respectively. The oxidized form of the 3DOM-Co@TiO_xN_y was also synthesized by annealing the 3DOM-Co@TiO_xN_y sample in air at 450℃ for 2 hours. The resulting product was identified as Co_3O_4@TiO_2, as seen in Figure 6.4.

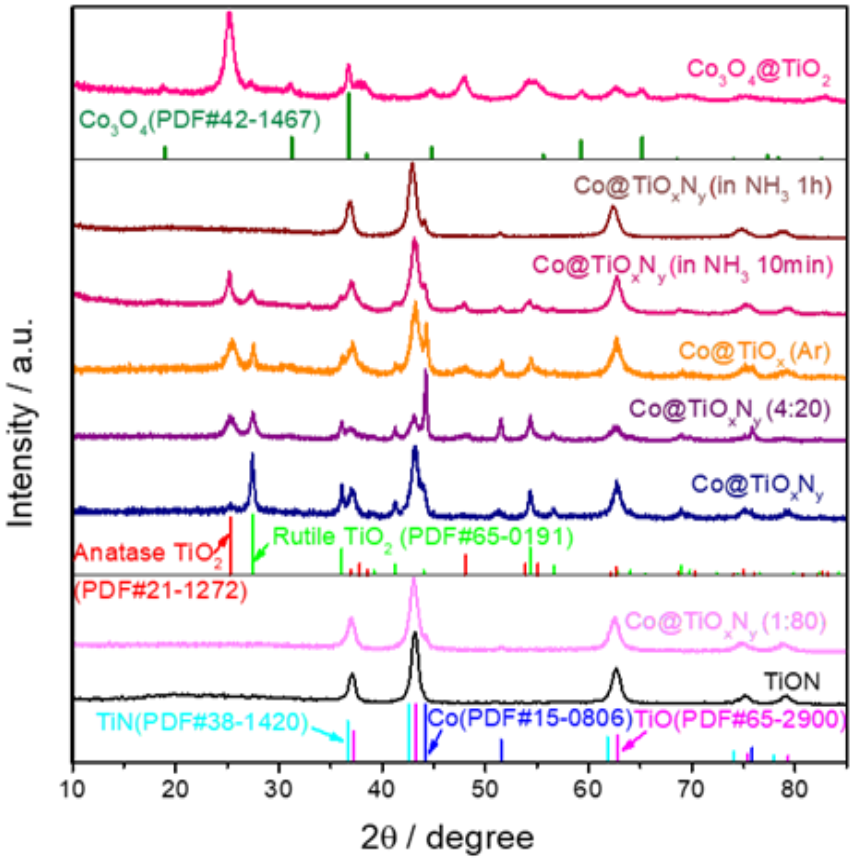

Figure 6.4 XRD patterns of various 3DOM composites.

6.2.2 Material characterization

The morphologies and microstructures of the as-prepared catalysts were characterized using scanning electron microscopy (SEM, LEO FESEM 1530) and transmission electron microscopy (TEM, JEOL 2010F). Their crystal structures were investigated using X-Ray Diffraction (XRD, Rigaku Miniflex 600). The surface chemical composition of the samples was analyzed by X-ray photoelectron spectroscopy (XPS), A Gaussian-Lorentzian mix is used while analyzing XPS peaks. The background used was the "Smart" background, which is a corrected Shirley background. The binding energy scale was calibrated to fix the carbon sp3 peak at 284.8 eV [24].

Brunauer-Emmett-Teller (BET) analysis was performed to evaluate the surface area of 3DOM-Co@TiO_xN_y composite.

6.2.3 Electrochemical evaluation

The ORR-OER performance of the as-prepared 3DOM composite catalysts was evaluated using a three-electrode glass cell in 0.1 M KOH solution. An SCE electrode and graphite rod was used as the reference and counter electrodes, respectively. The working electrode is the glassy carbon rotating disk electrode (RDE) loaded with 3DOM catalyst. The catalyst inks were prepared by dispersing 2 mg of catalyst and 2 mg of Vulcan XC-72 in 1 mL of ethanol containing 0.2 wt% Nafion ionomer. The ink was sonicated for 30min. Then, 25 μL of catalyst ink was drop-casted onto the RDE electrode, which results in an overall loading of 0.5 mg cm^{-2}. This includes 0.25 mg cm^{-2} active catalysts (e.g. 3DOM Co@TiO_xN_y) and 0.25 mg cm^{-2} Vulcan XC-72, respectively. The ORR and OER activities of the 3DOM catalysts were measured under O_2 and N_2 saturated 0.1M KOH, respectively, at a scanning rate of 10 mV s^{-1}. The same procedure is applied to measure the ORR and OER activity of commercial precious catalysts Pt/C (28.8 wt. % Pt) and Ir/C (20 wt. % Ir), respectively, with a loading of 0.2 mg cm^{-2}. This loading of commercial Pt/C and Ir/C catalysts is commonly used as reference loading in the literature, and their catalytic performances measured in this work are in line with reported works.[25,26]

Saturated calomel electrode (SCE) is used as the reference electrode in all RDE testing. The calibration of SCE was performed by measuring the voltage ΔE between the SCE and a Pt wire immersed in the high purity hydrogen saturated 0.1 M KOH electrolyte.[27] The measured ΔE between SCE and RHE is 0.996V. Then RDE potentials are calibrated and given as referred to RHE using the equation: $V_{RHE}=V_{SCE}+0.996$ V.

The electrochemical performance of 3DOM-Co@TiO_xN_y in zinc-air battery was tested using a multichannel potentiostation (Princeton Applied Research, VersaSTAT MC). The catalyst was spray-coated onto carbon paper and was used as cathode. The catalyst loading is 1.0 mg cm^{-2}. The anode and separator are zinc-plate and microporous membrane, respectively. The electrolyte is 6.0M KOH solution with 0.2M $Zn(CH_3COO)_2$. The galvanodynamic charge and discharge profiles of the battery were obtained by scaled the current density from 0 to 0-150 mA cm^{-2}. The cycling tests were conducted at a current density of 20 mA cm^{-2} with 10min discharge and 10min charge time for each cycle. The tests were operated in ambient air condition.

6.2.4 Computational Details

The DFT calculation was carried out using the generalized gradient approximation (GGA) with the Perdew-Burke-Ernzerhof (PBE) exchange and correlation functional.[30] All calculations were performed using the VASP package.[31,32] A Dudarev "+U" term acting on the Ti 3d states (referred as GGA + U) was applied. The U value was set to 3.8eV.[33] A plane-wave cutoff of 400eV was used. The Brillouin zone was integrated using the Monkhorst-Pack sets of 2×2×1 k-points mesh. The stoichiometric rutile TiO_2 (110) and (100) surfaces were modelled by nine-atomic layered slabs with a (3×2) and (3×2) unit cell, respectively. On the other hand, the stoichiometric TiO (110) and (100) surfaces were represented by nine-atomic layered slabs using 2×1 and 2×2 unit cell, respectively. The tetrahedral Co_4 cluster is adopted to model Co nanoparticle because it is the smallest 3D unit that can provide a three-dimensional structure to probe both metal-metal and metal-support interactions.[34,35] All the slabs have a vacuum height of 15 Å. During the calculations, the bottom two atomic layers were fixed, whereas the remaining layers and the adsorbates were allowed to relax. Structures are fully relaxed until the forces acting on the atoms are smaller than 0.03 eV/Å. The reduced TiO_2 (110) and (100)

surfaces (contains vacancy) were constructed by placing three and four oxygen vacancies on the bridging oxygen rows in their stoichiometric TiO_2 surfaces, respectively.[36] The reduced TiO (110) and (100) surfaces were built by removing three and two oxygen sites on the topmost layer of their stoichiometric surfaces. The metal-support adhesion interaction (E_{adh}) was calculated by the following equation: E_{adh}= -($E_{support+metal}$- $E_{support}$-E_{metal}), where $E_{support+metal}$ represents the total energy of the supported system, $E_{support}$ and E_{metal} are the energy of isolated support and metal system, respectively.

6.3 Results and Discussion

As discussed in the experimental section, the 3DOM-Co@TiO_xN_y bi-functional catalyst was prepared by thermal treating PS template soaked with cobalt acetate [$Co(CH_3COO)_2 \cdot 4H_2O$] and titanium butoxide [$Ti(OBu)_4$] precursor solution with an atomic ratio of Co:Ti=1:20. At different heating stages, Ar and NH_3 atmosphere was used. This ensures an oxygen-deficient and reductive environment that is beneficial for OVs formation in the TiO_xN_y support. It should be mentioned that the calcination of PS beads not only forms the 3DOM morphology, but also generates an N-doped carbonaceous layer enwrapping the Co@TiO_xN_y framework (Figure 6.3). Such N-doped carbon layer is introduced mainly to improve the ORR activity of the composite [9] rather than as conductive supporting material. The carbon layer also provides further confinement for ultrafine Co metal catalyst on TiO_xN_y (Figure 6.3), which will be discussed later. The crystal components of Co@TiO_xN_y were identified as metallic Co, TiO, TiN and rutile TiO_2 through XRD analysis (Figure 6.5, before OER). For the sake of comparison, 3DOM composites without the addition of Co precursor or ammonolysis treatment were also developed. The resulting products were identified and referred to as 3DOM-TiON and 3DOM-Co@TiO_x (Ar), respectively (Figure 6.4).

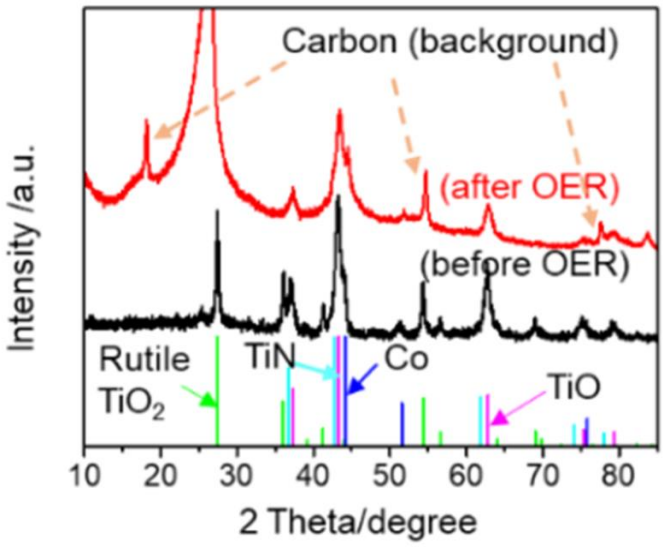

Figure 6.5 XRD patterns of 3DOM-Co@TiO_xN_y before and after OER reaction

Figure 6.6a shows the 3DOM morphology of the 3DOM-Co@TiO_xN_y composite: it has macroporous pores of ~150 nm and interconnected walls, providing a strong structural support for the composite. Scanning transmission electron microscopy (STEM) image shows that the 3DOM interconnected walls are built by aggregated nanoparticles (Figure 6.6b).

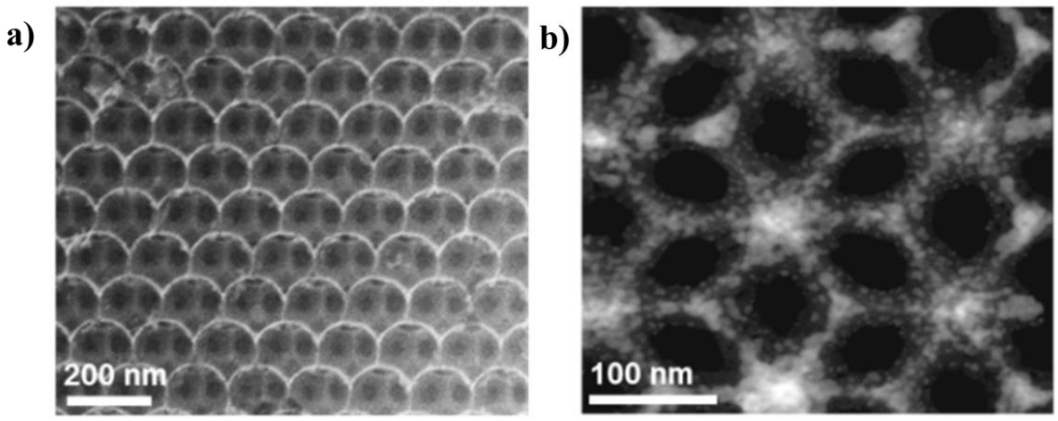

Figure 6.6 a) SEM and b) STEM image of 3DOM-Co@TiO_xN_y.

Interestingly, the 3DOM-Co@TiO_xN_y was found featured with an IV type N_2 absorption-

desorption isotherm, [37] seen in Figure 6.7. This indicates that, in addition to the macropores, it contains mesopores, leading to a high Brunauer-Emmett-Teller (BET) surface area of 266 m^2 g^{-1}. Together with its 3DOM porous structure, the high surface area ensures high availability of active sites, and low mass transfer resistance within the catalyst, which is beneficial for the electrochemical performance of the catalyst.

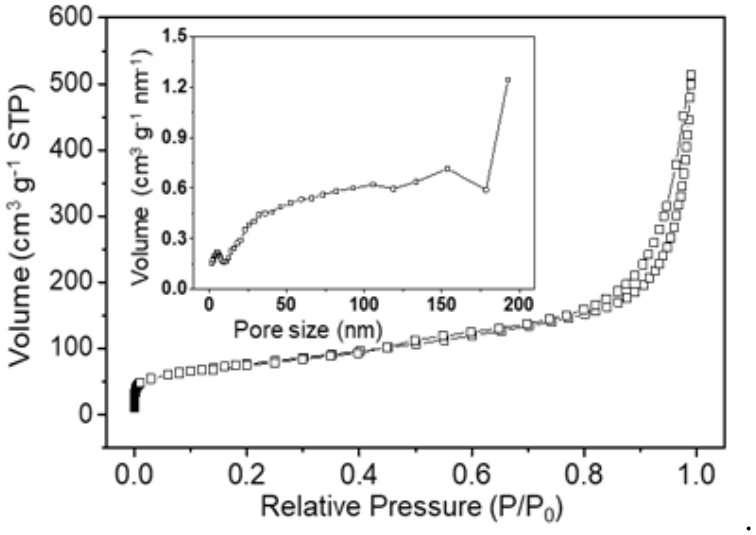

Figure 6.7 N_2 adsorption-desorption isotherms and pore size distribution of 3DOM-Co@TiO_xN_y composite.

Figure 6.8 shows the high magnification electron energy-loss spectroscopy (EELS) mapping of the 3DOM-Co@TiO_xN_y catalyst. It reveals that the aggregated nanoparticles formed the 3DOM walls, as observed in STEM, are TiO_xN_y, and their outer surfaces are homogeneously covered with Co with an atomic composition of 0.79%, see Table 6.1.

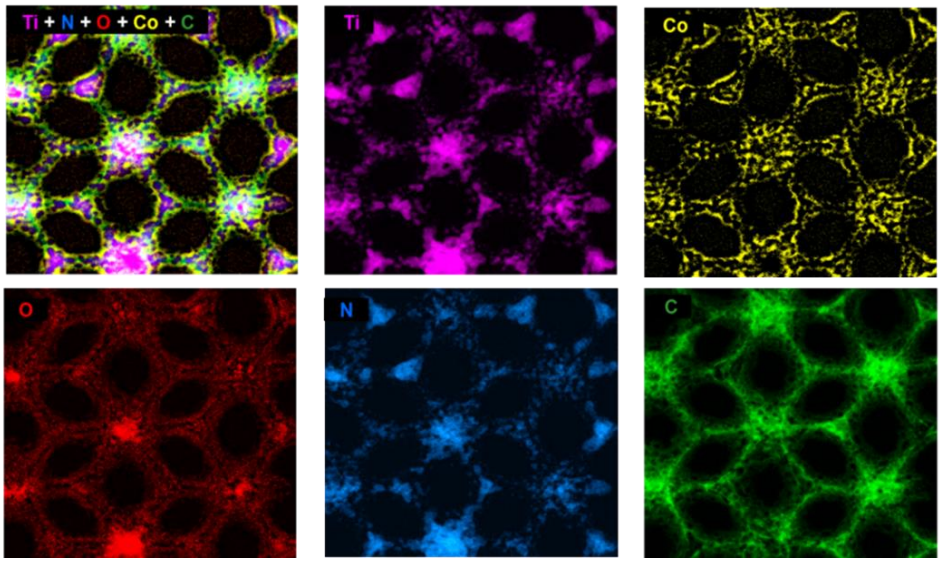

Figure 6.8 STEM-Electron energy-loss spectroscopy (STEM-EELS) elemental mapping (Ti, Co, O, N, and C) of 3DOM-Co@TiO_xN_y.

Table 6.1 XPS surface atomic composition of the as-prepared 3DOM-Co@TiO_xN_y and 3DOM-Co@TiO_x (Ar) composites

	Ti	Co	C	O	N
3DOM-Co@TiO_xN_y	12.62	0.79	58.07	18.85	9.67
3DOM-Co@TiO_x (Ar)	17.07	1.18	44.38	37.37	

A high resolution STEM mapping image shows that the Co@TiO_xN_y nanoparticles appear to exhibit the 'core-shell' structure (Figure 6.9a). Additionally, one can see that C element is uniformly distributed on the outermost surface layer of the Co@TiO_xN_y particles, suggesting there is a carbon layer covering the 3DOM walls. This carbon layer not only improves the

conductivity of the composite, but may also act as a confining layer to restrict ultrafine Co onto TiO_xN_y, and therefore can further contribute to the stability of the 3DOM-Co@TiO_xN_y. To distinguish the contribution of the carbon layer and TiO_xN_y components to the composite conductivity, the electrical conductivity of 3DOM-Co@TiO_xN_y and 3DOM-Co@TiO_x (Ar) were measured. Both of the composites have a carbon layer. However, the conductivity of 3DOM-Co@TiO_xN_y (5.11 S cm^{-1}) is one order of magnitude higher than that of 3DOM-Co@TiO_x (Ar) (0.76S cm^{-1}), seen in Figure 6.9b. This shows the conductivity of the 3DOM-Co@TiO_xN composite is mainly contributed by TiO_xN_y rather than the carbon layer. All of these observations strongly support the successful synthesis of ultrafine Co on conductive TiO_xN_y. Note that, the high resolution TEM (HRTEM) image of the 3DOM-Co@TiO_xN_y composite and the corresponding FFT pattern further confirm the existence of ultrafine metallic Co phase on TiO_xN_y (Figure 6.10).

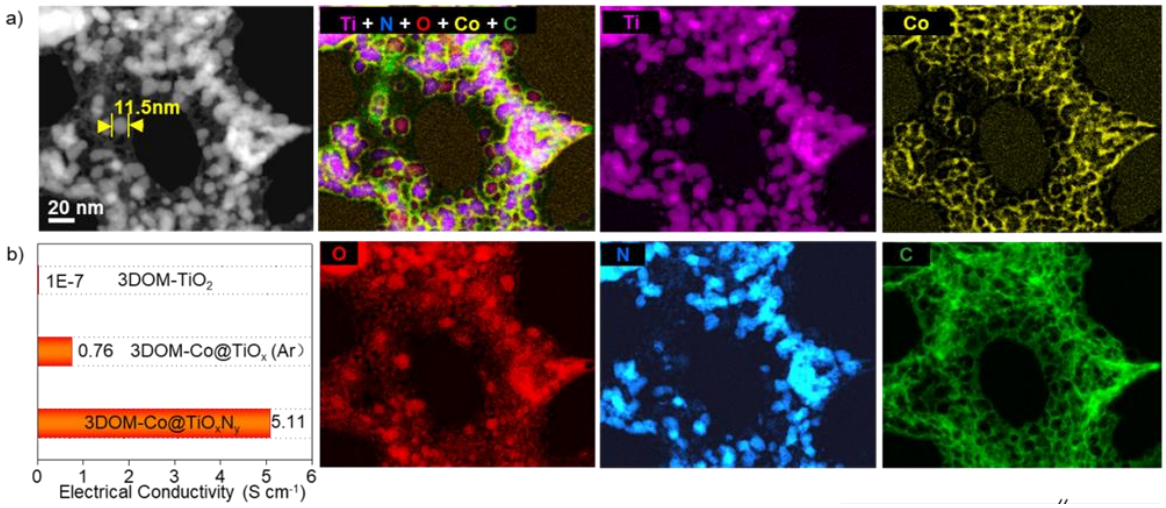

Figure 6.9 a) STEM image and high magnification STEM-EELS mapping of Ti, Co, O, N, and C elements; b) Electrical conductivity of 3DOM-Co@TiO_xN_y.

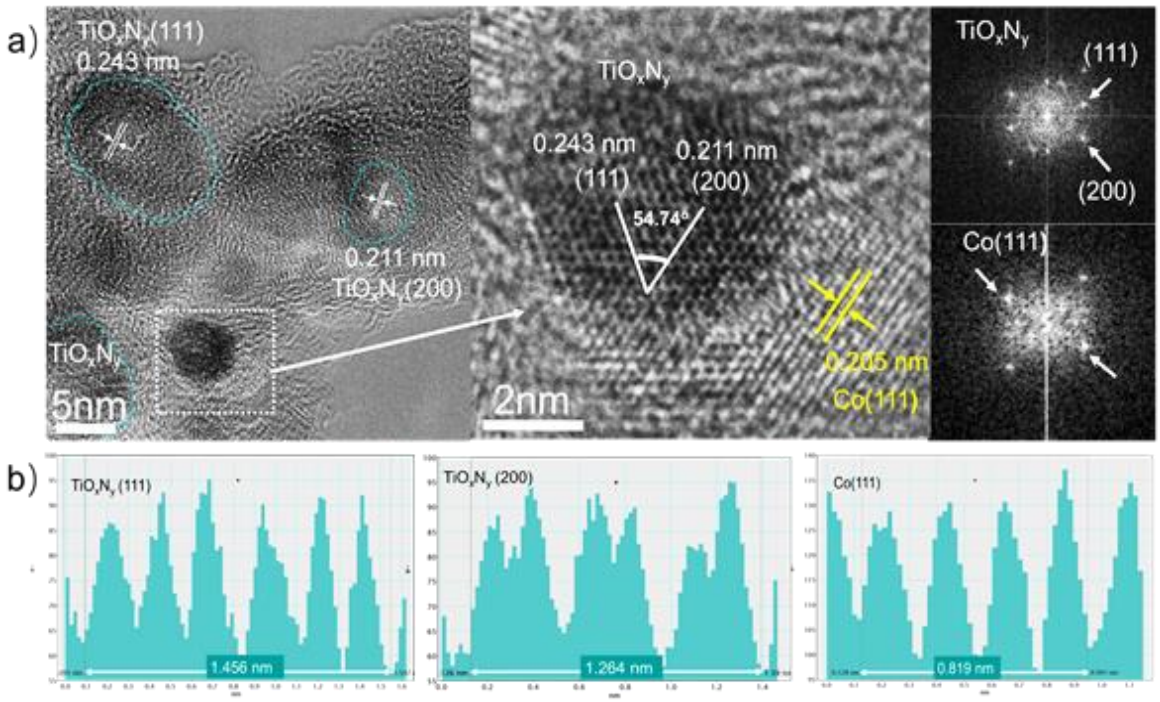

Figure 6.10 a) HRTEM images and corresponding FFT pattern of 3DOM-Co@TiO_xN_y composite; b) Line profiles of the d-spacing of the Co@TiO_xN_y in (a).

The local chemical environment on the surface of 3DOM-Co@TiO_xN_y (before OER) was examined by XPS. Its Ti 2p spectrum was deconvoluted into three overlapping doublets (Figure 6.11a). The minor Ti $2p_{3/2}$ peak located at 455.2 eV can be assigned to TiN or TiO. The other two peaks centred at 456.8 eV and 458.3 eV are referred to as TiON and reduced TiO_{2-x} or Ti_2O_3, respectively.[38,39] The Ti $2p_{3/2}$ signal at 459.1 eV associated with TiO_2 is very weak, which confirms the low oxidation state of Ti in TiO_xN_y. The Co 2p spectrum of 3DOM-Co@TiO_xN_y has a characteristic $2p_{3/2}$ peak of CoO rather than metallic Co, suggesting the ultrafine Co was mildly oxidized in the air (Figure 6.11b). The N 1s spectrum shows the existence of N-Ti-O (396.2 eV), N-Ti (397.2 eV) and N-C components in TiO_xN_y [40,41] (Figure 6.11c). The OVs in 3DOM-Co@TiO_xN_y was probed by the O 1s XPS spectrum (Figure 6.11d). The peak at 530.1 eV is associated with lattice O^{2-} from O-Ti or O-Co bond, [42,43] and the peak at 531.6 eV

represents the non-lattice (defective) O^{2-} or OH species.[44] Although the formation of OH species on the catalyst surface is possible, e.g. its exposure to the ambient atmosphere, the defective O^{2-} is consistent with the wide distribution of Ti^{2+}, Ti^{3+} and Ti^{4+} states in the Ti 2p spectrum (Figure 6.11a), indicative of enrichment of OVs on the TiO_xN_y surface. The locations of OV can be distributed across both of the TiO and TiO_2 lattice of TiO_xN_y. This is because i) TiO itself is commonly featured with high OV content (11~20%); [45] ii) TiO_2 with OV has been reported to be obtained in a low-oxygen atmosphere,[46,47] therefore the existence of OV in TiO and TiO_2 lattice obtained under the strong reducing atmosphere of NH_3 is inevitable.

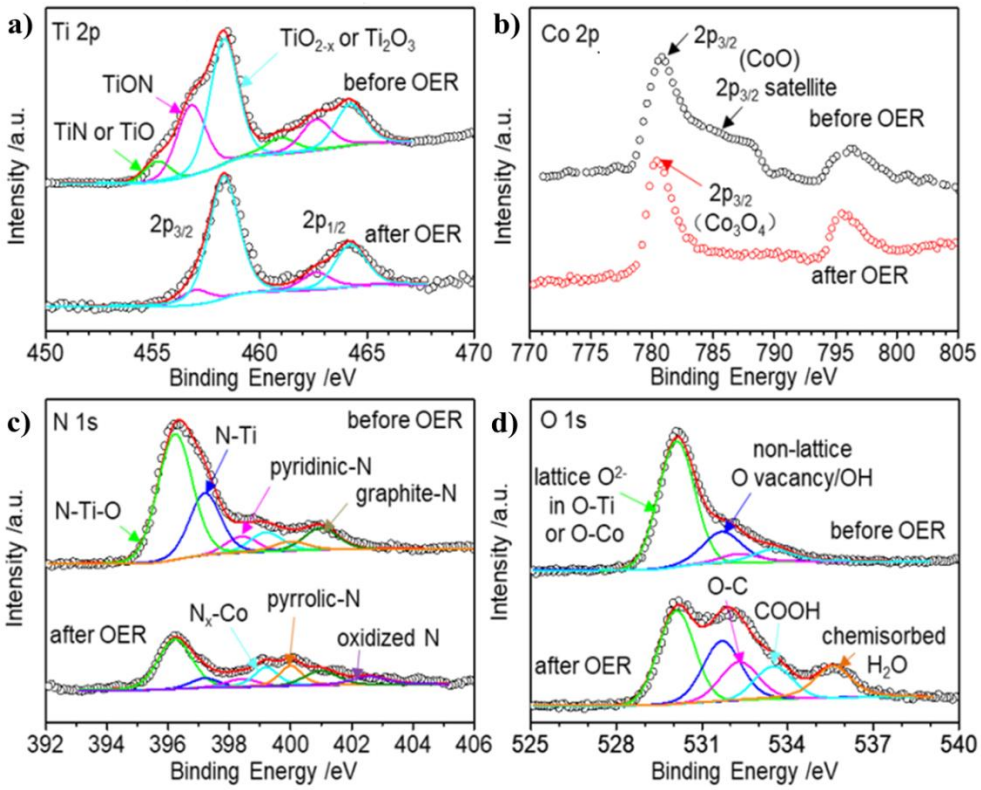

Figure 6.11 a) Ti 2p; b) Co 2p; c) N 1s; and d) O 1s XPS spectrum of 3DOM-Co@TiO_xN_y before and after 16 hours of OER half-cell test at a constant potential of 1.60V vs. RHE.

Further evidence of the OV comes from a close inspection of the shape of the O-K (O 1s→2p)

and Ti-L (Ti 2p→3d) core edges of EELS spectrum of 3DOM-Co@TiO_xN_y (Figure 6.12), which provides chemical and electronic information on buried atoms that are in a bulk-like environment.[48] The O-K edge fine structure has been reported sensitive to O-O ordering, and damps out as the OVs concentration increases.[49] As shown in Figure 6.12, the O-K edge fine structure 'washes out' in 3DOM-Co@TiO_xN_y compared with that of 3DOM-Co@TiO_x (Ar), indicating the high OVs concentration in TiO_xN_y. This is also consistent with the distinct peak shift in Ti-L edge towards low photon energy, as OVs are electron donors. The Co-L edge signal is not apparent, supportive for the low loading of Co (0.79%) on TiO_xN_y.

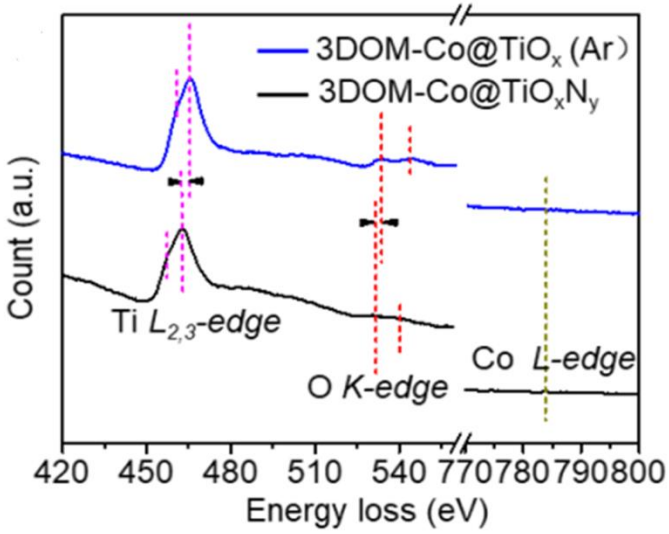

Figure 6.12 Comparison of EELS spectra of Ti-L, O-K and Co-L core edges acquired from the as-prepared 3DOM composites.

The beneficial effect of OVs in SMSI within Co-TiO_xN_y was supported by DFT calculations. Here, TiO_2 and TiO surface were used as representative crystals for 3DOM-Co@TiO_xN_y because they are the two main crystalline oxides in TiO_xN_y observed in our pre- and post-OER XRD analysis (Figure 6.5). The Ti-N component is neglected to simplify the DFT model. This is a reasonable assumption because we only focus on the OV sites. The (110) and (100) surfaces are

used to model the TiO_x oxides because they are the reported stable surfaces on rutile TiO_2,[50] and featured planes for TiO as well. The adhesion energy of tetrahedral Co_4 cluster on the OV sites of non-stoichiometric cubic TiO and rutile TiO_2 (110) surfaces are 12.13 eV and 12.98 eV, respectively, indicative of the SMSI (Figure 6.13). In addition, we found that, for (110) surface, the 3D Co_4 cluster was stable only on the non-stoichiometric (reduced) surfaces, whereas distortion of the Co_4 cluster occurs on the stoichiometric surface. For instance, on the stoichiometric TiO_2 (110) surface, although it has a much higher adhesion energy (19.65 eV) than that on reduced rutile TiO_2 (110), the severe distortion of Co_4 cluster results in many Co-O bonds, suggesting that the stoichiometric TiO_2 (110) surface is not favourable for the nucleation of metallic Co.

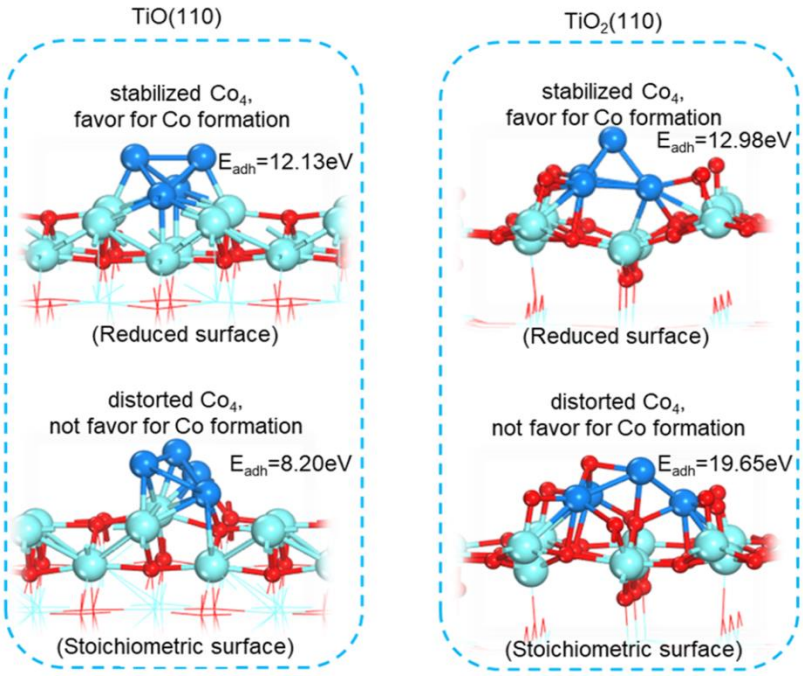

Figure 6.13 The most stable geometries and the corresponding adhesion energy of Co_4 cluster on reduced and stoichiometric TiO and TiO_2 (110) surface: blue (Co), cyan (Ti), red (O).

On the (100) surface of TiO_2 and TiO, the tetrahedral structure of Co_4 cluster is preserved,

and the non-stoichiometric (reduced) TiO_2 and TiO exhibit stronger SMSI than that on stoichiometric model (Figure 6.14). Moreover, we found that on both of the reduced (110) and (100) surfaces, the Co tends to incorporate into the TiO_2 and TiO lattice, revealing that the OV act as sites for the Co nuclei. Thus, we can further infer that, in addition to providing an SMSI, OV sites on the reduced surfaces also act as nucleation sites for Co growth during calcination. That is, the OV sites are essential in the nucleation and stabilization of the ultrafine metals. This is also supported by the fact that surface defects acting as preferred nucleation sites for the growth of metal particles have been widely recognized.[51,52]

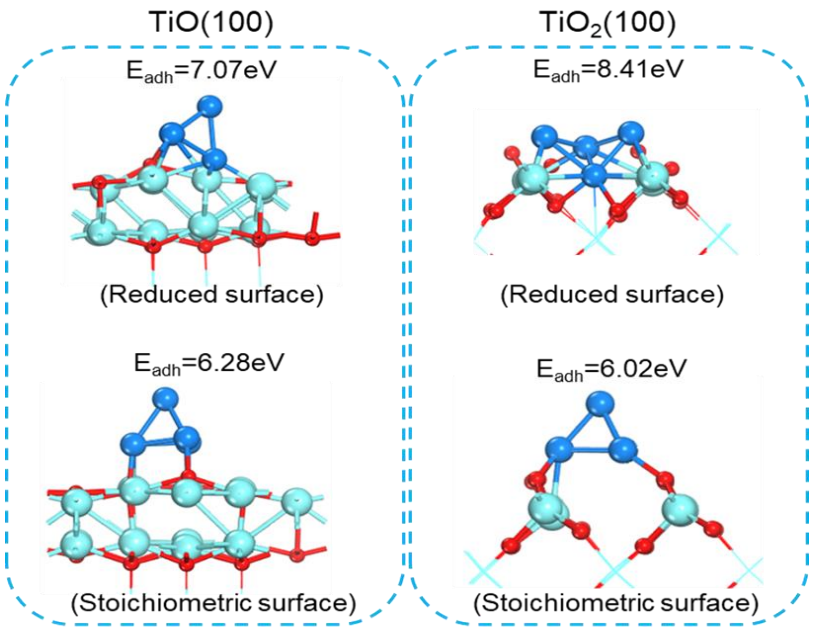

Figure 6.14 The most stable geometries and the corresponding adhesion energy of Co_4 cluster on reduced and stoichiometric TiO and TiO_2 (100) surface: blue (Co), cyan (Ti), red (O).

The electrocatalytic activities of the 3DOM composites were evaluated by linear sweep voltammetry (LSV) with 0.1 M KOH solution. Figure 6.15 shows that 3DOM-Co@TiO_xN_y delivers an ORR onset potential of 0.90 V (vs. RHE). Although its onset potential still can't catch up with that of Pt/C catalyst (0.98V), 3DOM-Co@TiO_xN_y exhibits a comparable ORR

half-wave potential (0.84 V) to that of Pt/C (0.85 V). Meanwhile, it also shows much higher ORR activity than the Co-free 3DOM-TiON and N-free 3DOM-Co@TiO_x (Ar). The linearity of the K-L plot and the number of electrons (n=4.0) transferred during ORR also indicate fast kinetics throughout the potential range inspected (Figure 6.16 a-b).

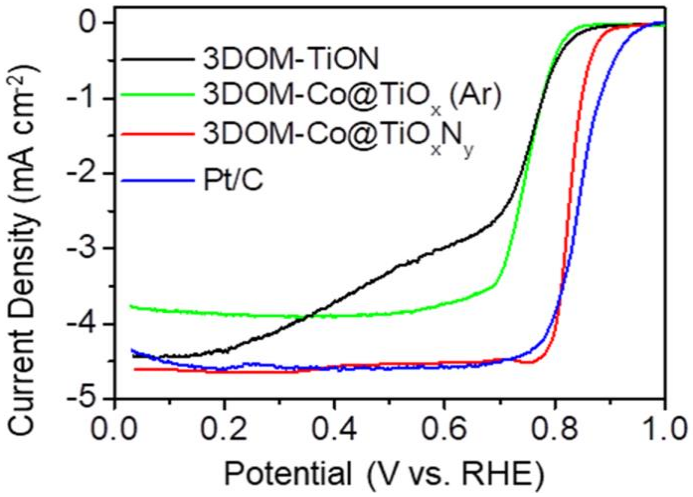

Figure 6.15 ORR LSV curves of various 3DOM composites obtained at a scan rate of 10 mV s^{-1} in 0.1 M KOH electrolyte at 900 rpm.

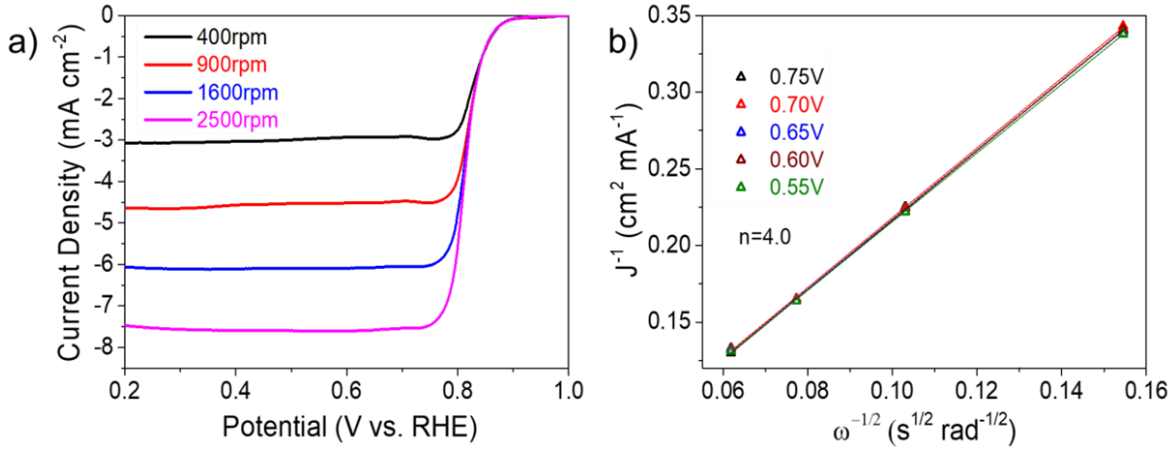

Figure 6.16 a) LSVs of 3DOM-Co@TiO_xN_y in O_2-saturated 0.1 M KOH at sweep rate of 10 mV s^{-1} and different rotation rates; b) the corresponding K-L plots (J^{-1} versus $\omega^{-1/2}$) at different potentials.

In the case of OER, 3DOM-Co@TiO_xN_y exhibits the highest activity among the 3DOM composites (Figure 6.17). For example, when a current density of 10 mA cm^{-2} is generated, it has a similar OER overpotential (~385 mV) as that of commercial Ir/C, whereas the overpotential for N-free 3DOM-Co@TiO_x (Ar) (417 mV) is slightly higher. The Co-free 3DOM-TiON composite has only minor OER activity, suggesting Co is the active component for OER. The high ORR and OER activity of 3DOM-Co@TiO_xN_y was further confirmed by its Tafel plot (Figure 6.18a-b).

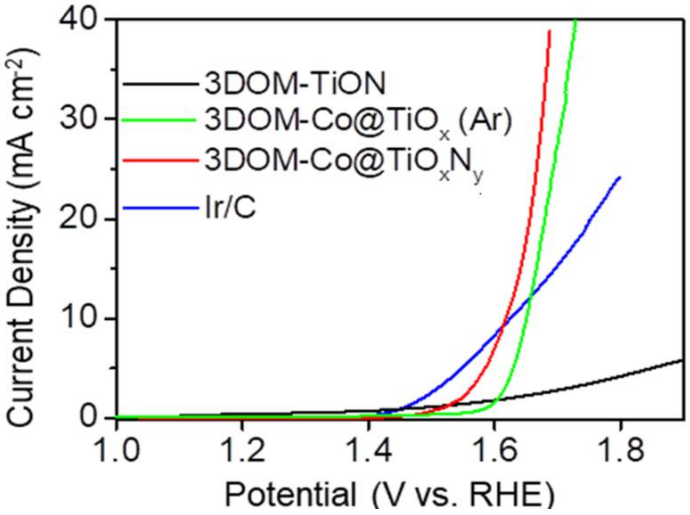

Figure 6.17 OER LSV curves of various 3DOM composites obtained at a scan rate of 10 mV s^{-1} in 0.1 M KOH electrolyte at 1600 rpm.

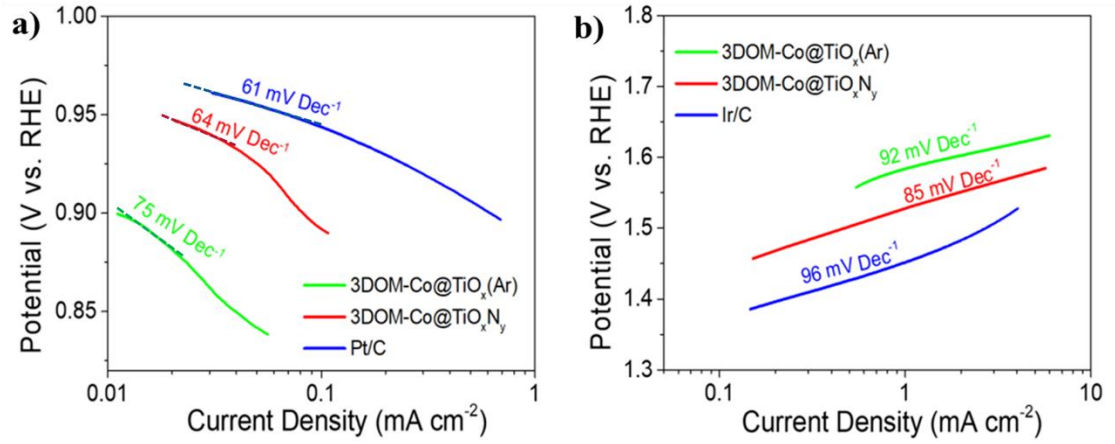

Figure 6.18 a) ORR; and b) OER Tafel plots of 3DOM-Co@TiO_xN_y, respectively.

In the above analyses, the activity of the 3DOM catalysts and commercial Pt/C or Ir/C catalysts was evaluated based on the geometry area of RDE electrode. The OER activity of as-developed catalysts were also normalized by the electrochemically active surface area (ECSA), which can be evaluated from the double-layer capacitance (C_{dl}) using the following equations [53]:

$$i_c = vC_{dl} \qquad (6-1)$$

$$\text{ECSA} = \frac{C_{dl}}{C_s} \qquad (6-2)$$

where i_c is the charging current, which can be measured from CVs at multiple scan rates. v is scan rate. The C_{dl}, can be determined as a slope by plotting i_c against scan rate. C_s is specific capacitance, which can be set to 0.035 mF cm^{-2} for 1.0M KOH solution [8].

Figure 6.19a-c) show the CVs obtained for the 3DOM catalysts, and their corresponding C_{dl} determined by CVs in the potential range of 1.1-1.30 V without redox processes. Figure 6.19d-f) show that the C_{dl} of 3DOM-Co@TiO_xN_y slightly surpass that of 3DOM-Co@TiO_x (Ar), and both of them are higher than that of 3DOM-TiON. The OER activities of these as-developed

catalysts normalized by ECSA also show a similar trend with that normalized by the geometry area of RDE electrode (Figure 6.19), revealing that the activity enhancement of 3DOM-Co@TiO_xN_y is due mainly to an increase in intrinsic surface specific activity of 3DOM-Co@TiO_xN_y.

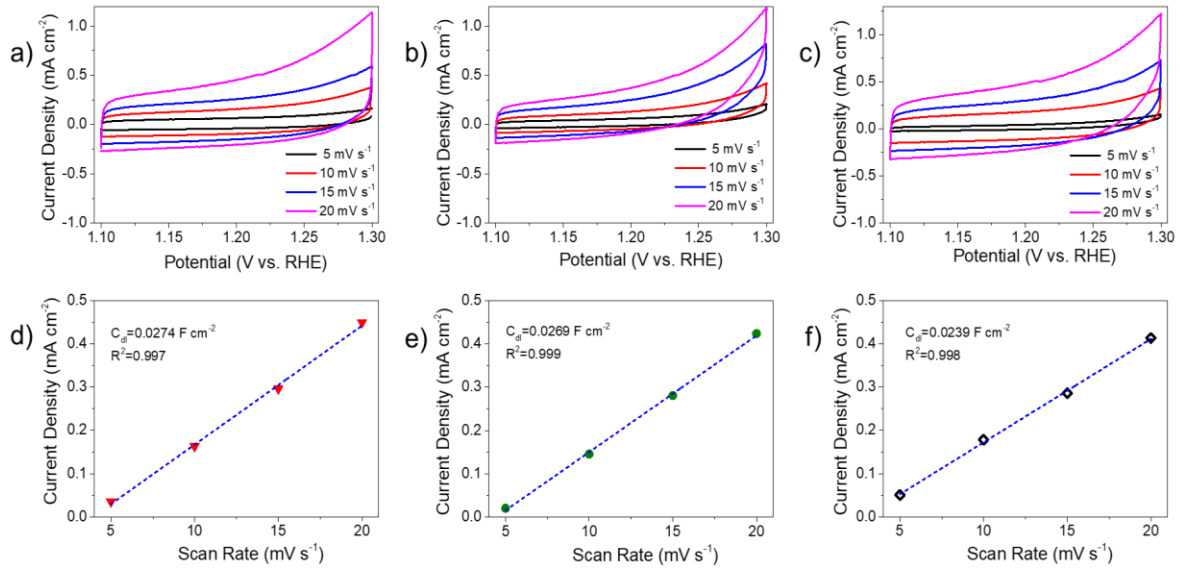

Figure 6.19 CV curves of a) 3DOM-Co@TiO_xN_y, b) 3DOM-Co@TiO_x(Ar) and c) 3DOM-TiON at the double layer region at scan rates of 5, 10, 15 and 20 mV s^{-1} in 1.0 M KOH solution; d-f) current density at the potential of 1.2V, where no redox current peaks are observed, as function of the scan rate derived from a-c), respectively.

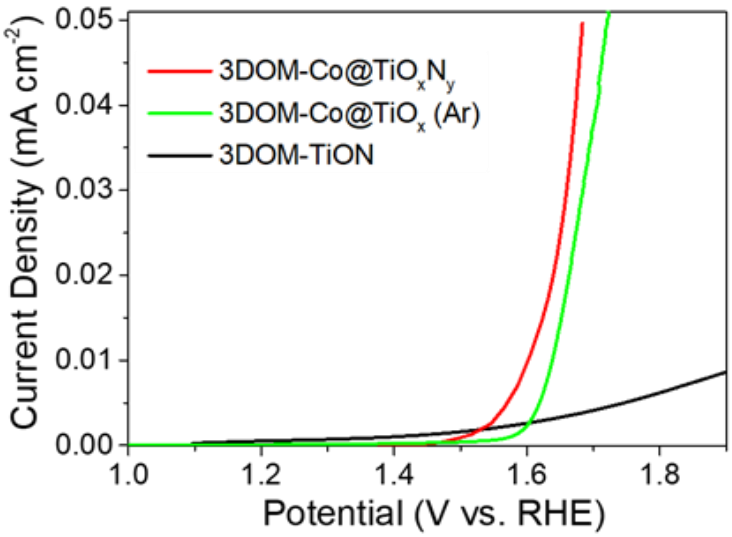

Figure 6.20 LSV curves of various catalysts normalized by electrochemical active surface area.

As mentioned in section 6.2.1, for a comprehensive comparison purpose, three other 3DOM composites, including oxidized 3DOM-Co_3O_4@TiO_2 (air-annealed 3DOM-Co@TiO_xN_y), Co@TiO_xN_y (in NH_3 10min) and Co@TiO_xN_y (in NH_3 1hour) were also synthesized and characterized. Figure 6.21 shows that all the three Co@TiO_xN_y composites treated by NH_3 exhibit higher catalytic activities for both ORR and OER than the oxidized Co_3O_4@TiO_2, indicating the positive effect of N present in the Co@TiO_xN_y catalysts. Moreover, despite all three catalysts having similar ORR activities, the as-prepared 3DOM-Co@Ti_xON_y composite, which obtained by 40min-NH_3 treatment, shows the highest OER activity.

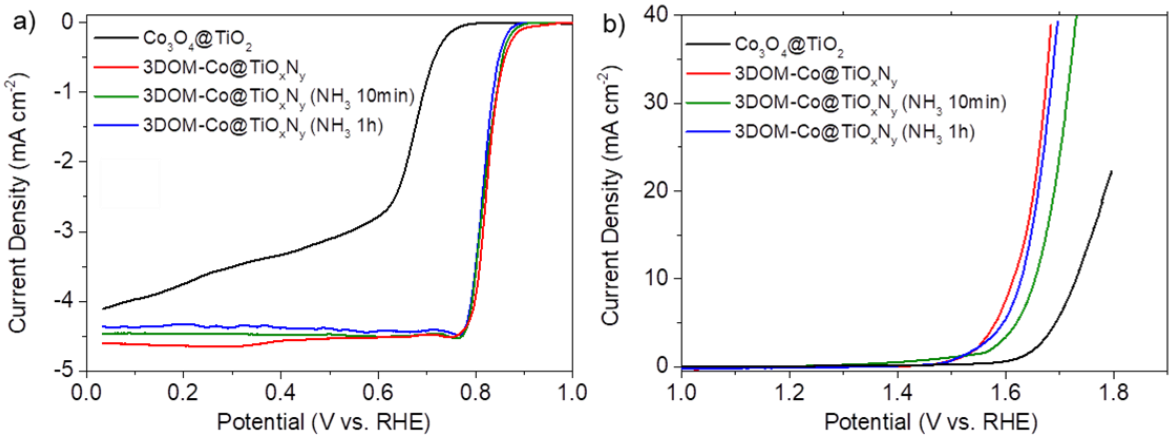

Figure 6.21 a) ORR and b) OER LSV curves of various 3DOM composites obtained at a scan rate of 10 mV s^{-1} in 0.1 M KOH electrolyte at 900 r.p.m and 1600 rpm, respectively.

Furthermore, the stability of the best-performing 3DOM-Co@Ti_xON_y catalyst was examined by performing a CP test at 10mA cm^{-2}. It shows that 3DOM-Co@TiO_xN_y electrode exhibits a much more stable voltage-time curve than Ir/C under OER: its output voltage increased by 5% after 20 h operation, much lower than that of Ir/C (20%), as shown in Figure 6.22a. When fabricated into an air electrode in a rechargeable zinc-air battery, an open circuit voltage of ~1.47 V is achieved (Figure 6.22b). At 1.0 V, the battery delivers a discharge current density of 95 mA cm^{-2} (Figure 6.22c). Notably, at low voltages under 0.8 V, 3DOM-Co@Ti_xON_y was able to deliver a much higher current density than that of Pt/C+Ir/C catalyst mixture, confirming the enhanced mass transfer realized by its 3DOM structure. Additionally, Figure 6.22d shows that it reaches a peak power density of 110 mW cm^{-2} at a current density of 135 mA cm^{-2} (0.80V), higher than that of Pt/C+Ir/C catalyst mixture. The battery stabilities using Pt/C+Ir/C and 3DOM-Co@Ti_xON_y electrodes were further examined at a current density of 20 mA cm^{-2} with each cycle being 20 min. As shown in Figure 6.22e, the zinc-air battery using Pt/C+Ir/C electrode shows a conspicuous charge and discharge voltage decay after 30 cycles (charge-discharge voltage gap of 1.36V) despite the narrow initial voltage gap (0.9V), and the

degradation continues over time.

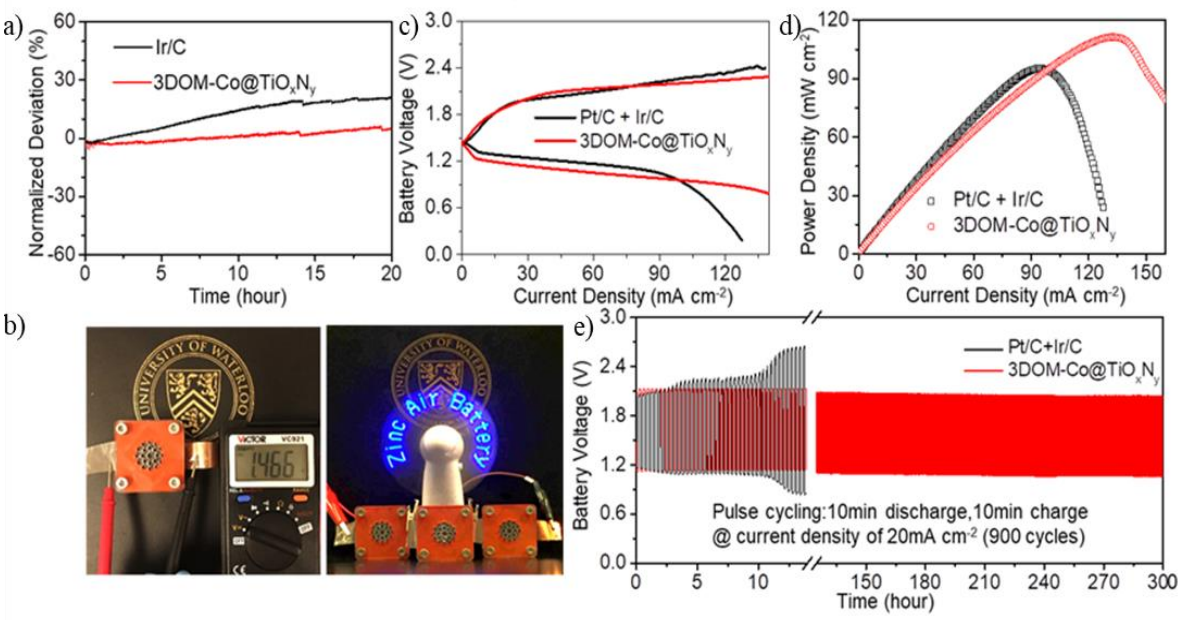

Figure 6.22 a) Long-term OER electrolysis stability under constant current density at 10 mA cm^{-2}; b) Demonstration of the zinc-air battery configuration; c) Charge and discharge polarization curves; d) Power density plots; and e) Cycling performance of zinc-air batteries assembled using 3DOM-Co@TiO_xN_y and Pt/C+Ir/C as air electrodes in ambient air.

Figure 6.23 shows that the battery using 3DOM-Co@Ti_xON_y electrode delivers an initial charge-discharge voltage gap of 0.97V, which was increases only by 10 mV (from 0.97V to 0.98V) after 900 cycles, representing excellent cycling stability with less than 1% energy efficiency loss under highly oxidative operating conditions.

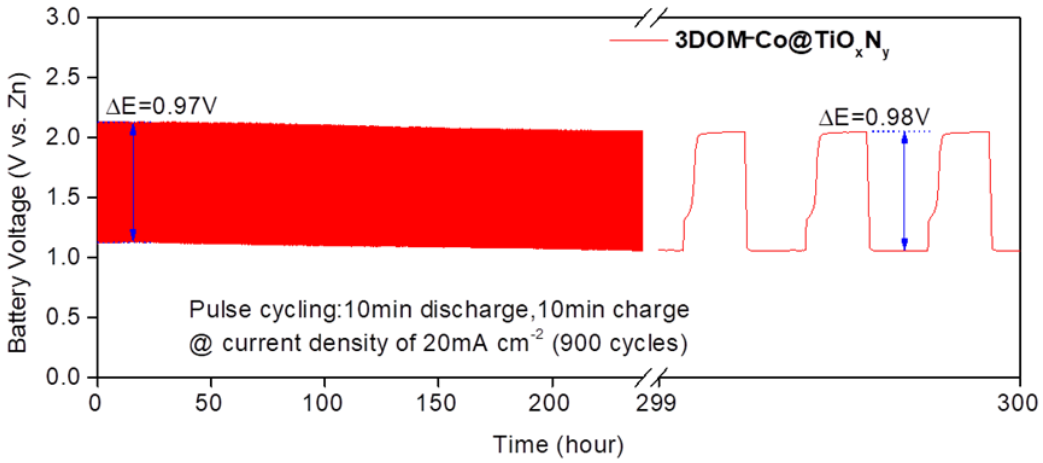

Figure 6.23 Galvanostatic discharge and charge cycling stability of a zinc-air battery using the 3DOM-Co@TiO_xN_y electrode under ambient conditions.

As discussed in our design strategy, the excellent activity and durability of 3DOM-Co@TiO_xN_y are attributed to ultrafine Co and its SMSI with the conductive TiO_xN_y support, respectively. Essentially, the OV in TiO_xN_y support, as well as its 3DOM structure, play the key role. Thus, we expect its OV and structure should be maintained during OER. To verify this argument, the morphology and composition of the 3DOM-Co@TiO_xN_y upon highly oxidative OER operating conditions (at a constant potential of 1.60V vs.RHE) were examined. SEM imaging confirms the 3DOM structure of the composite remained intact after 16 hours of OER testing (Figure 6.24).

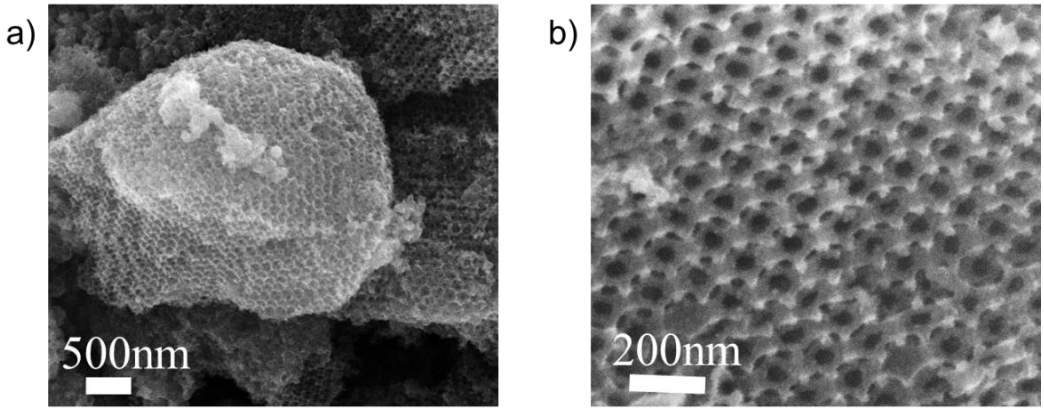

Figure 6.24 a) low and b) high magnification SEM images of the 3DOM-Co@TiO_xN_y composite after 16 hour OER half-cell test at a constant potential of 1.60V (*vs.* RHE).

Interestingly, the XRD pattern shows the TiON and TiO_2 crystalline in 3DOM-Co@TiO_xN_y disappears after OER reaction, exhibiting only TiO crystal patterns (Figure 6.5). Common sense would dictate TiO_xN_y will be eventually oxidized into TiO_2 under OER. Here, we argue that this would be true only in the absence of active OER components. In such cases, the outer surface TiO_xN_y would be "forced" to catalyze OER reaction, and gradually oxidized into TiO_2. In fact, there is only slight oxidation on TiO_xN_y: as shown in the Ti 2p XPS spectrum (Figure 6.11a, after OER), the low energy Ti $2p_{3/2}$ peak associated with TiN or TiO disappears. Meanwhile, the intensity of the TiON peak decreases and the TiO_{2-x} (or Ti_2O_3) peak predominates. There is no obvious increase of the signal at 459.1eV (corresponding to TiO_2), indicating its further oxidation is prohibited.

The mild oxidation of TiO_xN_y surface is also consistent with the decrease of the metallic N-Ti peaks (N-Ti-O and N-Ti) intensity in N 1s spectrum (Figure 6.11c). The oxidation might result from its inevitable involvement in catalyzing OER, see Figure 6.17, from which one can see that the Co-free 3DOM-TiON composite exhibits a minor OER activity. On the other hand, due to its high electrical conductivity, it may receive the electrons released from the active ultrafine Co during OER, and therefore suppresses its further oxidation. The vanishing of TiO_2 crystal structure in XRD is likely caused by the migration of O^{2-} from inner-core TiO_2 lattice towards the OV-rich TiO_xN_y outer surface, as a consequence of the applied positive voltage in OER. In semiconductor physics, such voltage-driven O^{2-} transportation in defective TiO_2 is well-known for resulting in its resistive switching property.[54] Figure 2d shows that the outer CoO surface of the ultrafine Co nanoparticles was oxidized into Co_3O_4 during OER, indicating Co_3O_4

is the actual catalytic phase for OER. As indicated in the O 1s XPS spectrum, after OER reaction, there is a significant increase in the relative intensity of vacancy O^{2-} and O-C peaks (Figure 6.11d). The latter confirms the oxidation of carbon layer during OER, whereas the increased intensity of O^{2-} vacancies might have resulted from the positive voltage-induced O^{2-} migration by extracting O^{2-} from the lattice.[55] Therefore, we conclude that, despite the slight oxidation of the TiO_xN_y surface and carbon layer in the composite, its conductive and OV-rich TiO_{2-x} (or Ti_2O_3) outer surface was preserved during OER. This is the underlying key factor that contributes to the high activity and stability of the composite. Additionally, we found that the chemical state of Co@TiO_xN_y remains almost the same after ORR (Figure 6.25), confirming that the stability of ORR/OER bi-functional catalyst is mainly affected by OER rather than ORR.

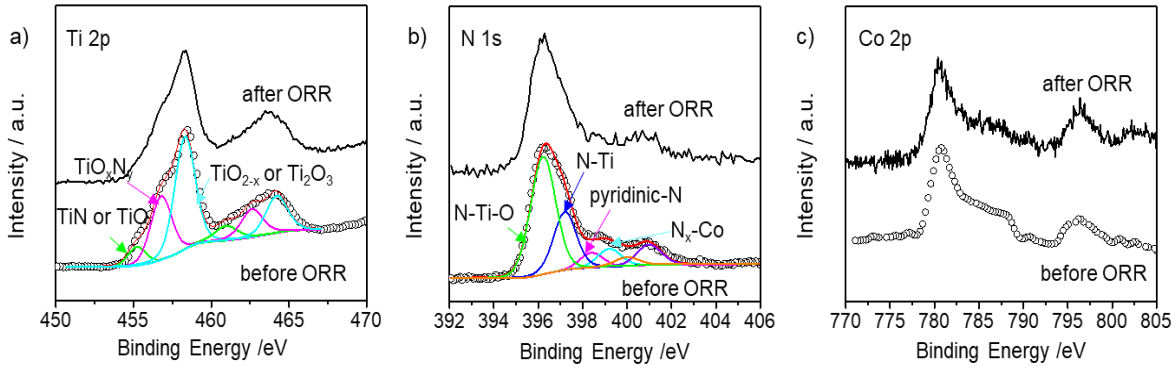

Figure 6.25 a) Ti 2p; b) N 1s; c) Co 2p XPS spectrum of 3DOM-Co@TiO_xN_y before and after 5000 CV cycles of ORR half-cell test.

6.4 Summary

Building on our improved understanding of OVs in semiconductor physics and its resulting SMSI in solid-gas catalysis, we proposed and demonstrated a rational catalyst design strategy of synthesizing 3DOM-TiO_xN_y semiconductor supported ultrafine Co as efficient and durable

electrocatalyst. Benefiting from the OVs-granted features of TiO_xN_y support, including high conductivity, oxidation-resistance, SMSI stabilizing ultrafine Co, the 3DOM-Co@TiO_xN_y composite exhibited comparable ORR-OER performance, but much longer cycling stability than noble-metals in a rechargeable zinc-air battery: it achieved over 900 charge-discharge cycles (300 hours) at 20 mA cm^{-2}. Moreover, we found that the composite undergoes a composition transition during OER. Such transition helps us elucidate the excellent stability of the composite, which is attributed to the sustained OVs and relative low oxidation state of TiO_xN_y surface during OER reaction. The strategy presented in this study can serve as a fundamental basis for selecting and designing high-performance catalyst support materials for oxygen electrocatalysis in rechargeable zinc-air batteries.

CHAPTER 7

Conclusions and Recommendations

7.1 Conclusions

The focus of this research was to develop efficient ORR-OER bifunctional catalysts in zinc-air batteries, and at the same time provide insights on the real OER active phase under its oxidative operating potential. First, an efficient surface engineered (oxidized and nitrogen-doped) cobalt sulfide oxygen electrocatalyst supported on nitrogen-doped reduce graphite oxide sheet (O-N-Co_9S_8@N-RGO) was developed using a surface engineering catalyst design approach. The decorated O-N-Co_9S_8@N-RGO composite shows excellent electrocatalytic activity especially for oxygen evolution reaction (OER), and good stability over 900 charge-discharge cycles (200 hour) at 10 mA cm^{-2} in zinc-air battery. Interestingly, we found that O-N-Co_9S_8 crystal was completely converted into Co_3O_4 after OER. As there are increasingly many reports that claim metal chalcogenides, especially metal sulfides, as efficient OER catalysts for alkaline water electrolysis and rechargeable zinc-air batteries, our observations further clarify that oxide is the actual OER active phase rather than sulfide. Moreover, with such knowledge, our study suggests, and experimentally demonstrates that metal oxides, e.g. Co_3O_4, *in-situ* generated from phase transition of metal chalcogenides or metal oxides during OER, should be more active than the oxides crystals synthesized from calcination. This study advances the fundamental insight of metal chalcogenides-based OER "catalysts", of which the post-OER characterizations of the as-prepared bifunctional catalyst should be considered to identify its real active phase. It also provides guidance for the design of active OER catalysts.

The surface engineered Co_9S_8 catalysts was further investigated by designing it into a self-supported 3DOM structured catalyst. The resulting 3DOM N-Co_9S_8@NC catalyst provides a 3D through-continuity for maximum accessibility of the active phases to reactants. Such 3DOM structure design also minimizes the likelihood of N-Co_9S_8 nanoparticles agglomeration, which is highly possible to occur in N-RGO supported O-N-Co_9S_8@N-RGO catalysts. As a result, the zinc-air battery using the 3DOM N-Co_9S_8@NC catalyst delivers outstanding charge and discharge performance, and long cycling stability over 400 h at 10 mA cm^{-2} is achieved. The results suggest that 3DOM self-support porous structure design is an effective strategy to improve the oxygen catalytic activity and cycling durability of transition metal-based bi-functional catalysts. It is also worth to know that the partial structure crush of N-Co_9S_8 after long-time OER testing implies that chalcogenide compounds might not suitable for the design of structurally robust bi-functional catalyst.

Finally, as an attempt to permanently solve the corrosion of bifunctional oxygen catalysts caused by the highly oxidative operating condition of rechargeable zinc-air batteries, based on our up-to-date multidisciplinary understanding of oxygen vacancies (OVs) in semiconductor physics and solid-gas catalysis, we propose a different strategy for the catalyst support design focusing on OVs-rich, low-bandgap semiconductor. The OVs promote the electrical conductivity of oxide support, and at the same time offer a strong metal-support interaction (SMSI), which gives small metal size, high catalytic activity, and stability. To the authors' knowledge, this is the first time that such concept is introduced to design active and stable non-precious bifunctional electrocatalysts. This strategy is demonstrated by successfully synthesizing ultrafine Co metal catalyst decorated three-dimensionally ordered macroporous titanium oxynitride (3DOM-Co@TiO_xN_y). The SMSI is verified by density functional theory calculations. The resulting

3DOM-Co@TiO_xN_y composite exhibits comparable oxygen electrocatalytic activity and much longer cycling stability than noble metal-based catalysts in alkaline conditions. The zinc-air battery using this catalyst delivers an excellent stability over 900 charge-discharge cycles at 20 mA cm^{-2}, with 99.5% energy efficiency retention. This work opens a new perspective to use OVs-rich semiconductors as promising support to design efficient and durable non-precious oxygen electrocatalysts for metal-air batteries. This study would be of substantial practical as well as fundamental interest to global research efforts in oxygen electrocatalysis and metal-air battery communities.

7.2 Recommendations

This research represents a promising step towards a rational design and development of efficient ORR-OER bifunctional catalysts in zinc-air batteries. It also provides a clear understanding of the real OER catalytic component in Co-based catalysts. However, there are still many challenges ahead for the development of novel oxygen electrocatalysts. The following are recommendations for future research:

i) The real catalytic phase of OER

Even though we have observed the conversion of cobalt sulfide into cobalt oxide during OER, but this is obtained under the operating potential of 1.60V *vs.* RHE. As discussed in Section 2.5 of Chapter 2, recently, there are studies reported that there exists a dynamic transformation between cobalt oxides and hydr-oxides at different OER working potentials. Thus, we think that the real catalytic phase of cobalt-based oxygen electrocatalysts is correlated with the potentials, which should be investigated in the future. Such study will provide a more comprehensive understanding of the OER catalysis process and guides the rational design of efficient bi-

functional catalysts in zinc-air batteries.

ii) The synergistic effects between Co-M (M=Fe, Ni) on ORR-OER activity

The present study has shown that 3DOM TiO_xN_y semiconductor catalyst support design is an effective strategy to develop efficient and stable bifunctional catalysts. However, only Co is used as the active component. As there are increasing more reports observing improved ORR-OER performance of Co-Fe, Co-Ni based oxygen electrocatalysts. The introduction of other transition metals, e.g. Fe, Ni, into the as-developed 3DOM-Co@TiO_xN_y composite to further enhance its ORR-OER activity and its synergistic effects would be interesting.

iii) The exploration of high-performance semiconductor supports in bi-functional catalysts

The current study has only focused on the TiO_xN_y semiconductor support design on the development of efficient and oxidation resistive ORR-OER catalysts. In fact, in addition to TiO_x-based material, there are many semiconductors that worthy to be searched and explored in oxgen eletrocatalysis.

Publications

1. **Guihua Liu**, Jingde Li, Jing Fu, Gaopeng Jiang, Gregory Lui, Dan Luo, Ya-Ping Deng, Jing Zhang, Zachary P. Cano, Aiping Yu, Dong Su, Zhengyu Bai, Lin Yang, Zhongwei Chen*. An oxygen-vacancy-rich semiconductor-supported bifunctional catalyst for efficient and stable zinc-air batteries. Advanced Materials, 2019, 31, 1806761

2. Jingde Li[1], **Guihua Liu[1]**, Jing Fu, Jing Zhang, Gaopeng Jiang, Fathy M Hassan, Luis Ricardez-Sandoval, Zhongwei Chen*. Surface decorated cobalt sulfide as efficient catalyst for oxygen evolution reaction and its intrinsic activity, Journal of Catalysis, 2018, 367, 43-52.

3. Jing Fu, Ruiling Liang, **Guihua Liu**, Aiping Yu, Zhengyu Bai, Lin Yang, Zhongwei Chen*. Recent progress in electrically rechargeable zinc-air batteries. Advanced Materials, 2018, 1805230.

4. **Guihua Liu**, Jing Fu, Dan Luo, Ya-Ping Deng, Jing Zhang, Jingde Li, Aiping Yu, Zhongwei Chen* Self-supported vacancy-rich cobalt sulfide as efficient bifunctional catalyst for zinc-air batteries. In Preparation

5. Gaopeng Jiang, Maciej Goledzinowski, Felix J. E. Comeau, Hadis Zarrin, Gregory Lui, Jared Lenos, Alicia Veileux, **Guihua Liu**, Jing Zhang, Sahar Hemmati, Jinli Qiao, Zhongwei Chen*. Free-standing functionalized graphene oxide solid electrolytes in electrochemical gas sensors. Advanced Functional Materials, 2016, 26, 1729-1736.

Copyright Permissions

Copyright Clearance Center RightsLink®

Home | Account Info | Help

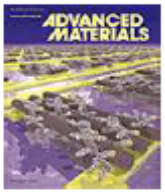

Title:	An Oxygen-Vacancy-Rich Semiconductor-Supported Bifunctional Catalyst for Efficient and Stable Zinc–Air Batteries
Author:	Guihua Liu, Jingde Li, Jing Fu, et al
Publication:	Advanced Materials
Publisher:	John Wiley and Sons
Date:	Dec 9, 2018

Logged in as:
Guihua Liu
LOGOUT

Order Completed

Thank you for your order.

This Agreement between Mrs. Guihua Liu ("You") and John Wiley and Sons ("John Wiley and Sons") consists of your license details and the terms and conditions provided by John Wiley and Sons and Copyright Clearance Center.

Your confirmation email will contain your order number for future reference.

printable details

License Number	4544181289959
License date	Mar 08, 2019
Licensed Content Publisher	John Wiley and Sons
Licensed Content Publication	Advanced Materials
Licensed Content Title	An Oxygen-Vacancy-Rich Semiconductor-Supported Bifunctional Catalyst for Efficient and Stable Zinc–Air Batteries
Licensed Content Author	Guihua Liu, Jingde Li, Jing Fu, et al
Licensed Content Date	Dec 9, 2018
Licensed Content Volume	31
Licensed Content Issue	6
Licensed Content Pages	7
Type of use	Dissertation/Thesis
Requestor type	Author of this Wiley article
Format	Print and electronic
Portion	Full article
Will you be translating?	No
Title of your thesis / dissertation	Design of Efficient Cobalt-based Bi-functional Catalysts for Zinc-Air Batteries
Expected completion date	Apr 2019
Expected size (number of pages)	160
Requestor Location	Mrs, Guihua Liu E6-2118 200 University Ave, W Waterloo, ON N2L 3G1 Canada Attn: Mrs. Guihua Liu

Publisher Tax ID	EU826007151
Total	0.00 CAD

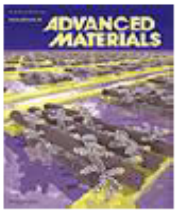

Title:	Recent Progress in Electrically Rechargeable Zinc–Air Batteries
Author:	Jing Fu, Ruilin Liang, Guihua Liu, et al
Publication:	Advanced Materials
Publisher:	John Wiley and Sons
Date:	Dec 9, 2018

Order Completed

Thank you for your order.

This Agreement between Mrs. Guihua Liu ("You") and John Wiley and Sons ("John Wiley and Sons") consists of your license details and the terms and conditions provided by John Wiley and Sons and Copyright Clearance Center.

Your confirmation email will contain your order number for future reference.

printable details

License Number	4544191057951
License date	Mar 08, 2019
Licensed Content Publisher	John Wiley and Sons
Licensed Content Publication	Advanced Materials
Licensed Content Title	Recent Progress in Electrically Rechargeable Zinc–Air Batteries
Licensed Content Author	Jing Fu, Ruilin Liang, Guihua Liu, et al
Licensed Content Date	Dec 9, 2018
Licensed Content Volume	0
Licensed Content Issue	0
Licensed Content Pages	13
Type of use	Dissertation/Thesis
Requestor type	Author of this Wiley article
Format	Print and electronic
Portion	Text extract
Number of Pages	5
Will you be translating?	No
Title of your thesis / dissertation	Design of Efficient Cobalt-based Bi-functional Catalysts for Zinc-Air Batteries
Expected completion date	Apr 2019
Expected size (number of pages)	160
Requestor Location	Mrs. Guihua Liu E6-2118 200 University Ave. W Waterloo, ON N2L 3G1 Canada Attn: Mrs. Guihua Liu
Publisher Tax ID	EU826007151

Total	0.00 CAD

Reference

Chapter 1

[1] J. Pan, Y. Y. Xu, H. Yang, Z. Dong, H. Liu, B.Y. Xia, Advanced Architectures and Relatives of Air Electrodes in Zn–Air Batteries, *Adv. Sci. 2018*, 5, 1700691.

[2] K. Sasaki, H. Naohara, Y. Cai, Y. M. Choi, P. Liu, M. B. Vukmirovic, J.X. Wang, R. R. Adzic, Core-Protected Platinum Monolayer Shell High-Stability Electrocatalysts for Fuel-Cell Cathodes, *Angew. Chem. Int. Ed.2010*,49, 8602 –8607.

[3] N. Danilovic, R. Subbaraman, K.C. Chang, S.H. Chang, Y. Kang, J. Snyder, A. P. Paulikas, D. Strmcnik, Y. T. Kim, D. Myers, V.R. Stamenkovic, N.M. Markovic, Using surface segregation to design stable Ru-Ir oxides for the oxygen evolution reaction in acidic environments, *Angew. Chem. Int. Ed. 2014*,53, 14016 –14021.

[4] E. Davari, D. G. Ivey, Bifunctional electrocatalysts for Zn–air batteries, *Sustainable Energy Fuels*, *2018*, 2, 39–67.

[5] J. Fu, F. M. Hassan, C. Zhong, J. Lu, H. Liu, A. Yu, Z. Chen, Defect engineering of chalcogen-tailored oxygen electrocatalysts for rechargeable quasi-solid-state zinc-air batteries, *Adv. Mater. 2017*, 1702526 1-9.

[6] M. Shen, C. Ruan, Y. Chen, C. Jiang, K. Ai, L. Lu, Covalent entrapment of cobalt–iron sulfides in N-doped mesoporous carbon: Extraordinary bifunctional electrocatalysts for oxygen reduction and evolution reactions, *ACS Appl. Mater. Interfaces, 2015*, 7, 1207-1218.

[7] B. Seo, Y. J. Sa, J. Woo, K. Kwon, J. Park, T. J. Shin, H. Y. Jeong, S. H. Joo, Size-dependent activity trends combined with in situ X-ray absorption spectroscopy reveal insights into cobalt oxide/carbon nanotube-catalyzed bifunctional oxygen electrocatalysis. *ACS Catal., 2016,* 6, 4347-4355.

[9] Z. Zhao, M. Li, L. Zhang, L. Dai, Z. Xia, Design principles for heteroatom-doped carbon nanomaterials as highly efficient catalysts for fuel cells and metal-air batteries, *Adv. Mater. 2015*, 27, 6834–6840.

[10] M. Lefèvre, E. Proietti, F. Jaouen, J.P. Dodelet, Iron-based catalysts with improved oxygen reduction activity in polymer electrolyte fuel cells, *Science, 2009,* 324, 71-74.

[11] L. Yu, X. Pan, X. Cao, P. Hu, X. Bao, Oxygen reduction reaction mechanism on nitrogen-

doped graphene: A density functional theory study, *Journal of Catalysis, 2011,* 282, 183–190

[12] H. Y. Zhao, C. H. Sun, Z. Jin, D. W. Wang, X. C. Yan, Z. G. Chen, G. S. Zhu, X. D. Yao, Carbon for the oxygen reduction reaction: a defect mechanism, *J. Mater. Chem., A,* 2015, 3, 11736.

[13] Y. Jia, L. Zhang, A. Du, G. Gao, J. Chen, X. Yan, C. L. Brown, X. Yao, Defect graphene as a trifunctional catalyst for electrochemical reactions, *Adv. Mater. 2016,* 28, 9532–9538.

[14] L. Wang, A. Ambrosi, M. Pumera, "Metal-Free" catalytic oxygen reduction reaction on heteroatom-doped graphene is caused by trace metal impurities, *Angew. Chem. Int. Ed. 2013,* 52, 13818–13821

[15] H. T. Chung, D. A. Cullen, D. Higgins, B. T. Sneed, E. F. Holby, K. L. More, P. Zelenay, Direct atomic-level insight into the active sites of a high-performance PGM-free ORR catalyst, *Science, 2017,* 357, 479–484.

[16] Q. Wang, L. Shang, R. Shi, X. Zhang, G.I.N. Waterhousec, L-Z. Wu, C-H. Tung, T. Zhang, 3D carbon nanoframe scaffold-immobilized Ni_3FeN nanoparticle electrocatalysts for rechargeable zinc-air batteries' cathodes, *Nano Energy, 2017,* 40, 382–389.

[17] Jinfa Chang, Yao Xiao, Meiling Xiao, Junjie Ge, Changpeng Liu, Wei Xing, Surface oxidized cobalt-phosphide nanorods as an advanced oxygen evolution catalyst in alkaline solution, *ACS Catal., 2015,* 5, 6874–6878.

[18] Jungang Hou, Bo Zhang, Zhuwei Li, Shuyan Cao, Yiqing Sun, Yunzhen Wu, Zhanming Gao, Licheng Sun, Vertically aligned oxygenated-CoS_2-MoS_2 heteronanosheet architecture from polyoxometalate for efficient and stable overall water splitting, *ACS Catal., 2018,* 8, 4612–4621.

[19] W.Li, X. Gao, D. Xiong, F. Wei, W. Song, J. Xu, L. Liu, Hydrothermal synthesis of monolithic Co_3Se_4 nanowire electrodes for oxygen evolution and overall water splitting with high efficiency and extraordinary catalytic stability, *Adv. Energy Mater., 2017,* 7, 1602579.

[20] Chauhan, M.; Reddy, K. P.; Gopinath, C. S.; Deka, S. Copper Cobalt Sulfide Nanosheets Realizing a Promising Electrocatalytic Oxygen Evolution Reaction, ACS Catal. **2017**, 7, 5871-5879.

[21] J. Wang, W. Cui, Q. Liu, Z. Xing, A. M. Asiri, X. Sun, Recent progress in cobalt-based heterogeneous catalysts for electrochemical water splitting, *Adv. Mater. 2016,* 28, 215-230

[22] G-F. Chen, T. Y. Ma, Z-Q. Liu, N. Li, Y-Z. Su, K. Davey, S-Z. Qiao, Efficient and stable bifunctional electrocatalysts Ni/Ni_xM_y (M = P, S) for overall water splitting, *Adv. Funct. Mater.*

2016, 26, 3314-3323

[23] X. Han, F. Cheng, T. Zhang, J. Yang, Y. Hu, J. Chen, Hydrogenated uniform Pt clusters supported on porous $CaMnO_3$ as a bifunctional electrocatalyst for enhanced oxygen reduction and evolution, *Adv. Mater. 2014,* 26, 2047–2051

[24] L. Li, C. Liu, G. He, D. Fan, A. Manthiram, Hierarchical pore-in-pore and wire-in-wire catalysts for rechargeable Zn– and Li-air batteries with ultra-long cycle life and high cell efficiency, *Energy Environ. Sci., 2015,* 8, 3274—3282

[25] J.C. Li, P.X. Hou, S.Y. Zhao, C. Liu, D.M. Tang, M. Cheng, F. Zhang, H, M. Cheng, A 3D bi-functional porous N-doped carbon microtube sponge electrocatalyst for oxygen reduction and oxygen evolution reactions, *Energy Environ. Sci., 2016,* 9, 3079-3084

[26] Dutta, A.; Samantara, A. K.; Dutta, S. K.; Jena, B. K.; Pradhan, N. Surface-Oxidized Dicobalt Phosphide Nanoneedles as a Nonprecious, Durable, and Efficient OER Catalyst. *ACS Energy Lett. 2016,* 1, 169−174.

[27] S. Jin, Are Metal Chalcogenides, Nitrides, and Phosphides Oxygen Evolution Catalysts or Bifunctional Catalysts? *ACS Energy Lett. 2017,* 2, 1937−1938

[28] F.S. Saleh, E. B. Easton, Diagnosing degradation within PEM fuel cell catalyst layers using electrochemical impedance spectroscopy, *J. Electrochem. Soc. 2012,* 159, B546;

[29] C. Spoeri, J. T. H. Kwan, A. Bonakdarpour, D. P. Wilkinson, P. Strasser, The stability challenges of oxygen evolving catalysts: towards a common fundamental understanding and mitigation of catalyst degradation, *Angew. Chem. Int. Ed. 2017,* 56, 5994.

[30] N. G. Akalework, C.J. Pan, W.N. Su, J. Rick, M.C. Tsai, J.F. Lee, J.M. Lin, L.D. Tsai, B.J. Hwang, Ultrathin TiO_2-coated MWCNTs with excellent conductivity and SMSI nature as Pt catalyst support for oxygen reduction reaction in PEMFCs, *J. Mater. Chem., 2012,* 22, 20977-20985

[31] G. Zhao, R. Mo, B. Wang, L. Zhang, K. Sun, Enhanced cyclability of $Li–O_2$ batteries based on TiO_2 supported cathodes with no carbon or binder, *Chem. Mater., 2014,* 26, 2551–2556.

[32] X. Xu, C. Su, W. Zhou, Y. Zhu, Y. Chen, Z. Shao, Co-doping Strategy for Developing Perovskite Oxides as Highly Efficient Electrocatalysts for Oxygen Evolution Reaction, *Adv. Sci. 2016,* 3, 1500187

Chapter 2

[1] Z. P. Cano, D. Banham, S. Ye, A. Hintennach, J. Lu, M. Fowler, Z. Chen, Batteries and fuel cells for emerging electric vehicle markets, *Nat. Energy., 2018,* 3, 279–289.

[2] Q. Wang, P. Ping, X. Zhao, G. Chu, J. Sun, C. Chen, Thermal runaway caused fire and explosion of lithium ion battery, *J. Power Sources, 2012,* 208, 210–224.

[3] S. G. Chalk, J. F. Miller, Key challenges and recent progress in batteries, fuel cells, and hydrogen storage for clean energy systems, *J. Power Sources, 2006,* 159, 73–80.

[4] Y. Li, H. Dai, Recent advances in zinc–air batteries, *Chem. Soc. Rev., 2014,* 43, 5257-5275

[5] J. Fu, F. M. Hassan, C. Zhong, J. Lu, H. Liu, A. Yu, Z. Chen. Defect Engineering of Chalcogen-Tailored Oxygen Electrocatalysts for Rechargeable Quasi-Solid-State Zinc–Air Batteries, Adv. *Mater. 2017,* 29, 1702526.

[6] https://en.wikipedia.org/wiki/Zinc%E2%80%93air_battery.

[7] K. E. K. Sun, T. K. A. Hoang, T. N. L. Doan, Y. Yu, X. Zhu, Y. Tian, P. Chen, Suppression of dendrite formation and corrosion on zinc anode of secondary aqueous batteries, *ACS Appl. Mater. Interfaces, 2017,* 9, 9681–9687.

[8] F. Wan, L. Zhang, X. Dai, X. Wang, Z. Niu, J. Chen, Aqueous rechargeable zinc/sodium vanadate batteries with enhanced performance from simultaneous insertion of dual carriers, *Nat. Commun., 2018,* 9, 1656.

[9] X. Liu, L. Wang, P. Yu, C. Tian, F. Sun, J. Ma, W. Li, H. Fu, A Stable Bifunctional Catalyst for Rechargeable Zinc-Air Batteries: Iron–Cobalt Nanoparticles Embedded in a Nitrogen-Doped 3D Carbon Matrix, *Angew. Chem. Int. Ed., 2018,* 130, 16398-16402.

[10] N. Xu, J. Qiao, Q. Nie, M. Wang, H. Xu, Y. Wang, X-D. Zhou, $CoFe_2O_4$ nanoparticles decorated carbon nanotubes: Air-cathode bifunctional catalysts for rechargeable zinc-air batteries, *Catal. Today, 2018,* 318, 144-149.

[11] C. Si, Y. Zhang, C. Zhang, H. Gao, W. Ma, L. Lv, Z. Zhang, Mesoporous nanostructured spinel-type MFe_2O_4 (M = Co, Mn, Ni) oxides as efficient bi-functional electrocatalysts towards oxygen reduction and oxygen evolution, *Electrochim. Acta, 2017,* 245, 829-838.

[12] B. K. Barman, K. K. Nanda, Prussian blue as a single precursor for synthesis of Fe/Fe_3C encapsulated N-doped graphitic nanostructures as bi-functional catalysts, *Green Chem., 2016,* 18, 427-432.

[13] Y-J. Wang, W. Long, L. Wang, R. Yuan, A. Ignaszak, B. Fang, D. P. Wilkinson, Unlocking the door to highly active ORR catalysts for PEMFC applications: polyhedron-engineered Pt-based nanocrystals, *Energy Environ. Sci., 2018,* 11, 258-275.

[14] M. Escudero-Escribano, Pa. Malacrida, M. H. Hansen, U. G. Vej-Hansen1, A. Velázquez-Palenzuela1, V. Tripkovic, J. Schiøtz, J. Rossmeisl, I. E. L. Stephens, Ib Chorkendorff, Tuning the activity of Pt alloy electrocatalysts by means of the lanthanide contraction, *Science, 2016,* 352, 73-76.

[15] M. Liu, Z. Zhao, X. Duan, Y. Huang, Nanoscale Structure Design for High-Performance Pt-Based ORR Catalysts, *Adv. Mater. 2019,* 31, 1802234.

[16] J. Shan, C. Guo, Y. Zhu, S. Chen, L. Song, M. Jaroniec, Y. Zheng, S-Z. Qiao, Charge-Redistribution-Enhanced Nanocrystalline Ru@ IrOx Electrocatalysts for Oxygen Evolution in *Acidic Media, Chem., 2019,* 5, 445-459.

[17] J. Ding, P. Wang, S. Ji, H. Wang, V. Linkov, R. Wang, N-doped mesoporous FeN_x/carbon as ORR and OER bifunctional electrocatalyst for rechargeable zinc-air batteries, *Electrochim. Acta, 2019,* 296, 653-661.

[18] S.W. Kim, Y. Son, K. Choi, S. I. Kim, Y. Son, J. Park, J. H. Lee, J.H. Jang, Highly Active Bifunctional Electrocatalysts for Oxygen Evolution and Reduction in Zn–Air Batteries, *Chem SusChem, 2018,* 11, 4203 –4208.

[19] Y. Liu, H. Jiang, Y. Zhu, X. Yang, C. Li, Transition metals (Fe, Co, and Ni) encapsulated in nitrogen-doped carbon nanotubes as bi-functional catalysts for oxygen electrode reactions, *J. Mater. Chem. A, 2016,* 4, 1694-1701.

[20] W. Wang, J. Luo, S. Chen, Carbon oxidation reactions could misguide the evaluation of carbon black-based oxygen-evolution electrocatalysts, *Chem. Commun., 2017,* 53, 11556-11559.

[21] A. Puapattanakula, S. Therdthianwongb, A. Therdthianwongc, N. Wongyao, Improvement of Zinc-Air Fuel Cell Performance by Gelled KOH, *Energy Procedia, 2013,* 34, 173-180.

[22] Z. X. Liu, Z. P. Li, H.Y. Qin, B. H. Liu, Oxygen reduction reaction via the 4-electron transfer pathway on transition metal hydroxides, *J. Power Sources, 2011,* 196, 4972–4979.

[23] H. Arnolds, Femtosecond laser-induced reactions with O_2 on Pt {111}, *Surf. Sci., 2004,* 548, 151-156.

[24] L. Ai, Z. Niu, J. Jiang, Mechanistic insight into oxygen evolution electrocatalysis of surface phosphate modified cobalt phosphide nanorod bundles and their superior performance for overall

water splitting, *Electrochim. Acta, 2017,* 242,355–363.

[25] H. Osgood, S. V. Devaguptapu, H. Xu, J. Cho, G. Wu, Transition metal (Fe, Co, Ni, and Mn) oxides for oxygen reduction and evolution bifunctional catalysts in alkaline media, *Nano Today, 2016,* 11, 601.

[26] Y. Bu, O. Gwon, G. Nam, H. Jang, S. Kim, Q. Zhong, J. Cho, G. Kim, A highly efficient and robust cation ordered perovskite oxide as a bifunctional catalyst for rechargeable zinc-air batteries, *ACS Nano, 2017,* 11, 11594–11601.

[27] T. Ishihara, L. M. Guo, T. Miyano, Y. Inoishi, K. Kaneko, S. Ida, Mesoporous $La_{0.6}Ca_{0.4}CoO_3$ perovskites with large surface areas as stable air electrodes for rechargeable Zn–air batteries, *J. Mater. Chem. A, 2018,* 6, 7686-7692.

[28] D.U. Lee, Ji. Li, M. G. Park, M. H. Seo, W. Ahn, I. Stadelmann, L. Ricardez-Sandoval, Z. Chen, Self-Assembly of Spinel Nanocrystals into Mesoporous Spheres as Bifunctionally Active Oxygen Reduction and Evolution Electrocatalysts, *ChemSusChem, 2017,* 10, 2258 – 2266.

[29] J-I. Jung, M. Risch, S. Park, M. G. Kim, G. Nam, H-Y. Jeong, Y. Shao-Horn, J. Cho, Optimizing nanoparticle perovskite for bifunctional oxygen electrocatalysis, *Energy Environ. Sci., 2016,* 9, 176-183.

[30] T. Ishihara, K. Yokoe, T. Miyano, H. Kusaba, Mesoporous $MnCo_2O_4$ spinel oxide for a highly active and stable air electrode for Zn-air rechargeable battery, *Electrochim. Acta, 2019,* 300, 455-460.

[31] E. Davari, D. G. Ivey, Bifunctional electrocatalysts for Zn–air batteries, *Sustainable Energy Fuels, 2018,* 2, 39–67.

[32] Y-J. Wang, H. Fan, A. Ignaszak, L. Zhang, S. Shao, D. P. Wilkinson, J. Zhang, Compositing doped-carbon with metals, non-metals, metal oxides, metal nitrides and other materials to form bi-functional electrocatalysts to enhance metal-air battery oxygen reduction and evolution reactions, *Chem. Eng. Sci., 2018,* 348, 416–437.

[33] Y. Li, C. Zhong, J. Liu, X. Zeng, S. Qu, X. Han, Y. Deng, W. Hu, J. Lu, Atomically Thin Mesoporous Co_3O_4 Layers Strongly Coupled with N-rGO Nanosheets as High-Performance Bifunctional Catalysts for 1D Knittable Zinc-Air Batteries, *Adv. Mater., 2018,* 30, 1703657.

[34] S. Zeng, H. Chen, H. Wang, X. Tong, M. Chen, J. Di, Q. Li, Crosslinked Carbon Nanotube Aerogel Films Decorated with Cobalt Oxides for Flexible Rechargeable Zn–Air Batteries, *Small, 2017,* 13,1700518.

[35] Z. Li, M. Shao, Q. Yang, Y. Tang, M. Wei, D. G. Evans, X. Duan, Directed synthesis of carbon nanotube arrays based on layered double hydroxides toward highly-efficient bifunctional oxygen electrocatalysis, *Nano Energy, 2017,* 37, 98-107.

[36] X. Han, X. Wu, C. Zhong, Y. Deng, N. Zhao, W. Hu, $NiCo_2S_4$ nanocrystals anchored on nitrogen-doped carbon nanotubes as a highly efficient bifunctional electrocatalyst for rechargeable zinc-air batteries, *Nano Energy, 2017,* 31, 541–550.

[37] L. Qian, Z. Lu, T. Xu, X. Wu, Y. Tian, Y. Li, Z. Huo, X. Sun, X. Duan, Trinary layered double hydroxides as high-performance bifunctional materials for oxygen electrocatalysis, *Adv. Energy Mater. 2015,* 5, 1500245.

[38] Q. Wang, L. Shang, R. Shi, X. Zhang, Y. Zhao, G. I. N. Waterhouse, L-Z. Wu, C-H. Tung, T. Zhang, NiFe Layered Double Hydroxide Nanoparticles on Co, N-Codoped Carbon Nanoframes as Efficient Bifunctional Catalysts for Rechargeable Zinc-Air Batteries, *Adv. Energy Mater., 2017,* 7, 1700467.

[39] Y. Li, W. Zhou, J. Dong, Y. Luo, P. An, J. Liu, X. Wu, G. Xu, H. Zhang, J. Zhang, Interface engineered in situ anchoring of Co_9S_8 nanoparticles into a multiple doped carbon matrix: highly efficient zinc–air batteries, *Nanoscale, 2018,* 10, 2649-2657.

[40] S. Jin, Are metal chalcogenides, nitrides, and phosphides oxygen evolution catalysts or bifunctional catalysts? *ACS Energy Lett., 2017,* 2, 1937−1938.

[41] J. Hou, B. Zhang, Z. Li, S. Cao, Y. Sun, Y. Wu, Z. Gao, L. Sun, Vertically aligned oxygenated-CoS_2-MoS_2 heteronanosheet architecture from polyoxometalate for efficient and stable overall water splitting, *ACS Catal., 2018,* 8, 4612–4621.

[42] X. Su, Y. Wang, J. Zhou, S. Gu, J. Li, S. Zhang, Operando spectroscopic identification of active sites in NiFe prussian blue analogues as electrocatalysts: Activation of oxygen atoms for oxygen evolution reaction, *J. Am. Chem. Soc., 2018,* 140, 11286−11292.

[43] M. Favaro, J. Yang, S. Nappini, E. Magnano, F. M. Toma, E. J. Crumlin, J. Yano, I.D. Sharp, Understanding the oxygen evolution reaction mechanism on CoO_x using operando ambient-pressure X-ray photoelectron spectroscopy, *J. Am. Chem. Soc., 2017,* 139, 8960–8970.

[44] J. Ryu, N. Jung, J. H. Jang, H-J. Kim, S. J. Yoo, In situ transformation of hydrogen-evolving CoP nanoparticles: toward efficient oxygen evolution catalysts bearing dispersed morphologies with Co-oxo/hydroxo molecular units, *ACS Catal., 2015,* 5, 4066−4074.

[45] X. Xu, F. Song, X. Hu, A nickel iron diselenide-derived efficient oxygen-evolution catalyst,

Nature Commun., 2016, 7, 12324.

[46] J. Fester, A. Makoveev, D. Grumelli, R. Gutzler, Z. Sun, J. Rodr&guez-Fernandez, K. Kern, J. V. Lauritsen, The structure of the cobalt oxide/Au catalyst interface in electrochemical water splitting, *Angew. Chem. Int. Ed. 2018,* 57, 11893−11897.

[47] Z. Chen, L. Cai, X. Yang, C. Kronawitter, L. Guo, S. Shen, B. E. Koel, Reversible structural evolution of $NiCoO_xH_y$ during the oxygen evolution reaction and identification of catalytically active phase, *ACS Catal., 2018,* 8, 1238−1247.

[48] J. Zhang, Z. Zhao, Z. Xia, L. Dai, A metal-free bifunctional electrocatalyst for oxygen reduction and oxygen evolution reactions, *Nature Nanotechnol., 2015,* 10, 444–452.

[49] G-L. Chai, K. Qiu, M, Qiao, M-M. Titirici, C. Shang, Z. Guo, Active sites engineering leads to exceptional ORR and OER bifunctionality in P, N Co-doped graphene frameworks, *Energy Environ. Sci., 2017,* 10, 1186-1195.

[50] S. S. Shinde, C-H. Lee, A. Sami, D-H. Kim, S-U. Lee, J-H. Lee, Scalable 3-D Carbon Nitride Sponge as an Efficient Metal-Free Bifunctional Oxygen Electrocatalyst for Rechargeable Zn–Air Batteries, *ACS Nano, 2017,* 11, 347–357.

[51] H. B. Yang, J. Miao, S-F. Hung, J. Chen, H. B. Tao, X. Wang, L. Zhang, R. Chen, J. Gao, H. M. Chen, L. Dai, B. Liu, Identification of catalytic sites for oxygen reduction and oxygen evolution in N-doped graphene materials: Development of highly efficient metal-free bifunctional electrocatalyst, *Sci. Adv., 2016,* 2, e1501122.

[52] Z. Chen, A. Yu, D. Higgins, H. Li, H. Wang, Z. Chen, Highly Active and Durable Core–Corona Structured Bifunctional Catalyst for Rechargeable Metal–Air Battery Application, *Nano Lett. 2012,* 12, 1946.

[53] H. W. Park, D. U. Lee, P. Zamani, M. H. Seo, L. F. Nazar, Z. Chen, Highly active Co-doped LaMnO3 perovskite oxide and N-doped carbon nanotube hybrid bi-functional catalyst for rechargeable zinc–air batteries, *Nano Energy, 2014,* 10, 192.

[54] G. Li, X. Wang, J. Fu, J. Li, M. G. Park, Y. Zhang, G. Lui, Z. Chen, Pomegranate-Inspired Design of Highly Active and Durable Bifunctional Electrocatalysts for Rechargeable Metal–Air Batteries, *Angew. Chem. Int. Ed. 2016,* 55, 4977.

[55] S. K. Singh, V. M. Dhavale, S. Kurungot, Surface-Tuned Co3O4 Nanoparticles Dispersed on Nitrogen-Doped Graphene as an Efficient Cathode Electrocatalyst for Mechanical Rechargeable Zinc–Air Battery, *ACS Appl. Mater. Interfaces, 2015,* 7, 21138.

[56] Y. Zhang, B. Ouyang, J. Xu, G. Jia, S. Chen, R. S. Rawat, H. J. Fan, Rapid Synthesis of Cobalt Nitride Nanowires: Highly Efficient and Low-Cost Catalysts for Oxygen Evolution, *Angew. Chem. Int. Ed. 2016,* 55, 8670.

[57] Y. Liang, Y. Li, H. Wang, J. Zhou, J. Wang, T. Regier, H. Dai, Co_3O_4 nanocrystals on graphene as a synergistic catalyst for oxygen reduction reaction, *Nat. Mater. 2011,* 10, 780.

[58] A. P. Tiwari, D. Kim, Y. Kim, H. Lee, Bifunctional oxygen electrocatalysis through chemical bonding of transition metal chalcogenides on conductive carbons, *Adv. Energy Mater. 2017,* 7, 1602217.

[59] L. Xu, Q. Jiang, Z. Xiao, X. Li, J. Huo, S. Wang, L. Dai, Plasma-Engraved Co_3O_4 Nanosheets with Oxygen Vacancies and High Surface Area for the Oxygen Evolution Reaction, *Angew. Chem. Int. Ed. 2016,* 55, 5277.

[60] C. F. Chen, G. King, R. M. Dickerson, P. A. Papin, S. Gupta, W. R. Kellogg, G. Wu, Oxygen-deficient $BaTiO_{3-x}$ perovskite as an efficient bifunctional oxygen electrocatalyst, *Nano Energy, 2015,* 13, 423.

[61] J. Bao, X. Zhang, B. Fan, J. Zhang, M. Zhou, W. Yang, X. Hu, H. Wang, B. Pan, Y. Xie, Ultrathin spinel-structured nanosheets rich in oxygen deficiencies for enhanced electrocatalytic water oxidation, *Angew. Chem. Int. Ed. 2015,* 127, 7507.

[62] X. Fan, M. S. Balogun, Y. Huang, Y. Tong, Oxygen-Deficient Three-Dimensional Porous Co3O4 Nanowires as an Electrode Material for Water Oxidation and Energy Storage, *ChemElectroChem, 2017,* 4, 2453.

[63] L. Xu, Q. Jiang, Z. Xiao, X. Li, J. Huo, S. Wang, L. Dai, Plasma-Engraved Co_3O_4 Nanosheets with Oxygen Vacancies and High Surface Area for the Oxygen Evolution Reaction, *Angew. Chem. Int. Ed. 2016,* 55, 5277.

[64] N. Kim, Y. J. Sa, T. S. Yoo, S. R. Choi, R. A. Afzal, T. Choi, Y. Seo, K. Lee, J. Y. Hwang, W. S. Choi, S. H. Joo, J. Park, Oxygen-deficient triple perovskites as highly active and durable bifunctional electrocatalysts for oxygen electrode reactions, *Sci. Adv. 2018,* 4, 9360.

[65] Y. Wang, T. Zhou, K. Jiang, P. Da, Z. Peng, J. Tang, B. Kong, W. Cai, Z. Yang, G. Zheng, Reduced Mesoporous Co_3O_4 Nanowires as Efficient Water Oxidation Electrocatalysts and Supercapacitor Electrodes, *Adv. Energy Mater. 2014,* 4, 1400696.

[66] T. Ling, D. Y. Yan, Y. Jiao, H. Wang, Y. Zheng, X. Zheng, J. Mao, X. W. Du, Z. Hu, M. Jaroniec, S. Z. Qiao, Engineering surface atomic structure of single-crystal cobalt (II) oxide

nanorods for superior electrocatalysis, *Nat. Commum 2016,* 7, 12876.

[67] J. Fu, F. M. Hassan, C. Zhong, J. Lu, H. Liu, A. Yu, Z. Chen, Defect Engineering of Chalcogen-Tailored Oxygen Electrocatalysts for Rechargeable Quasi-Solid-State Zinc–Air Batteries, *Adv. Mater. 2017,* 29, 1702526.

[68] X. Liu, L. Dai, Carbon-based metal-free catalysts, *Nat. Review.Mater. 2016,* 1, 16064.

[69] H. Zhang, R. Lv, Defect engineering of two-dimensional materials for efficient electrocatalysis, *J. Materiomics 2018,* 4, 95.

[70] K. Gong, F. Du, Z. Xia, M. Durstock, L. Dai, Nitrogen-doped carbon nanotube arrays with high electrocatalytic activity for oxygen reduction, *Science 2009,* 323, 760.

[71] Y. Zheng, Y. Jiao, L. Ge, M. Jaroniec, S. Z. Qiao, Two-Step Boron and Nitrogen Doping in Graphene for Enhanced Synergistic Catalysis, *Angew. Chem. Int. Ed. 2013,* 52, 3110.

[72] W. Zhang, W. Lai, R. Cao, Energy-Related Small Molecule Activation Reactions: Oxygen Reduction and Hydrogen and Oxygen Evolution Reactions Catalyzed by Porphyrin- and Corrole-Based Systems, *Chem. Rev. 2016,* 117, 3717.

[73] Z. W. Seh, J. Kibsgaard, C. F. Dickens, I. Chorkendorff, J. K. Nørskov, T. F. Jaramillo, Combining theory and experiment in electrocatalysis: Insights into materials design, *Science 2017,* 355.

[74] F. Zhang, Y. Ge, H. Chu, P. Dong, R. Baines, Y. Pei, M. Ye, J. Shen, Dual-Functional Starfish-like P-Doped Co–Ni–S Nanosheets Supported on Nickel Foams with Enhanced Electrochemical Performance and Excellent Stability for Overall Water Splitting, *ACS Appl. Mater. Interfaces 2018,* 10, 7087.

[75] H. Zhang, T. Wang, A. Sumboja, W. Zang, J. Xie, D. Gao, S. J. Pennycook, Z. Liu, C. Guan, J. Wang, Integrated Hierarchical Carbon Flake Arrays with Hollow P-Doped $CoSe_2$ Nanoclusters as an Advanced Bifunctional Catalyst for Zn-Air Batteries, *Adv. Funct. Mater. 2018,* 1804846.

[76] J. Hao, W. Yang, Z. Peng, C. Zhang, Z. Huang, W. Shi, A Nitrogen Doping Method for CoS_2 Electrocatalysts with Enhanced Water Oxidation Performance, *ACS Catalysis 2017,* 7, 4214.

[77] L. Guo, J. Deng, G. Wang, Y. Hao, K. Bi, X. Wang, Y. Yang, N, P-doped CoS_2 Embedded in TiO_2 Nanoporous Films for Zn-Air Batteries, *Adv. Funct. Mater. 2018,* 1804540.

[78] M. H. Seo, M. G. Park, D. U. Lee, X. Wang, W. Ahn, S. H. Noh, S. M. Choi, Z. P. Cano, B. Han, Z. Chen, Bifunctionally active and durable hierarchically porous transition metal-based

hybrid electrocatalyst for rechargeable metal-air batteries, *Appl. Catal., B 2018*, 239, 677.
[79] D-S. Kim, E. F. A. Zeid, Y-T. Kim, Additive treatment effect of TiO2 as supports for Pt-based electrocatalysts on oxygen reduction reaction activity, *Electrochim. Acta, 2010,* 55, 3628-3633.
[80] H. Kim, M. K. Cho, J. A. Kwon, Y. H. Jeong, K. J. Lee, N. Y. Kim, M. J. Kim, S. J. Yoo, J. H. Jang, H-J. Kim, S. W. Nam, D-H. Lim, E. Cho, K-Y. Lee, J. Y. Kim, Highly efficient and durable TiN nanofiber electrocatalyst supports, *Nanoscale, 2015*, 7, 18429-18434.

Chapter 3

[1] Fu G, Yan X, Chen Y, Xu L, Sun D, Lee JM, Tang Y. Boosting bifunctional oxygen electrocatalysis with 3D graphene aerogel-supported Ni/MnO particles. *Adv. Mater.*, *2018,* 30, 1704609.

[2] Y. Jiang, Y-P. Deng, J. Fu, D. U. Lee, R. Liang, Z. P. Cano, Y. Liu, Z. Bai, S. Hwang, L. Yang, D. Su, W. Chu, Z. Chen, Interpenetrating Triphase Cobalt-Based Nanocomposites as Efficient Bifunctional Oxygen Electrocatalysts for Long-Lasting Rechargeable Zn–Air Batteries, *Adv. Energy Mater. 2018*, 8, 1702900.

[3] J. Fu, F. M. Hassan, J. Li, D. U. Lee, A. R. Ghannoum, G. Lui, Md. A. Hoque, Z. Chen, Flexible Rechargeable Zinc-Air Batteries through Morphological Emulation of Human Hair Array, *Adv. Mater. 2016,* 28, 6421–6428.

[4] https://serc.carleton.edu/research_education/geochemsheets/techniques/XRD.html.

[5] https://en.wikipedia.org/wiki/BET_theory.

[6] https://en.wikipedia.org/wiki/Scanning_transmission_electron_microscopy.

Chapter 4

[1] B. Lim, M. Jiang, P. H. C. Camargo, E. C. Cho, J. Tao, X. Lu, Y. Zhu, Y. Xia, Pd-Pt bimetallic nanodendrites with high activity for oxygen reduction, *Science, 2009,* 324, 1302-1305.

[2] T. Reier, M. Oezaslan, P. Strasser, Electrocatalytic oxygen evolution reaction (OER) on Ru, Ir, and Pt Catalysts: a comparative study of nanoparticles and bulk materials, *ACS Catal. 2012, 2,* 1765-1772.

[3] B. Hua, M. Li, Y-F. Sun, Y-Q. Zhang, N. Yan, J. Chen, T. Thundat, J. Li, J-L. Luo, A coupling for success: Controlled growth of Co/CoO_x nanoshoots on perovskite mesoporous nanofibres as high-performance trifunctional electrocatalysts in alkaline condition, *Nano Energy, 2017,* 32, 247-254.

[4] G. Wu, A. Santandreu, W. Kellogg, S. Gupta, O. Ogoke, H. Zhang, H-L. Wang, L. Dai, Carbon nanocomposite catalysts for oxygen reduction and evolution reactions: From nitrogen doping to transition-metal addition, *Nano Energy, 2016,* 29, 83-110.

[5] Q. Wang, L. Shang, R. Shi, X. Zhang, G.I.N. Waterhousec, L-Z. Wu, C-H. Tung, T. Zhang, 3D carbon nanoframe scaffold-immobilized Ni_3FeN nanoparticle electrocatalysts for rechargeable zinc-air batteries' cathodes, *Nano Energy, 2017,* 40 382-389.

[6] H. Zhu, J. Zhang, R. Yanzhang, M. Du, Q. Wang, G. Gao, J. Wu, G. Wu, M. Zhang, B. Liu, J. Yao, X. Zhang, When cubic cobalt sulfide meets layered molybdenum disulfide: a core-shell system toward synergetic electrocatalytic water splitting, *Adv. Mater. 2015,* 27, 4752-4759.

[7] S. Dou, L. Tao, J. Huo, S. Wang, L. Dai, Etched and doped Co_9S_8/graphene hybrid for oxygen electrocatalysis, *Energy Environ. Sci.,2016,* 9, 1320-1326.

[8] T. Zhou, Y. Du, D. Wang, S. Yin, W. Tu, Z. Chen, A. Borgna, R. Xu, Phosphonate-based metal-organic framework derived Co-P-C hybrid as an efficient electrocatalyst for oxygen evolution reaction, *ACS Catal. 2017,* 7, 6000-6007.

[9] M. Chauhan, K.P. Reddy, C. S. Gopinath, S. Deka, Copper Cobalt Sulfide Nanosheets Realizing a Promising Electrocatalytic Oxygen Evolution Reaction, *ACS Catal. 2017,* 7, 5871-5879.

[10] P. Ganesan, M. Prabu, J. Sanetuntikul, S. Shanmugam, Cobalt sulfide nanoparticles grown on nitrogen and sulfur codoped graphene oxide: an efficient electrocatalyst for oxygen reduction and evolution reactions, *ACS Catal., 2015,* 53625-3637.

[11] J. Wang, W. Cui, Q. Liu, Z. Xing, A. M. Asiri, X. Sun, Recent progress in cobalt-based heterogeneous catalysts for electrochemical water splitting, *Adv. Mater. 2016,* 28, 215-230.

[12] G-F. Chen, T. Y. Ma, Z-Q. Liu, N. Li, Y-Z. Su, K. Davey, S-Z. Qiao, Efficient and stable bifunctional electrocatalysts Ni/Ni_xM_y (M = P, S) for overall water splitting, *Adv. Funct. Mater.,2016,* 26, 3314-3323.

[13] C. Tang, H-S. Wang, H-F. Wang, Q. Zhang, G.-L. Tian, J.-Q. Nie, F. Wei, Spatially confined hybridization of nanometer-sized NiFe hydroxides into nitrogen-doped graphene frameworks leading to superior oxygen evolution reactivity, *Adv. Mater.,2015,* 27, 4516-4522.

[14] J. Fu, F. M. Hassan, C. Zhong, J. Lu, H. Liu, A. Yu, Z. Chen, Defect engineering of chalcogen-tailored oxygen electrocatalysts for rechargeable quasi-solid-state zinc–air batteries, *Adv. Mater., 2017,* 29, 1702526.

[15] L. Zhuang, L. Ge, Y. Yang, M. Li, Y. Jia, X. Yao, Z. Zhu, Ultrathin iron-cobalt oxide nanosheets with abundant oxygen vacancies for the oxygen evolution reaction, *Adv. Mater., 2017,* 29, 1606793.

[16] M. E. G. Lyons, M. P. Brandon, A comparative study of the oxygen evolution reaction on oxidised nickel, cobalt and iron electrodes in base, *J. Electroanal. Chem. 2010,* 641, 119-130.

[17] C. Spöri, H. J. T. Kwan, Ar. Bonakdarpour, D. P. Wilkinson, P. Strasser, The stability challenges of oxygen evolving catalysts: towards a common fundamental understanding and mitigation of catalyst degradation, *Angew. Chem. Int. Ed. 2017,* 56, 5994-6021.

[18] X. Xu, F. Song, X. Hu, A nickel iron diselenide-derived efficient oxygen-evolution catalyst, *Nat. Commun. 2016,* 7, 12324.

[19] C. Yang, O. Fontaine, J-M. Tarascon, A. Grimaud, Chemical recognition of active oxygen species on the surface of oxygen evolution reaction electrocatalysts, *Angew. Chem. Int. Ed. 2017,* 56, 8652-8656.

[20] B. Song, K. Li, Y. Yin, T. Wu, L. Dang, M. Cabán-Acevedo, J. Han, T. Gao, X. Wang, Z. Zhang, J. R. Schmidt, P. Xu, S. Jin, Tuning mixed nickel iron phosphosulfide nanosheet electrocatalysts for enhanced hydrogen and oxygen evolution, *ACS Catal., 2017,* 7, 8549-8557.

[21] Jin, S. Are metal chalcogenides, nitrides, and phosphides oxygen evolution catalysts or bifunctional catalysts? *ACS Energy Lett., 2017,* 2, 1937-1938.

[22] Y. Zhang, B. Ouyang, J. Xu, G. Jia, S. Chen, R.S. Rawat, H. J. Fan, Rapid synthesis of cobalt nitride nanowires: highly efficient and low-cost catalysts for oxygen evolution, *Angew.*

Chem. Int. Ed., 2016, 55, 8670-8674.

[23] W. S. Hummers Jr, R. E. Offeman, Preparation of graphitic oxide, *J. Am. Chem. Soc., 1958*, 80, 1339-1339.

[24] Y. Xu, H. Bai, G. Lu, C. Li, G. Shi, Flexible graphene films via the filtration of water-soluble noncovalent functionalized graphene sheets, *J. Am. Chem. Soc.,2008,* 130, 5856-5857.

[25] L.H. Jin, C.C. Lv, J. Wang, H. Xia, Y.X. Zhao, Z. P. Huang, Co_9S_8 nanotubes as an efficient catalyst for hydrogen evolution reaction in alkaline electrolyte, *Am. J. Analyt Chem., 2016,* 7, 210-218.

[26] J. Wang, L. Li, X. Chen, Y. Lu, W. Yang, Monodisperse cobalt sulfides embedded within nitrogen-doped carbon nanoflakes: an efficient and stable electrocatalyst for the oxygen reduction reaction, *J. Mater. Chem. A, 2016,* 4, 11342-11350.

[27] F. Morales, F. M. F. de Groot, O. L. J. Gijzeman, A. Mens, O. Stephan, B. M. Weckhuysen, Mn promotion effects in Co/TiO_2 Fischer–Tropsch catalysts as investigated by XPS and STEM-EELS, *J. Catal., 2005,* 230, 301-308.

[28] M. Shen, C. Ruan, Y. Chen, C. Jiang, K. Ai, L. Lu, Covalent entrapment of cobalt–iron sulfides in N-doped mesoporous carbon: Extraordinary bifunctional electrocatalysts for oxygen reduction and evolution reactions, *ACS Appl. Mater. Interfaces, 2015,* 7, 1207-1218.

[29] J. Masa, W. Xia, I. Sinev, A. Zhao, Z. Sun, S. Grützke, P. Weide, M. Muhler, Schuhmann, W. Mn_xO_y/NC and Co_xO_y/NC Nanoparticles Embedded in a Nitrogen-Doped Carbon Matrix for High-Performance Bifunctional Oxygen Electrodes, *Angew. Chem. Int. Ed. 2014*, 53, 8508-8512.

[30] B. Seo, Y. J. Sa, J. Woo, K. Kwon, J. Park, T. J. Shin, H. Y. Jeong, S. H. Joo, Size-Dependent Activity Trends Combined with in Situ X-ray Absorption Spectroscopy Reveal Insights into Cobalt Oxide/Carbon Nanotube-Catalyzed Bifunctional Oxygen Electrocatalysis, *ACS Catal. 2016,* 6, 4347.

[31] H. S. Jeon, M.S. Jee, H. Kim, S. J. Ahn, Y. J. Hwang, B. K. Min, Simple Chemical Solution Deposition of Co_3O_4 Thin Film Electrocatalyst for Oxygen Evolution Reaction, *ACS Appl. Mater. Interfaces, 2015,* 7, 24550-24555.

[32] G. Li, X. Wang, J. Fu, J. Li, M. G. Park, Y. Zhang, G. Lui, Z. Chen, Pomegranate-Inspired Design of Highly Active and Durable Bifunctional Electrocatalysts for Rechargeable Metal–Air Batteries, *Angew. Chem. Int. Ed. 2016,* 55, 4977-4982.

[33] A. Aijaz, J. Masa, C. Rçsler, W. Xia, P. Weide, A. J. R. Botz, R.A. Fischer, W.

Schuhmann, M. Muhler, Co@Co_3O_4 Encapsulated in Carbon Nanotube-Grafted Nitrogen-Doped Carbon Polyhedra as an Advanced Bifunctional Oxygen Electrode, *Angew. Chem. Int. Ed. 2016,* 55, 4087-4091.

[34] X. Zhong, Y. Jiang, X. Chen, L. Wang, G. Zhuang, X. Li, J.G. Wang, Integrating cobalt phosphide and cobalt nitrideembedded nitrogen-rich nanocarbons: highperformance bifunctional electrocatalysts for oxygen reduction and evolution, *J. Mater. Chem. A, 2016,* 4, 10575–10584.

[35] Y. Chen, L. Fu, Z. Liu, One-pot synthesis of cobalt-coordinated N-doped carbon catalysts via co-synthesis of ionic liquids and cobalt porphyrins, *Chem. Commun., 2015,* 51, 16637-16640.

[36] R. Wei, M. Fang, G. Dong, C. Lan, L. Shu, H. Zhang, X. Bu, J. C. Ho, High-Index Faceted Porous Co_3O_4 Nanosheets with Oxygen Vacancies for Highly Efficient Water Oxidation, *ACS Appl. Mater. Interfaces, 2018,* 10, 7079.

[37] N. Weidler, S. Paulus, J. Schuch, J. Klett, S. Hoch, P. Stenner, A. Maljusch, J. Bro ̈tz, C. Wittich, B. Kaisera, W. Jaegermann, CoO_x thin film deposited by CVD as efficient water oxidation catalyst: change of oxidation state in XPS and its correlation to electrochemical activity, *Phys. Chem. Chem. Phys., 2016,* 18, 10708.

[38] B. S. Yeo, A. T. Bell, Enhanced activity of gold-supported cobalt oxide for the electrochemical evolution of oxygen, *J. Am. Chem. Soc., 2011,* 1335587.

[39] K.S. Exner, J. Anton, T. Jacob, H. Overa, Chlorine evolution reaction on RuO_2 (110): Ab initio atomistic thermodynamics study-Pourbaix diagrams, *Electrochim. Acta, 2014,* 120, 460-466.

[40] J. Chivot, L. Mendoza, C. Mansour, T. Pauporte ́, M. Cassir, New insight in the behaviour of Co–H_2O system at 25–150℃, based on revised Pourbaix diagrams, Corrosion, *Science, 2008,* 50, 62.

[41] M. Bajdich, M. Garc ́a-Mota, A. Vojvodic, J. K. Nørskov, A.T. Bell, Theoretical investigation of the activity of cobalt oxides for the electrochemical oxidation of water, *J. Am. Chem. Soc., 2013,* 135, 13521.

Chapter 5

[1] X. Han, F. Cheng, T. Zhang, J. Yang, Y. Hu, J. Chen, Hydrogenated uniform Pt clusters supported on porous $CaMnO_3$ as a bifunctional electrocatalyst for enhanced oxygen reduction and evolution, *Adv. Mater. 2014,* 26, 2047–2051.

[2] L. Li, C. Liu, G. He, D. Fan, A. Manthiram, Hierarchical pore-in-pore and wire-in-wire catalysts for rechargeable Zn– and Li–air batteries with ultra-long cycle life and high cell efficiency, *Energy Environ. Sci., 2015,* 8, 3274—3282.

[3] J.C. Li, P.X. Hou, S.Y. Zhao, C. Liu, D.M. Tang, M. Cheng, F. Zhang, H.M. Cheng, A 3D bi-functional porous N-doped carbon microtube sponge electrocatalyst for oxygen reduction and oxygen evolution reactions, *Energy Environ. Sci., 2016,* 9, 3079-3084.

[4] X. Lu, C. Zhao, Highly efficient and robust oxygen evolution catalysts achieved by anchoring nanocrystalline cobalt oxides onto mildly oxidized multiwalled carbon nanotubes. *J. Mater. Chem. A, 2013,* 39, 12053.

[5] S. Maass, F. Finsterwalder, G. Frank, R. Hartmann, C. Merten, Carbon support oxidation in PEM fuel cell cathodes. *J. Power Sources, 2008,* 176,444.

[6] G. Lui, G. Li, X. Wang, G. Jiang, E. Lin, M. Fowler, A. Yu, Z. Chen. Flexible, three-dimensional ordered macroporous TiO_2 electrode with enhanced electrode–electrolyte interaction in high-power Li-ion batteries. *Nano Energy, 2016,* 24, 72.

[7] Y. Liang, Y. Li, H. Wang, J. Zhou, J. Wang, T. Regier, H. Dai, Co_3O_4 nanocrystals on graphene as a synergistic catalyst for oxygen reduction reaction, *Nat. Mater. 2011,* 10, 780.

[8] S. Wang, D. Yu, L. Dai, Polyelectrolyte functionalized carbon nanotubes as efficient metal-free electrocatalysts for oxygen reduction, *J. Am. Chem. Soc. 2011,* 133, 5182.

[9] S. Dou, L. Tao, J. Huo, S. Wang, L. Dai, Etched and doped Co_9S_8/graphene hybrid for oxygen electrocatalysis. *Energy Environ. Sci. 2016,* 9, 1320.

[10] Y. Tang, F. Jing, Z. Xu, F. Zhang, Y. Mai, D. Wu, Highly crumpled hybrids of nitrogen/sulfur dual-doped graphene and Co_9S_8 nanoplates as efficient bifunctional oxygen electrocatalysts. *ACS Appl. Mater. Interfaces. 2017,* 9, 12340.

[11] Y. Zhang, S. Chao, X. Wang, H. Han, Z. Bai, L. Yang, Hierarchical Co_9S_8 hollow microspheres as multifunctional electrocatalysts for oxygen reduction, oxygen evolution and hydrogen evolution reactions. *Electrochim. Acta. 2017,* 246, 380.

[12] M. Al-Mamun, Y. Wang, P. Liu, Y.L. Zhong, H. Yin, X. Su, H. Zhang, H. Yang, D. Wang, Z. Tang, H. Zhao, One-step solid phase synthesis of a highly efficient and robust cobalt pentlandite electrocatalyst for the oxygen evolution reaction. *J. Mater. Chem. A, 2016,* 4, 18314.

[13] Z. Yang, Z. Yao, G. Li, G. Fang, H. Nie, Z. Liu, X. Zhou, X.A. Chen, S. Huang, Sulfur-doped graphene as an efficient metal-free cathode catalyst for oxygen reduction. *ACS nano. 2011*, 6, 205.

[14] Y. Ito, W. Cong, T. Fujita, Z. Tang, M. Chen, High catalytic activity of nitrogen and sulfur co-doped nanoporous graphene in the hydrogen evolution reaction. *Angew. Chem. Int. Ed, 2015* 127, 2159.

[15] Z.H. Sheng, L. Shao, J.J. Chen, W.J. Bao, F.B. Wang, X.H. Xia, Catalyst-free synthesis of nitrogen-doped graphene via thermal annealing graphite oxide with melamine and its excellent electrocatalysis. *ACS nano. 2011*, 5, 4350.

[16] Y. Tang, D. Wu, Y. Mai, H. Pan, J. Cao, C. Yang, F. Zhang, X. Feng, A two-dimensional hybrid with molybdenum disulfide nanocrystals strongly coupled on nitrogen-enriched graphene via mild temperature pyrolysis for high performance lithium storage. *Nanoscale, 2014,* 6, 14679.

[17] H. Jin, J. Li, F. Chen, L. Gao, H. Zhang, D. Liu, Q. Liu, Nitrogen-doped carbon xerogels as novel cathode electrocatalysts for oxygen reduction reaction in direct borohydride fuel cells. *Electrochim. Acta. 2016,* 222, 438.

[18] Z. Liu, L. Ji, X. Dong, Z. Li, L. Fu, Q. Wang, Preparation of Co–N–C supported on silica spheres with high catalytic performance for ethylbenzene oxidation. *RSC Adv. 2015,* 5, 6259.

[19] K. Niu, B. Yang, J. Cui, J. Jin, X. Fu, Q. Zhao, J. Zhang, Graphene-based non-noble-metal Co/N/C catalyst for oxygen reduction reaction in alkaline solution. *J. Power Source, 2013,* 243, 65.

[20] R.Y. Asahi, T.A. Morikawa, T. Ohwaki, K. Aoki, Y. Taga, Visible-light photocatalysis in nitrogen-doped titanium oxides. *Science, 2001,* 293, 269.

[21] S. Ebnesajjad, R. Morgan, editors, Fluoropolymer additives. *William Andrew, 2011,* Dec 5.

[22] D. Xiong, Q. Zhang, S.M. Thalluri, J. Xu, W. Li, X. Fu, L. Liu, One-Step Fabrication of Monolithic Electrodes Comprising Co_9S_8 Particles Supported on Cobalt Foam for Efficient and Durable Oxygen Evolution Reaction. *Chem-Eur. J. 2017,* 23, 8749.

Chapter 6

[1] J. Wang, W. Cui, Q. Liu, Z. Xing, A. M. Asiri, X. Sun, Recent progress in cobalt-based heterogeneous catalysts for electrochemical water splitting, *Adv. Mater. 2016,* 28, 215.

[2] Y. Li, M. Gong, Y. Liang, J. Feng, J. E. Kim, H. Wang, G. Hong, B. Zhang, H. Dai, Advanced zinc-air batteries based on high-performance hybrid electrocatalysts, *Nat. Commun. 2013,* 4, 1805.

[3] S. Dresp, F. Luo, R. Schmack, S. Ku ̈hl, M. Gliech, P. Strasser, An efficient bifunctional two-component catalyst for oxygen reduction and oxygen evolution in reversible fuel cells, electrolyzers and rechargeable air electrodes, *Energy Environ. Sci. 2016,* 9, 2020.

[4] Z. Zhao, Z. Xia, Design principles for dual-element-doped carbon nanomaterials as efficient bifunctional catalysts for oxygen reduction and evolution reactions, *ACS Catal. 2016,* 6, 1553.

[5] Y. P. Zhu, C. Guo, Y. Zheng, S.Z. Qiao, Surface and interface engineering of noble-metal-free electrocatalysts for efficient energy conversion processes, *Acc. Chem. Res. 2017,* 50, 915.

[6] G.L. Chai, K. Qiu, M. Qiao, M.M. Titirici, C. Shang, Z. Guo, Active sites engineering leads to exceptional ORR and OER bifunctionality in P, N Co-doped graphene frameworks, *Energy Environ. Sci. 2017,* 10, 1186.

[7] G. A. Ferrero, K. Preuss, A. Marinovic, A. B. Jorge, N. Mansor, D. J. L. Brett, A.B. Fuertes, M. Sevilla, M.M. Titirici, Fe–N-doped carbon capsules with outstanding electrochemical performance and stability for the oxygen reduction reaction in both acid and alkaline conditions, *ACS Nano, 2016,* 10, 5922.

[8] B. Y. Xia, Y. Yan, N. Li, H. B. Wu, X.W. Lou, X. Wang, A metal–organic framework-derived bifunctional oxygen electrocatalyst, *Nat. Energy 2016,* 1, 15006.

[9] Z.-F. Huang, J. Wang, Y. Peng, C.-Y. Jung, A. Fisher, Xin Wang, Design of efficient bifunctional oxygen reduction/evolution electrocatalyst: recent advances and perspectives, *Adv. Energy Mater. 2017,* 7, 1700544.

[2] F.S. Saleh, E. B. Easton, Diagnosing degradation within PEM fuel cell catalyst layers using electrochemical impedance spectroscopy, *J. Electrochem. Soc. 2012,* 159, B546.

[3] C. Spoeri, J. T. H. Kwan, A. Bonakdarpour, D. P. Wilkinson, P. Strasser, The stability challenges of oxygen evolving catalysts: towards a common fundamental understanding and mitigation of catalyst degradation, *Angew. Chem. Int. Ed. 2017,* 56, 5994.

[4] N. G. Akalework, C. J. Pan, W. N. Su, J. Rick, M. C. Tsai, J. F. Lee, J. M. Lin, L. D. Tsai, B. J. Hwang, Ultrathin TiO_2-coated MWCNTs with excellent conductivity and SMSI nature as Pt catalyst support for oxygen reduction reaction in PEMFCs, *J. Mater. Chem. 2012,* 22, 20977.

[5] G. Zhao, R. Mo, B. Wang, L. Zhang, K. Sun, Enhanced Cyclability of Li–O_2 Batteries Based on TiO_2 Supported Cathodes with No Carbon or Binder, *Chem. Mater. 2014,* 26, 2551.

[6] A. Lewera, L. Timperman, A. Roguska, N. Alonso-Vante, Metal–Support Interactions between Nanosized Pt and Metal Oxides (WO_3 and TiO_2) Studied Using X-ray Photoelectron Spectroscopy, *J. Phys. Chem. C, 2011,* 115, 20153.

[7] A. Vesel, M. Mozetic, J. Kovac, A. Zalar, XPS study of the deposited Ti layer in a magnetron-type sputter ion pump, *Appl. Surf. Sci. 2006,* 253, 2941.

[8] B. Avasarala, P. Haldar, Electrochemical oxidation behavior of titanium nitride based electrocatalysts under PEM fuel cell conditions, *Electrochim. Acta, 2010,* 55, 9024.

[9] B. Avasarala, P. Haldar, On the stability of TiN-based electrocatalysts for fuel cell applications, *Int. J. Hydrog. Energy, 2011,* 36, 3965.

[10] A. Grimaud, K. J. May, C. E. Carlton, Y-L. Lee, M. Risch, W. T. Hong, J. Zhou, Y. Shao-Horn, Double perovskites as a family of highly active catalysts for oxygen evolution in alkaline solution, *Nat. Commun. 2013,* 4, 2439.

[11] B. J. Kim, D. F. Abbott, X. Cheng, E. Fabbri, M. Nachtegaal, F. Bozza, I. E. Castelli, D. Lebedev, R. Schäublin, C. Copéret, T. Graule, N. Marzari, T. J. Schmidt, Unraveling thermodynamics, stability, and oxygen evolution activity of strontium ruthenium perovskite oxide, *ACS Catal. 2017,* 7, 3245.

[12] Y. Zhu, W. Zhou, Y. Zhong, Y. Bu, X. Chen, Q. Zhong, M. Liu, Z. Shao, A perovskite nanorod as bifunctional electrocatalyst for overall water splitting, *Adv. Energy Mater. 2017,* 7, 1602122.

[13] H. Liu, F. Zeng, Y. Lin, G. Wang, F. Pan, Correlation of oxygen vacancy variations to band gap changes in epitaxial ZnO thin films, *Appl. Phys. Lett. 2013,* 102, 181908.

[14] X. L. Wang, C. Y. Luan, Q. Shao, A. Pruna, C. W. Leung, R. Lortz, J. A. Zapien, A. Ruotolo, Effect of the magnetic order on the room-temperature band-gap of Mn-doped ZnO thin films, *Appl. Phys. Lett. 2013,* 102, 102112.

[15] J. A. Farmer, C. T. Campbell, Ceria maintains smaller metal catalyst particles by strong metal-support bonding, *Science, 2010,* 329, 933.

[16] P. Chen, A. Khetan, F. Yang, V. Migunov, P. Weide, S. P. Stürmer, P. Guo, K. Kähler, W. Xia, J. Mayer, H. Pitsch, U. Simon, M. Muhler, Experimental and Theoretical Understanding of Nitrogen-Doping-Induced Strong Metal–Support Interactions in Pd/TiO_2 Catalysts for Nitrobenzene Hydrogenation, *ACS Catal. 2017*, 7, 1197.

[17] J. C. Matsubu, S. Zhang, L. DeRita, N. S. Marinkovic, J. G. Chen, G. W. Graham, X. Pan, P. Christopher, Adsorbate-mediated strong metal–support interactions in oxide-supported Rh catalysts, *Nat. Chem. 2017*, 9, 120.

[18] M-C. Tsai, T-T. Nguyen, N. G. Akalework, C-J. Pan, J. Rick, Y-F. Liao, W-N. Su, B-J. Hwang, Interplay between Molybdenum Dopant and Oxygen Vacancies in a TiO_2 Support Enhances the Oxygen Reduction Reaction, *ACS Catal. 2016*, 6, 6551.

[19] I. N. Remediakis, N. Lopez, J. K. Nørskov, CO oxidation on rutile-supported Au nanoparticles, *Angew. Chem. Int. Ed. 2005*, 44, 1824.

[20] H-S. Oh, H. N. Nong, T. Reier, A. Bergmann, M. Gliech, J. F. de Araújo, E. Willinger, R. Schlögl, D. Teschner, P. Strasser, Electrochemical Catalyst–Support Effects and Their Stabilizing Role for IrOx Nanoparticle Catalysts during the Oxygen Evolution Reaction, *J. Am. Chem. Soc. 2016*, 138, 12552.

[21] D. Yan, Y. Li, J. Huo, R. Chen, L. Dai, S. Wang, Defect chemistry of nonprecious-metal electrocatalysts for oxygen reactions, *Adv. Mater. 2017*, 29, 1606459.

[22] Y. Guo, Y. Tong, P. Chen, K. Xu, J. Zhao, Y. Lin, W. Chu, Z. Peng, C. Wu, Y. Xie, Engineering the electronic state of a perovskite electrocatalyst for synergistically enhanced oxygen evolution reaction, *Adv. Mater. 2015*, 27, 5989.

[23] G. Lui, G. Li, X. Wang, G. Jiang, E. Lin, M. Fowler, A. Yu, Z.W. Chen, Flexible, three-dimensional ordered macroporous TiO_2 electrode with enhanced electrode–electrolyte interaction in high-power Li-ion batteries, *Nano Energy. 2016*, 24, 72.

[24] http://xpssimplified.com/elements/carbon.php

[25] J. Fu, F. M. Hassan, C. Zhong, J. Lu, H. Liu, A. Yu, Z. Chen. Defect Engineering of Chalcogen-Tailored Oxygen Electrocatalysts for Rechargeable Quasi-Solid-State Zinc–Air Batteries, *Adv. Mater. 2017*, 29, 1702526.

[26] B.Y. Xia, Y. Yan, N. Li, A metal–organic framework-derived bifunctional oxygen electrocatalyst, *Nat. Energy. 2016*, 1, 15006.

[27] Y. Hu, J. Jensen, W. Zhang, L. N. Cleemann, W. Xing, N. J. Bjerrum, Q. Li. Direct

Synthesis of Fe_3C-Functionalized Graphene by High Temperature Autoclave Pyrolysis for Oxygen Reduction, *Angew. Chem. Int. Edit. 2014,* 53, 3675.

[28] Y. Liang, Y. Li, H. Wang, J. Zhou, J. Wang, T. Regier, H. Dai, Co_3O_4 nanocrystals on graphene as a synergistic catalyst for oxygen reduction reaction, *Nat. Mater. 2011,* 10, 780;

[29] S. Wang, D. Yu, L. Dai, Polyelectrolyte functionalized carbon nanotubes as efficient metal-free electrocatalysts for oxygen reduction, *J. Am. Chem. Soc. 2011,* 133, 5182.

[30] J. P. Perdew, K. Burke, M. Ernzerhof, Generalized gradient approximation made simple, *Phys. Rev. Lett. 1996,* 77, 3865.

[31] G. Kresse, J. Hafner, Ab initio molecular dynamics for liquid metals, *Phys. Rev. B. 1993,* 47, 558.

[32] G. Kresse, J. Furthmüller, Efficient iterative schemes for ab initio total-energy calculations using a plane-wave basis set, *J. Phys. Rev. B. 1996,* 54, 11169.

[33] Z. Helali, A. Markovits, C. Minot, M. Abderrabba, First-row transition metal atoms adsorption on rutile TiO_2(110) surface, *Struct Chem. 2012,* 23,1309.

[34] R. Zhang, B. Wang, H. Liu, L. Ling, Effect of Surface Hydroxyls on CO_2 Hydrogenation Over Cu/γ-Al_2O_3 Catalyst: A Theoretical Study, *J. Phys. Chem. C 2011,* 115, 19811.

[35] Y. Pan, C. Liu, Q. Ge, Effect of surface hydroxyls on selective CO_2 hydrogenation over Ni4/γ-Al_2O_3: A density functional theory study, *J. Catal. 2010,* 272, 227.

[36] I. N. Remediakis, N. Lopez, J. K. Nørskov, CO oxidation on rutile-supported Au nanoparticles, *Angew. Chem. Int. Ed. 2005,* 44, 1824.

[37] J. C. Groen, L.A.A. Peffer, J. Pérez-Ramírez, Pore size determination in modified micro-and mesoporous materials. Pitfalls and limitations in gas adsorption data analysis, *Microporous Mesoporous Mater. 2003,* 60, 1.

[38] R. L. Kurtz, V. E. Henrich, Comparison of Ti 2p Core-Level Peaks from TiO_2, Ti_2O_3, and Ti Metal, by XPS, *Surf. Sci. Spectra. 1998,* 5, 179.

[39] B. Avasarala, P. Haldar, On the stability of TiN-based electrocatalysts for fuel cell applications, *Int. J. Hydrog. Energy. 2011,* 36, 3965.

[40] Q. Zuo, G. Cheng, W. Luo, A reduced graphene oxide/covalent cobalt porphyrin framework for efficient oxygen reduction reaction, *Dalton Trans. 2017,* 46, 9344.

[41] H. Jin, J. Li, F. Chen, L. Gao, H. Zhang, D. Liu, Q. Liu, Nitrogen-doped carbon xerogels as novel cathode electrocatalysts for oxygen reduction reaction in direct borohydride fuel cells,

Electrochim. Acta, 2016, 222, 438.

[42] P.O. Larsson, A. Andersson, L. R. Wallenberg, B. Svensson, Combustion of CO and toluene; characterisation of copper oxide supported on titania and activity comparisons with supported cobalt, iron, and manganese oxide, *J. Catal. 1996,* 163, 279.

[43] B.J. Tan, K.J. Klabunde, P.M.A. Sherwood, XPS studies of solvated metal atom dispersed (SMAD) catalysts. Evidence for layered cobalt-manganese particles on alumina and silica, *J. Am. Chem. Soc. 1991,* 113, 855.

[44] B. Bharti, S. Kumar, H-N. Lee, R. Kumar, Formation of oxygen vacancies and Ti^{3+} state in TiO_2 thin film and enhanced optical properties by air plasma treatment, *Sci. Rep. 2016,* 6, 32355.

[45] M. D. Banus, T. B. Reed, A. J. Strauss, Electrical and magnetic properties of TiO and VO, *Phys. Rev. B, 1972,* 5, 2775.

[46] H. Liu, F. Zeng, Y. Lin, G. Wang, F. Pan, Correlation of oxygen vacancy variations to band gap changes in epitaxial ZnO thin films, *Appl. Phys. Lett. 2013,* 102, 181908.

[47] X. L. Wang, C. Y. Luan, Q. Shao, A. Pruna, C. W. Leung, R. Lortz, J. A. Zapien, A. Ruotolo, Effect of the magnetic order on the room-temperature band-gap of Mn-doped ZnO thin films, *Appl. Phys. Lett. 2013,* 102, 102112.

[48] U. Kaiser, D. A. Muller, J. Grazul, A. Chuvulin, M. Kawasaki, Direct observation of defect-mediated cluster nucleation, *Nature Mater. 2002,* 1, 102.

[49] D. A. Muller, N. Nakagawa, A. Ohtomo, J. L. Grazul, H. Y. Hwang, Atomic-scale imaging of nanoengineered oxygen vacancy profiles in $SrTiO_3$, *Nature, 2004,* 430, 657.

[50] T. Zheng, C. Wu, M. Chen, Y. Zhang, P. T. Cummings, A DFT study of water adsorption on rutile TiO_2 (110) surface: The effects of surface steps, *J. Chem. Phys. 2016,* 145, 044702.

[51] Poppa, H. Catal. Nucleation, growth, and TEM analysis of metal particles and clusters deposited in UHV, *Rev. Sci. Eng. 1993,* 35, 359.

[52] M. Che, Z. X. Cheng, C. Louis, Nucleation and particle growth processes involved in the preparation of Silica-Supported nickel materials by a Two-Step procedure, *J. Am. Chem. Soc. 1995,* 117, 2008.

[53] C. C. L. McCrory, S. Jung, C. Peters, T. F. Jaramillo, Benchmarking heterogeneous electrocatalysts for the oxygen evolution reaction, *J. Am. Chem. Soc. 2013,* 135, 16977.

[54] N. Ghenzi, M. J. Rozenberg, R. Llopis, P. Levy, L. E. Hueso, P. Stoliar, Tuning the resistive switching properties of TiO_{2-x} films, *Appl. Phys. Lett. 2015,* 106, 123509.

[55] Y. Du, A. Kumar, H. Pan, K. Zeng, S. Wang, P. Yang, A.T. S. Wee, The resistive switching in TiO_2 films studied by conductive atomic force microscopy and Kelvin probe force microscopy, *AIP Adv. 2013*, 3, 082107.